Dissertation

submitted to the

Combined Faculties for the Natural Sciences and Mathematics

of the Ruperto-Carola University of Heidelberg, Germany

for the degree of

Doctor of Natural Sciences

Presented by

Sayyora Artikova

born in Mangit, Uzbekistan

Oral examination: 2^{nd} May, 2012

Low-Energy Ions in the Heavy Ion Cooler Storage Ring TSR

Referees: Prof.Dr. Joachim Ullrich
Prof.Dr. Andreas Wolf

Ionen niedriger Energie im Schwerionenkühlerspeichering TSR

Um Ionenstrahlen im Energiebereich zwischen einigen keV und einigen MeV zu erzeugen, ist eine Abbremsung dieser Ionenstrahlen erforderlich. Die Verlangsamung von Ionenstrahlen in einem Speichering beruht auf einem Vorschlag von Poth (1990). Bei diesem Vorgang ist der Einfluss der Wechselwirkung der Ionen mir dem Restgas, das "Intrabeam Scattering" (IBS) sowie der inkohärente "Tuneshift" von entscheidender Bedeutung. Das Ziel dieser Doktorarbeit ist die Abbremsung von Ionenstrahlen im Schwerionenkühlerspeichering TSR. Ebenso soll die Dynamik des Abbremsvorgangs untersucht werden. Die vorliegende Doktorarbeit konzentriert sich auf die Untersuchung des Abbremsvorgangs von $^{12}C^{6+}$ Ionen, dabei sollen alle Prozesse erforscht werden, die einen Einfluss auf die Strahlentwicklung haben. Um den Ablauf zu untersuchen wurden $^{12}C^{6+}$ Ionen von 73.3 MeV auf 9.77 MeV mit einer Effizienz von etwa 90 % abgebremst. Damit Experimente bei der Endenergie durchgeführt werden können, wurden zwei Kühlschritte bei der Anfangs- und Endenergie durchgeführt. Die Elektronenvorkühlung erzeugt einen sehr dichten Ionenstrahl, so dass IBS Effekte in Betracht gezogen werden müssen, um die Entwicklung des Ionenstrahls zu verstehen. Damit die experimentelle Daten beschrieben werden können, wurde ein Näherungsmodell für das IBS entwickelt. Da beim Abbremsvorgang die Umlauffrequenz und damit die Intensität des Ionenstrahls verkleinert wird, kann der Ionenstrom mit dem vorhandenen Strahlstromtransformator nur schwer gemessen werden. Deshalb wurden neue Methoden verwendet und entwickelt mit deren Hilfe sehr kleine Ionenströme im TSR gemessenen werden können. Ebenso wurden inkohärente "Tuneshift" Effekte untersucht, die den maximale Ionenstrom begrenzen. Die Verfügbarkeit von niederenergetischen Ionenstrahlen erweitert den Energiebereich in dem mehrfachgeladene Ionen für "MOT-Remi" Experimente verwendet werden können, um Ion-Atom Stöße präzise zu untersuchen.

Low-Energy Ions in the Heavy Ion Cooler Storage Ring TSR

Deceleration is required to produce multicharged ion beams in the energy range from few keV to few MeV. It should be noted that the idea of decelerating ions in storage rings to lower energies dates back to H. Poth (1990). During deceleration of the charged particle beam, the influence of residual gas interaction, intrabeam scattering (IBS) as well as the incoherent space charge tune shift increase. These phenomena are mostly dominant in storage rings and become important at low velocities.
The purpose of this PhD thesis is the generation of low-velocity ion beams by deceleration at the heavy ion cooler storage ring TSR and the study of the accompanying processes. Deceleration experiments concentrated on $^{12}C^{6+}$ ions to identify the mechanisms which have an influence on the behavior and evolution of the beam. To explore the deceleration cycle, the $^{12}C^{6+}$ ions are decelerated from 73.3 MeV to 9.77 MeV with an efficiency of 90%. To achieve this low energy two cooling steps at the initial and final energies of the beam are applied. Electron pre-cooling results in a dense ion beam where IBS has to be taken into account to describe the development of beam size during deceleration. An approximated model of IBS is proposed to interpret the experimental data. A decrease of the ion beam revolution frequency during the deceleration cycle reduces the beam current, which makes it difficult to measure with a common current transformer. Hence, new techniques are applied at low ion currents to determine the stored number of particles. Also incoherent tune shift effects, limiting the maximum number of stored particles are investigated. The availability of low-energy ion beams will expand the range of multicharged beam energies for precision studies of ion-atom collision in-ring MOT-Remi experiments.

Contents

1 Introduction

As natural sources of fast particles are limited in energy and intensity, it was not surprising that in 1928, Cockcroft and Walton, encouraged by Rutherford, were set to the task of building a particle accelerator at the Cavendish Laboratory, UK. By 1932, the apparatus was finished and used to split lithium nuclei with 400 keV protons. This was the first fully man-controlled splitting of the atom. From the measurement of the binding energy, it provided the experimental verification of Einstein's mass-energy relationship, known since 1905. Sir John D. Cockcroft and Ernest T. Walton received jointly, the Nobel Prize award for their pioneer work on the "transmutation of atomic nuclei by artificially accelerated atomic particles" in 1951[1]. This was the start of the era of particle accelerators as one of the most important tools for the experimental physics in general and nuclear physics research, in particular, for many decades.

Since then there has been tremendous progress in the construction and diversity of such machines. However, this academic image is fast changed as the applications for accelerators become more and more diversified. They are already well established in radiation therapy, ion implantation and isotope production. Synchrotron light and the spallation neutron sources form large and rapidly growing branches of the accelerator family. In time accelerators may be used for the bulk sterilization of food and waste products, for the cleaning of exhaust gases from factories, or as the drivers in inertial fusion devices. Research and technology developments toward circular machines as a part of the accelerator complexes made small storage rings feasible due to the successful demonstration of phase cooling[2] as well as the progress in the vacuum technology allowing to reach the 10^{-12} mbar regime.

Indeed, accelerators and storage rings do provide an extremely rich field for the study of fundamental physics principles. The current storage-ring facilities are mostly involved in atomic, molecular and nuclear physics research. One of the common driving ideas for all of these projects is to enhance the phase-space density of the stored ions by cooling that is, the momentum exchange with a collinear electron beam of the same mean velocity. Thus, finally reaching a relative momentum spread $\Delta p/p$ of the ions smaller than 10^{-4} very small beam emittances became possible. Therewith exciting perspectives are opened for precision experiments in fundamental, atomic and nuclear physics. Another common feature of all the rings is the storage of high numbers of particles up to the space-charge limit. Combined with low emittance and large revolution frequencies, high luminosities are reached enabling a whole suite of new experiments. The ion cooler storage rings that previously operated and are presently in operation are listed in table 1.1. Most recently, accelerators based on X-ray lasers, like the Linac Coherent Light Source (LCLS) at the SLAC National Laboratory in Standford, came into operation with many exciting prospects for science and applications. New projects such as the Small Laser-equipped Storage Ring (S-LSR) in Japan, the Heavy Ion Research Facility Lanzhou and Cooler Storage Ring (HIRFL-CSR) in China for the physics with radioactive and other heavy-ion beams are constructed.

Table 1.1: Ion cooler rings.

Projects	$B\rho$ (Tm)	**stochastic cooling**	**electron cooling**	**laser cooling**	**research purpose**
CRYRING (Stockholm)	1.4		0.2-13 kV		atomic and molecular physics
TSR(Heidelberg)	1.5		0.5-16 kV	13.3 MeV ($^7Li^+$)	accelerator, atomic
				7.3 MeV ($^9Be^+$)	and molecular physics
ASTRID(Aarhus)	1.9		0.001-2 kV	100 keV ($^7Li^+$)	atomic and molecular physics
"Cooler"(Bloomington, IN)	3.6		20-300 kV		nuclear and accelerator physics
TARN II(Tokyo)	6.1	7 MeV/c	15-110 kV		accelerator, atomic and molecular physics
CELSIUS(Uppsala)	7.0		5-300 kV		nuclear physics
LEAR, LEIR(CERN)	7.0	2-1270 MeV/c	1-30 kV		antiproton physics, prepare beams of Pb^{54+} for LHC
ESR(Darmstadt)	10.0	$0.7 \leq \beta \leq 0.75$	2-240 kV		atomic, nuclear and accelerator physics
COSY(Jülich)	11.7	1-2.5 GeV	20-100 kV		nuclear physics
SIS(Darmstadt)	18.0		5-35 kV		nuclear physics
S-LSR (Kyoto)	0.95		4 kV	40 keV ($^{24}Mg^+$)	accelerator physics
CSRm, CSRe (Lanzhou)	10.6, 6.4		25 kV, 150 kV		atomic and nuclear physics

The Heidelberg Test Storage Ring (TSR)[6] started operating in May 1988. It is a low-energy cooler storage ring for heavy ions with energies up to 30 MeV/u at a charge-to-mass ratio q/A=0.5. With the combination of a 12 MV tandem and a post-accelerator, the TSR is a very versatile experimental facility for pursuing accelerator, atomic, molecular and nuclear physics. The storage ring consists of four straight sections serving primarily for: (i) injection, (ii) electron cooling, (iii) experiments and (iv) for bunching, acceleration or deceleration with an RF resonator. The desire to accumulate, store, accelerate or decelerate highly charged heavy ions and the need for efficient electron cooling controlled the ring design.

Atomic physics experiments on the basis of the TSR include such studies as interactions between the stored ion beam and internal fixed gas-jet targets, studies of electron-ion interactions of the circulating beam in the electron cooler, as well as investigations to store beams with multiple charge states.

Multicharged ion beams with the energies, ranging from a few MeV down to even a few keV, play an important role in different aspects of research in atomic and molecular physics. Most of the accelerators cannot produce highly charged ion beams at low energies with sufficient intensity, due to the inefficiency of the gas or foil stripping at lower energies. There exists a broad variety of experiments involving high charge state ions that still await exploration in this energy range. For example, in atomic collisions, inner-shell excitation, and vacancy producing processes have thresholds in the lower energy range. Experimental investigations in this energy range are of fundamental interest, since they allow to explore the behavior of the collision systems by taking into account the transition from the low-energy "molecular" regime to the intermediate energy "atomic" regime, and provide important benchmark data in this theoretically challenging energy range. Therefore, to provide (low- and medium-energy, multi-, highly charged ion) such beams, deceleration is necessary.

Deceleration in storage ring to lower energies was proposed a long time ago[3], but so far experiments at the TSR were mainly performed with ions at injected energies. Since the RF system of the ring has a widely tunable range, deceleration is also possible. Recently, providing intense beams of multicharged ions at medium and low energies, was motivated by the goal to perform atomic and molecular collision experiments. The availability of lower-energy ion beams will expand the range of multicharged ion beam energies to in-ring experiments at the TSR. New atomic physics experiments can be conducted, for studying the collisional properties of the multicharged ions as well as various aspects of their atomic structure with a wide variety of experimental techniques such as the magneto-optical trap reaction microscope (MOT-Remi)[4]. The accurate measurement of the ion-atom collisions can be achieved by combining three techniques: the TSR for the storing and cooling of the projectile ions, a magneto-optical trap (MOT) for cooling the target atoms down to temperatures below 1 mK, and a reaction microscope for measuring the momenta after the collisions. Varying the energy of ions is required to study the ionization processes in kinematically complete experiments using a reaction microscope to answer open questions about the energy dependence of various processes.

The production of the low-energy ions is accomplished at the TSR by deceleration. Deceleration of the charged particle beam is accompanied with intrabeam scattering and an increase of the space-charge tune-shift, influences of the scattering on the residual gas and therefore, considerable challenges arise. Thus, the purpose of this thesis is to pro-

duce and characterize low-energy ion beams in the TSR and to study the accompanying processes. Tracing the beam dynamics during deceleration is especially needed to identify the mechanisms that influence the beam development during these phases.

The thesis is organized as follows: a brief history, achievements and future perspectives of the field are introduced in the **chapter 1**. In **chapter 2** a basic description of the heavy ion storage ring TSR facility is presented. Machine parameters, operational characteristics of the TSR, experimental techniques which were employed previously and developed in the present study are discussed in the **chapter 3**. Beam losses due to the residual gas interactions, lifetime measurements and space-charge effects, incoherent tune shift which limits the beam intensity, are studied in **chapter 4**. A simple analytical model of IBS is presented in **chapter 5** with obtained experimental verifications. Results of the deceleration are discussed in detail in **chapter 6**. The analysis of the energy dependency of relevant phenomena in the acceleration of the beam is also presented in this chapter. Summary of the results obtained and an outlook are presented in **chapter 7**. Calibration measurements of experiments are given in the **Appendices**.

2 The heavy ion cooler storage ring TSR

A storage ring is a device in which a beam of particles is confined in a vacuum system by magnetic fields for time periods that are long compared with the scale set by the laboratory length divided by the particle velocity[5]. Storage of a particular particle depends upon its mass, energy and charge. There are few main factors that make ion storage rings interesting for atomic and molecular physics. The storage time is sufficiently long to allow the application of beam cooling, and the circulation of the beam ensures that ions which pass the thin gas-target essentially without interacting return to the target after a short time ($\propto 1 - 10\ \mu s$), thus guaranteeing highly effective currents. Moreover, the beam can be bunched into short buckets such that time-of-flight detection methods become applicable which are at the heart of the "reaction microscope" many particle imaging technology.

The TSR[6] has a circumference of 55.4 m and the maximum magnetic rigidity of the dipoles is $B\rho$=1.5 Tm. Fig.2.1 shows a schematic layout of the TSR lattice. QF and QD

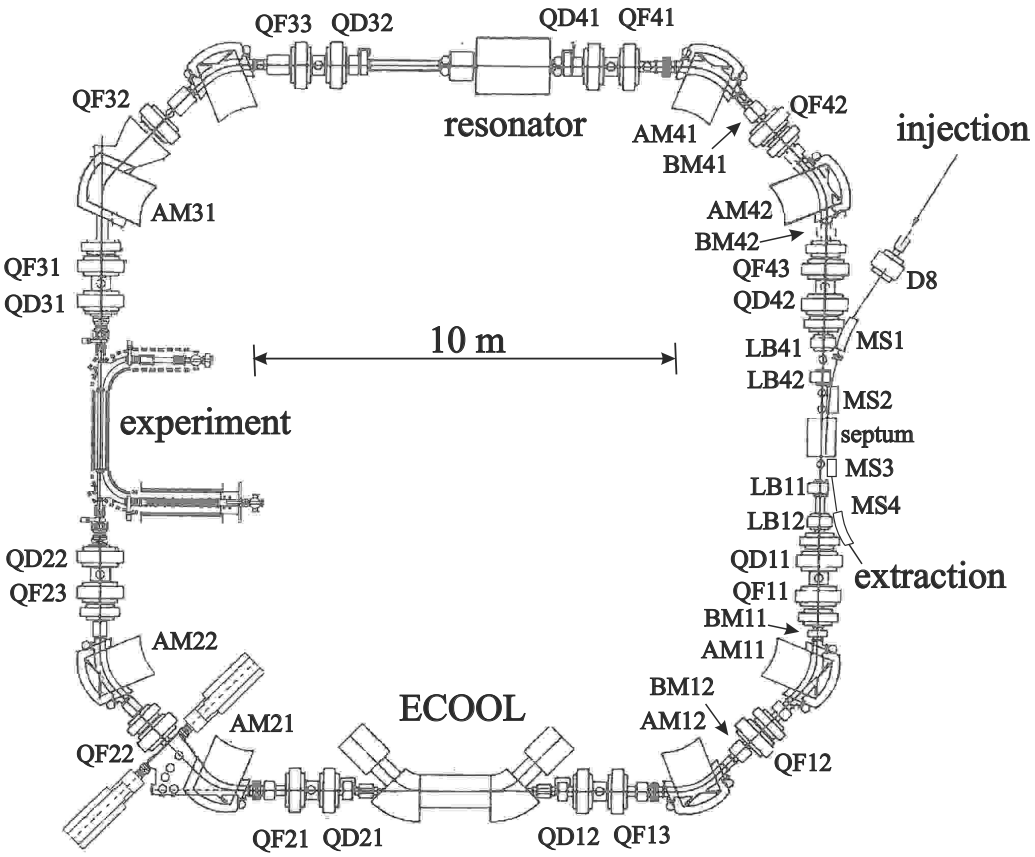

Figure 2.1: The TSR lattice

are twenty quadrupoles which are grouped into five families to focus the beam. They are all of the same type and their parameters are also quite identical. The bending fields of the ring are provided by 45° curved eight dipoles AM assembled from 1 mm steel laminations. Alignment and magnetic field errors distort the closed orbit, therefore each dipole comprises backing windings for horizontal correction. In addition, magnets for vertical corrections are placed in between two quadrupoles in each section. Sextupoles in the ring are used for chromaticity correction and slow extraction using 3^{rd} order resonances. An injection pursued by two magnetic septa and an electrostatic septum. Bumper magnets BM, in the injection section of the ring make a time-dependent deformation of the main orbit possible, resulting in the possibility to store many orbits side by side. This so-called multiturn injection technique leads to a filling of the transverse phase space of the ring. With this method, the intensity can be increased by a factor 40 as compared to a single-turn injection. Another independent method to increase the current in the storage ring is called RF stacking[7]. In this case, via the RF resonator the energy of the ions can be slightly changed and up to the eighteen inconsiderably different energies have been accumulated in the ring, thus filling the longitudinal phase space as well. For this method, it is essential to produce dispersion in the injection straight section, that the ring indicates a momentum acceptance $\Delta p/p$ of 3%. Due to its large apertures, the ring has a horizontal acceptance of A_x=100 mm mrad and a vertical acceptance of A_y=40 mm mrad. The electron cooler is located in the straight section after the injection part, with its large support structure carrying its solenoids and toroids. The electrons start at a thermionic cathode and are recovered finally in the collector on the other side with an efficiency of more than 99.94%. The electron beam diameter (3 cm) can be adjusted due to the adiabatic expansion of the electron beam reducing the transverse temperature. The maximum electron current in the cooler is 1 A. The electron beam overlaps with the ion beam for 1.5 m and is guided over its complete length by a longitudinal magnetic field of 0.05-0.1 T. This field prevents a blowup of the intense electron beam and, furthermore, decouples the longitudinal and transverse degrees of freedom of the electrons. Electron beam temperatures of 0.1 meV longitudinally and 5 meV transversely are routinely reached. The experimental area starts with a large dipole chamber in the first dipole magnet AM21 behind the electron cooler. Since the main beam and charge-changed ions are deflected differently, charge-changing reactions in the electron cooler can be observed by placing high-efficiency detectors at appropriate location around the magnet. Another straight section of the ring located in between the dipoles AM22 and AM31 presently contains special equipment for experiments, for example, an electron target, the reaction microscope with internal gas jet or a MOT target, which can be moved in and out. The fourth straight section houses the RF resonator used for bunching, acceleration or deceleration of the beam. If the storage ring is operated at a stable working point, the loss of ions is primarily determined by interactions with the residual gas and the electrons in the electron cooler. Since the lifetime of ion beams in the ring decisively depends on the residual gas pressure, the vacuum system was designed to achieve a quite low pressure of about 10^{-11} mbar.

2.1 The RF resonator

RF resonator is a device designed to generate strong and time-varying electric fields. It has been mainly developed in the radio-wave region of the electromagnetic spectrum, because of both, technical (availability of power sources) and physics (acceleration of particles) motivation. Variable frequency RF accelerating systems use mostly a ferrite loaded resonator. In such devices, the resonator length may be reduced by placing ferrite toroids in the volume around the beam tube or between the inner and outer conductors which allow to resonator to reach lower frequencies at a reasonable size. The eigenfrequency is lowered because the large relative permeability reduces the wave speed inside the resonator. Also, by biasing the ferrite with an external bucking field the permeability can be varied so that the eigenfrequency follows the changing particle revolution frequency as the beam accelerates or decelerates. However, the inside construction of these resonators is complicated by the necessary ferrite ring supports and the bias windings which reduce the ferrite volume. Furthermore, the RF voltage induced in the bias windings requires supplementary RF filters, which may lead to some parasitic resonances. To avoid these complications a new type quadrupole ferrite-loaded resonator was developed at MPIK[9, 10]. In contrast to the common ferrite loaded RF resonator, an external quadrupole field is applied to magnetize the ferrite, hence, the magnetization and RF fields are completely decoupled. Fig.2.2 shows the schematics of the TSR RF resonator, with an overall length of about 1 m. The

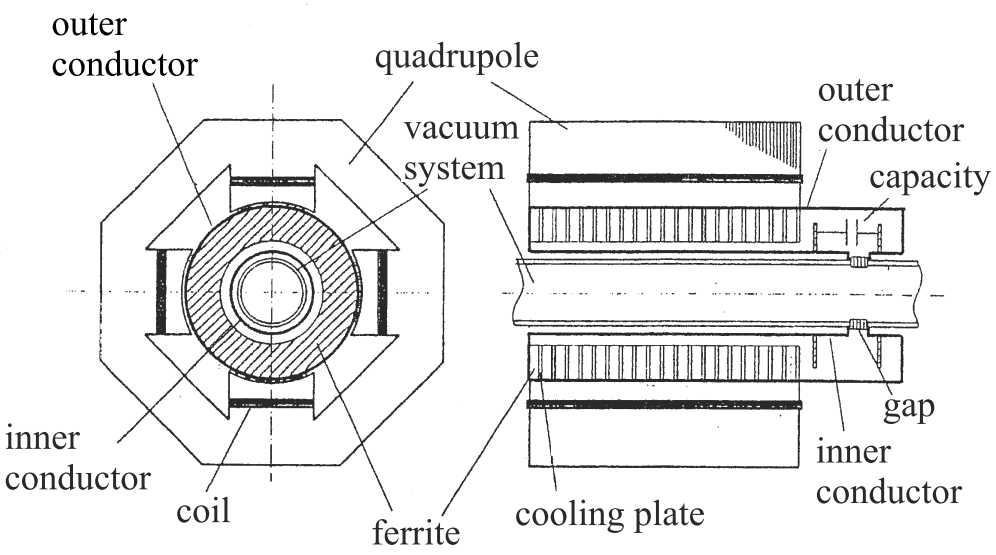

Figure 2.2: Schematics of the quadrupole ferrite-loaded RF resonator.

space between the inner and the outer conductor of the resonator is occupied with ferrite rings and cooper cooling plates. From electrical strength point of view, a certain vacuous area (radial dimension of 10 mm) is needed from the inner conductor to the copper cooling plates. The magnetic bias field is created by an external quadrupole with five bias windings on each pole. In order to reduce the requisite DC power the space between the ferrite rings and the quadrupole poles must be as small as possible. The mandatory voltages for

acceleration or deceleration of a multiturn injected ion beam ranging between 100-300 V, which are relatively small as compare to the resonator voltage of a post-accelerator and causes no problem to the high power consumption. The design criterion of the maximum voltage of 5 kV defined by the demand to ensure the adiabatic capture of a RF-stacked ion beam having a momentum spread of about 1 %. Varying the eigenfrequency is realized by changing the ferrite permeability with a DC magnetization field. Hence, enables energy ramping for heavy ion beams, covering a frequency range between 0.45 and 9 MHz with a fast tuning capability of about factor 9, along the entire range of magnetic rigidities of the storage ring in between 0.2-1.5 Tm. The magnetization field is produced by several bias windings mounted directly on the ferrite rings and connected to a regulated power supply. It provides the currents approximately up to 200 A.

2.2 Electron cooling

The beam properties of the stored ions can be substantially improved using an electron cooling process. If there is no cooling, the low-energy beam has a large emittance because the whole horizontal acceptance of the ring is filled with particles. An electron beam traveling at the same speed as the ion beam is deflected into the ring, where it accompanies the ion beam in its propagating direction for 1.2 m until being deflected out again. In case that, an individual ion deviates from this velocity, it is accelerated or decelerated by the electrons via Coulomb interaction over many revolutions until it possesses the desired velocity value. Statistically, the velocity distribution of the ion beam before and during electron cooling can be described in terms of a temperature which decreases with time until being in equilibrium with intrabeam scattering. The cooling effect shrinks the diameter of the ion beam from several centimeters to a few millimeters within a fraction of a second depending on the mass and charge state of the ions. The cooled beams are then utilized for in-ring experiments or extracted from the storage ring. The electron cooler is located in one of the four long straight sections of the ring. It consists of different components such as the gun, the non-evaporable getter(NEG) pump modules, the solenoidal and toroidal magnets, the titanium sublimation pumps, the position pick-ups, the collector, the pumping ports and the correction dipoles on the ring axis. The complete structure and the position of the electron cooler is shown in fig. 2.3. The interaction between electrons and ions takes place in the solenoid located in the center. The guide field of the electron beam from the electron gun to the collector is created by five solenoidal and two toroidal coils[11]. The gun solenoid coil is designed for a maximum magnetic field of 12 kG to allow an expansion of the electron beam. The other solenoids and toroids are designed for a maximum magnetic field of 3 kG in order to be able to study cooling with relatively strong magnetic fields. To allow steering of the beam the field direction in the main magnets can be changed by the superposition of transverse fields excited by a pair of dipole saddle coils. Although the length of a straight section in the TSR is 5.2 m, the space needed for the toroids and correction magnets to compensate the closed orbit deflection in the toroid magnets themselves limits the effective length of the cooling solenoid to 1.2 m. The aperture dimensions for the ion beam in the horizontal degree of freedom in the cooler solenoid and toroid is ± 100 mm. The field quality in the main cooler solenoid which is essential for a low electron temperature is ensured by precision windings as well as by powering seven sets of correction coils. With this scheme, the main square fluctuations

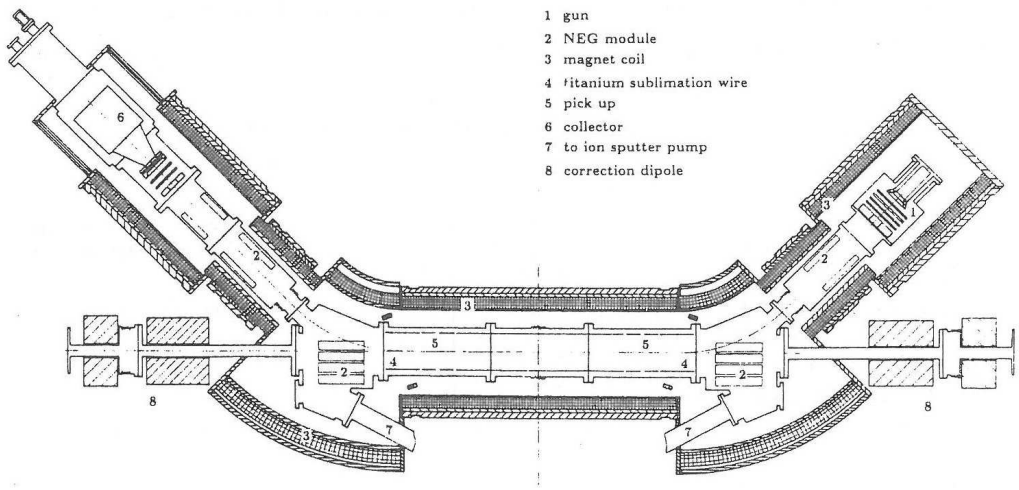

Figure 2.3: Schematics of the TSR electron cooler.

of the field direction $\sqrt{< B_t^2/B_l^2 >}$ were reduced to less than $4 \cdot 10^{-5}$ both horizontally and vertically for an effective length of the cooler region of 1.2 m. The cooler system is designed to operate in a heavy-ion ring in which low-energy even partially or fully stripped bare ions to be stored with lifetimes in the order of minutes. Therefore, a residual gas pressure of $5 \cdot 10^{-11}$ mbar or better had to be maintained also in the cooler where high gas loads from gun and collector are present. Besides the precaution in assembling the vacuum chambers from specially cleaned, vacuum fired and 300 °C bakeable components a high pumping speed is necessary, which is supplied by 34 (NEG) modules (15000 l/s) two 400 l/s and one 60 l/s sputter ion pumps.

2.3 Beam diagnostics

Non-destructive methods for the diagnostics of stored ion beams are important for the setup of in-ring experiments. A number of ion-beam properties can be monitored conveniently by observing the fluctuations of electronic signals induced by the ion beam in suitable pick-up electrodes. Thus, the generated Schottky noise spectrum corresponding to fluctuations of the total beam intensity, is commonly used to determine the longitudinal momentum spread of a coasting beam[12]. In some cases, the Schottky noise spectrum of a coasting beam induced in a transverse pick-up can provide information on the root-mean-square beam size, reflected by the amplitude of the betatron sidebands. However, for electron-cooled ion beams with small diameter and betatron oscillation amplitudes, this method fails as the sidebands become too weak to be detected. Hence, there seems to be no access to the transverse properties of such beams using the electronic pick ups.

Therefore, a monitoring device for the transverse density distribution of stored ion beams, based on the detection of ionization products of the beam particles in the residual gas, has been developed at MPIK[13]. As mentioned before, the heavy ion storage rings generally operate at a very low residual gas pressure in the order of 10^{-11} mbar. Nevertheless, a sufficient sensitivity and a large dynamic range for the detection of the ionization products, can be achieved by employing single-particle counting. With two

beam profile monitor (BPM) units of this kind, non-destructive, sensitive measurements of the horizontal and vertical profiles of stored ion beams can be performed with a spatial resolution of about 0.2-0.3 mm. Horizontal and vertical BPM(s) are used to determine the transverse beam temperature, to study transverse cooling and heating mechanisms, to observe the ion beam behaviour during experiments, and to determine the storage-ring parameters such as the dispersion function. The working principle of the BPM as shown

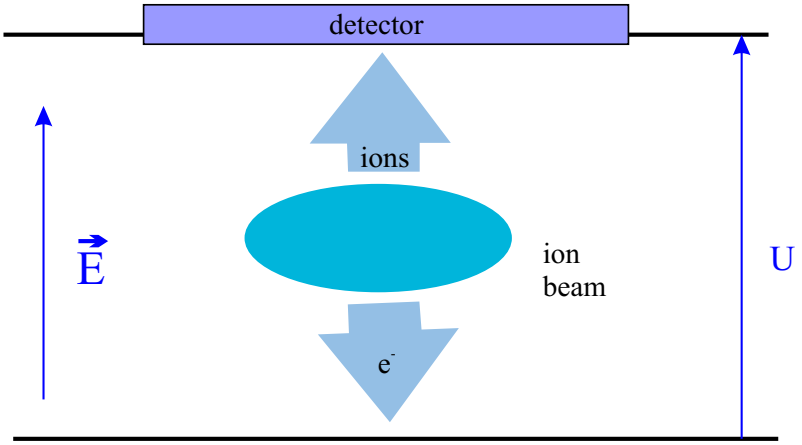

Figure 2.4: Principle of the residual beam profile monitor.

in fig. 2.4 is based on monitoring residual gas ions produced by the stored ion beam via distant ion-atom collisions which are then, accelerated by the electric field towards a position-sensitive detector mounted behind one of the plates. For that purpose, the circulating beam passes the free volume between two parallel plates, where a high voltage is applied to produce a homogeneous electric field perpendicular to the beam direction. Since the energies of the ions received in the collision are typically smaller as compared to those gained in the accelerating field a projection of the beam profile onto the detector is obtained, considering that the number of liberated residual-gas ions in a given volume is proportional to the density of the incident ion beam. The spatial resolution is limited, in principle, by the transverse(to the direction of the ion beam propagation) momentum transfer to the residual-gas ions during the ionization process and by the thermal motion of the residual gas, resulting in transverse velocity components $v_\perp$, which parallel to the metal plates, causes a lateral displacement Δx at the detector referring to the position where the ionization process took place. This displacement is given as following:

$$\Delta x = \sqrt{\frac{2M\Delta z}{eE}} v_\perp, \tag{2.1}$$

where M is the mass of a residual-gas ion, Δz is the initial distance between the residual gas ion and the detector, and E is the electric field strength in the detection volume. The detector is a chevron microchannel plate(MCP) assembly consisting of two plates in series. It provides an amplification of 10^7, necessary for electronic detection of single residual-gas ions impinging on the active surface. It operates over a wide range of count rates and allows for good spatial resolution.

Beam currents in particle accelerators are commonly measured by passing them through

the center of a toroidal transformer. The direct current transformer[8] is an active device utilizing strong, precisely controlled AC magnetizing forces applied to one or more toroidal cores to enable the sampling of a magnetic bias imposed by the beam or any other current. This category of devices is unique in the ability to measure a DC current component. The DC transformer operates in a zero average flux mode. Sensitive electronics detects any flux imbalance in the magnetic circuit and return a feedback current to precisely null that imbalance. When the initial flux is due to the magnetic bias induced by a beam current, the resulting feedback current will be directly proportional to that beam current. A stable, precision resistor in the feedback current path yields a voltage that serves as the output of the instrument. Practical DC transformers for particle beams are combinations of DC sections and AC transformers. This overcomes the aliasing inherent in any sampling circuit and extends the useful bandwidth of the system. DC transformers are utilized in synchrotron and storage rings where measurement of the DC components of bunched or coasting beams are important. These instruments can provide resolution and long-term stability at the level of one microampere. They are usually not appropriate for transport line applications and are relatively expensive for applications not requiring DC response. The current range of the DC transformer in the TSR is ± 10 mA at a resolution of 1 μA. The linearity error is about $\pm 0.005\%$, and zero drift is less than ± 4 μA in one hour.

3 TSR lattice and parameters

The first step in designing a storage ring is to choose an optimum pattern of focusing and bending magnets, the lattice. Magnets are classified according to the generated field into dipole magnets for beam orbit control, quadrupole magnets for beam size control, sextupole and higher-order multipole magnets for the control of chromatic and geometric aberrations. Before fixing the parameters, the practical difficulties of the magnets must be considered and the tolerances will be determined. The remnant field of a magnet may have quite a different shape from that defined by the pole geometry. Furthermore, steel properties may vary during the production of laminations. In addition, eddy currents in vacuum chambers and coils may perturb the linear field shape. Those are localized currents flowing in a conductor in response to changing the magnetic fields. Mechanical tolerances must ensure that asymmetries do not creep in. At high fields, it can be important that the linearity may deteriorate owing to saturation and variations in the packing factor.

The nominal energy defines the design orbit of a storage ring, which is a closed orbit of the ideal or so called reference particle. If all magnetic fields scale with the beam momentum, the closed orbit does not change. Particle motion with a small deviation from the closed orbit exhibits oscillations around the closed orbit.

3.1 Tune diagram and working point

In the storage ring, the transverse particle motion is subdivided into a closed orbit and a small-amplitude betatron motion around the closed orbit. The betatron oscillations are stable, transverse oscillations around the equilibrium orbit in the horizontal and vertical planes; it was first discussed for betatron accelerators. The restoring force for the oscillation is provided by the focusing magnetic field components that bend a particle which is off the equilibrium orbit bring it back to the equilibrium. The bending magnets in the lattice provide complete revolution of the particle beam, and this defines a closed orbit. Betatron oscillations are determined by the setting of quadrupoles in the lattice. The so-called tune is the number of betatron oscillations per revolution of the beam. Its magnitude is primarily a function of the quadrupole strength. The tune diagram is a plot of vertical tune values versus horizontal tune values with resonances usually shown as solid lines. Resonances are horizontal and vertical tune values at which field errors can cause beam losses in the storage ring. The working point is the point or region in a tune diagram where the storage ring normally operates. The tune diagram[1] and the normal working point of the TSR in the standard operational mode considering superpediodicity 1 and including up to the 4^{th} order resonances are shown in fig. 3.1[2], where the resonances

[1] A fragment of the tune diagram is shown for both tune intervals from 2.5 to 3.0.

[2] Note that, the same descriptions are valid for all the tune diagrams which are shown in different chapters throughout the thesis.

are indicated as: 1^{st} order - black[3], 2^{nd} order - blue[4], 3^{rd} order - red, 4^{th} order - green lines. Ideally, actual operational position of the beam can be plotted on the tune diagram as a (working) point. But, due to the chromaticity and a certain momentum spread of the beam, it is perceptive to give a finite length ΔQ to the working point, in reality, it is a working line. In general, the resonances occur in the tune diagram with the following

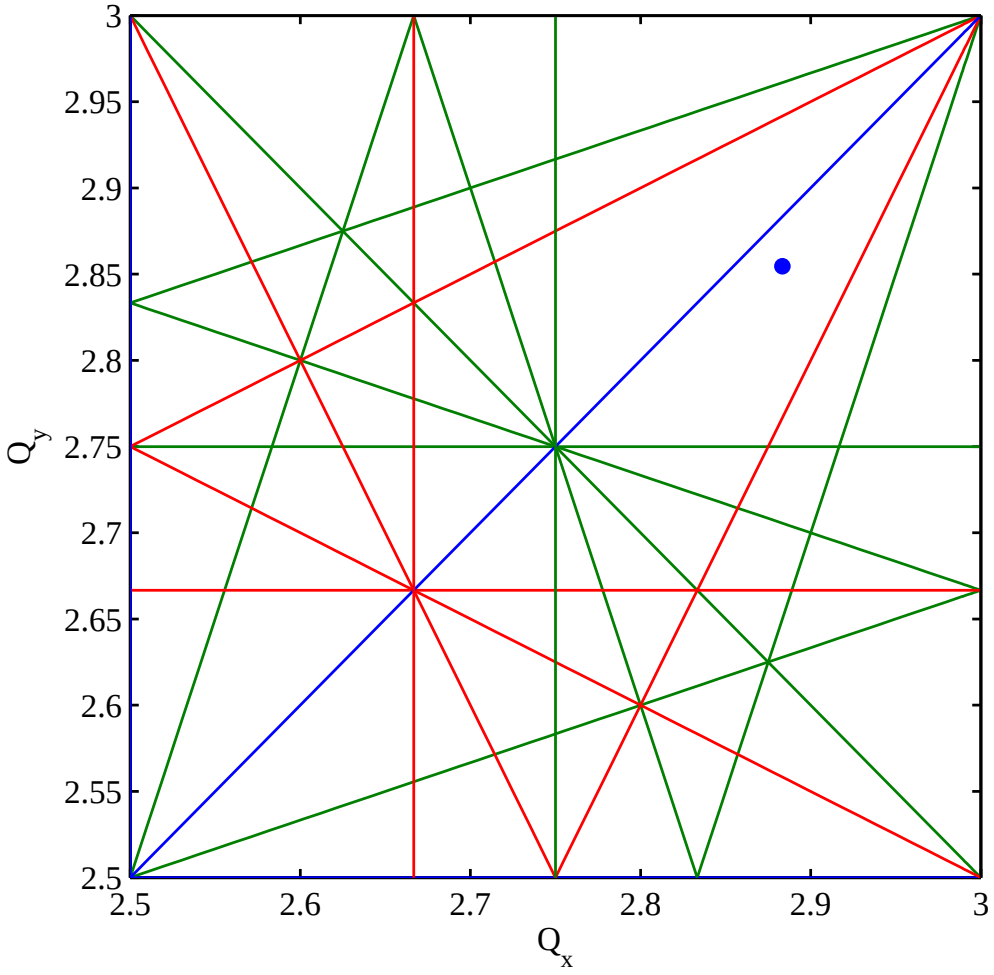

Figure 3.1: The resonances are indicated as colored, solid lines of 1^{st} order - black, 2^{nd} order - blue, 3^{rd} order - red, 4^{th} order - green lines.

equation:

$$lQ_x + mQ_y = p, \tag{3.1}$$

[3]In this fragment of the tune diagram black lines are shown on the right, as a vertical framing line and on the top as a horizontal framing line.

[4]Similarly, two more the 2^{nd} order resonances are shown on the left, as a vertical and on the bottom, as a horizontal framing lines.

where $|l| + |m| = n$ is the order of the resonances and p is the azimuthal frequency which drives it. This equation defines a set of lines in the tune diagram for each order of resonance and for each value of the integer p[14]. The n order determines the spacing of resonances in the tune diagram. For example, 3^{rd} order resonances converge on a point, which occurs for every $\frac{1}{3}$ of the integer tune value, including the integer itself. Somehow, by careful adjustment of the quadrupoles in the lattice and by keeping the tune spread (chromaticity) small, the beam must be coaxed up to full energy without hitting the lines.

Resonances and stopband width

"Resonance" in storage rings and accelerators means "betatron resonance". They occur when some perturbing force in the machine distorts the orbit in a periodic way, causing the betatron oscillations to grow larger and larger, until the beam is lost or perhaps extracted. The tune value does not have to be exactly on a resonance line for the resonance to affect the beam. Within a band around the resonance line, multipole fields can perturb the tune sufficiently enough to lock it on to resonance and may cause a resonant beam loss. This is the origin of the term "stopband width". The stopbands of various resonances have different widths proportional to the strength of the imperfection which drives it, so that the beam reaches resonance as the offending tune approaches. When a particle encounters the multipole field error at a certain phase, it gets an additional kick which induces increments in phase and amplitude. Over one turn, the tune changes by certain amount from an unperturbed tune value and on each turn by $2\pi\cdot$(fractional part of the tune) while it oscillates in a band around the mean value. In actual storage rings or accelerators, the magnetic field errors are unavoidable. Therefore, the closed orbit and the betatron motion will be perturbed. The nonlinear resonances are driven by nonlinear multipole field errors. Dipole perturbations excite 1^{st} order, which is the strongest resonance in a storage ring and therefore, integer tune values should be avoided. Quadrupole perturbations excite 2^{nd} order resonances and, thus, half-integer tune values should be avoided as well. Sextupoles excite 3^{rd} order, octupoles 4^{th} order resonances and so on.

A resonant beam loss is not relevant in the TSR operation in the standard mode at the normal working point (indicated in fig. 3.1), where the tune is far from resonances. If the working point shifts away from the original tune value and the beam crosses over resonances, there will definitely be beam losses, which is also discussed in the next chapter. Therefore, the knowledge of the resonance stopbands in the TSR tune diagram are important and are estimated experimentally. To assess the particle loss by resonances, the measurements are performed for a beam having a large momentum spread.

The experimental setup is shown schematically in fig. 3.2. It consists of a noise source and a frequency mixer which is connected to the TSR resonator by a RF switch. The mixer is a frequency-translating device which implies a nonlinear electrical circuit that creates new frequencies from the sum and difference of two frequencies applied to it. They are widely used in most RF communication equipment to shift the frequency range.

The experiments are performed in the following procedure:

- rectangular, uniform noise distribution with a width of 20 kHz is generated by software and sent to the port R of the frequency mixer via jack connection of the PC load speaker;

- the RF frequency f_L is given to the port L of the frequency mixer, and the sum and difference of two frequencies will be obtained from the intermediate frequency output

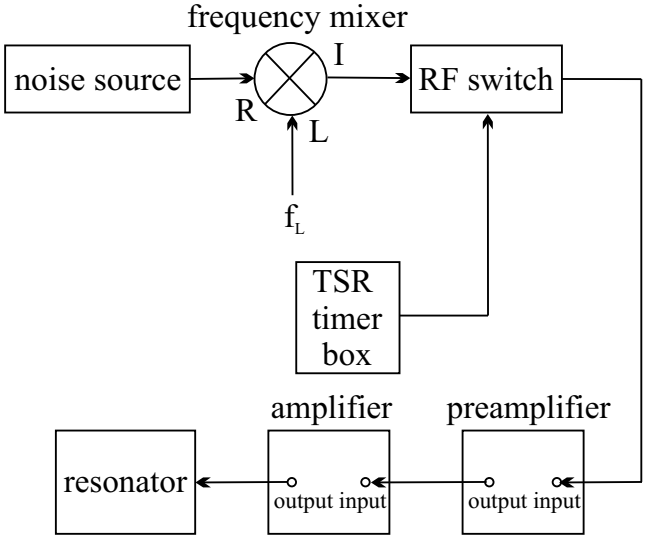

Figure 3.2: Schematics of the setup for stopband width measurement.

port I;

- duration of the noise is set for 1.5 s at the TSR timer box, which is connected to the RF switch to control it using a TTL signal; TTL is a type of binary electrical signal based on the transistor-transistor-logic (TTL) standard. It has only two, low and high voltage levels which are 0 and 5 volts, respectively.

- the output signal coming from the port I passes through the RF switch while it is on and will be applied to the beam via the RF resonator for duration of 1.5 s.

In fig. 3.3 the ideal distribution and the generated profile of the noise measured directly from the output of the mixer within the frequency span of 3.08-3.104 MHz is shown, where the central frequency corresponds to the fifth harmonics of the beam revolution frequency. The comparison shows that, despite of the edges' slight deviations, the assigned output signal level is well-achieved and thus can be used in actual operation. The 1^{st} and the 2^{nd} order resonances are known to be the strongest and they can not be measured properly. Therefore only 3^{rd} and 4^{th} order resonances are studied with $^{12}C^{6+}$ ions. The frequency spread with Schottky noise diagnostics is measured with a realtime spectrum analysator (RSA 3303A).

Initially, the noise is applied to the beam at the normal working point Q_1 of the TSR (indicated in fig. 3.1) which is set in the resonance-free region and frequency spread of the beam is measured. The closest resonance to this working point is a diagonal blue line so called coupling resonance, which only couples horizontal and vertical degrees of freedom, and thus, does not lead to beam loss. The beam profile is shown in fig. 3.4 without the effects of resonances where the measured momentum spread is $\Delta p/p$=9·10^{-3}. When the normal working point of the TSR shifts away[5] at high intensities, the 4^{th} and the 3^{rd} order resonances are to be crossed over. Therefore, to estimate the consequences of the 4^{th} order resonances of the beam, the working line is set in the region of Q_2, where 4^{th} order resonances exist. Measured frequency spread of the beam is shown in fig. 3.5. It takes a few minutes to detect the resonant beam loss caused by the 4^{th} order resonances. The

[5]Discussed in the next chapter.

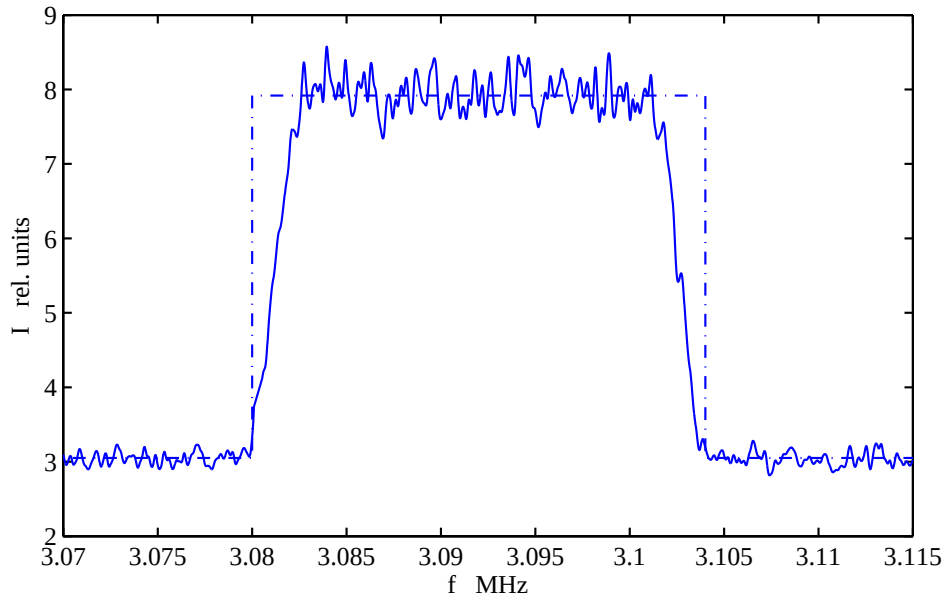

Figure 3.3: Ideal distribution and the generated noise profile measured directly from the mixer output.

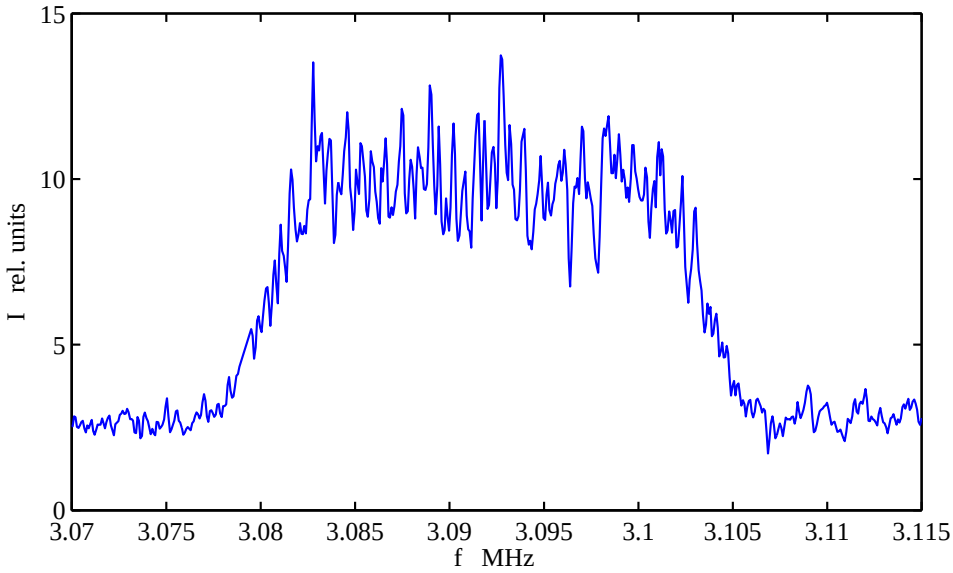

Figure 3.4: Measured frequency spread of the stored ion beam at the resonance-free region, around $Q_1(2.892,\ 2.856)$.

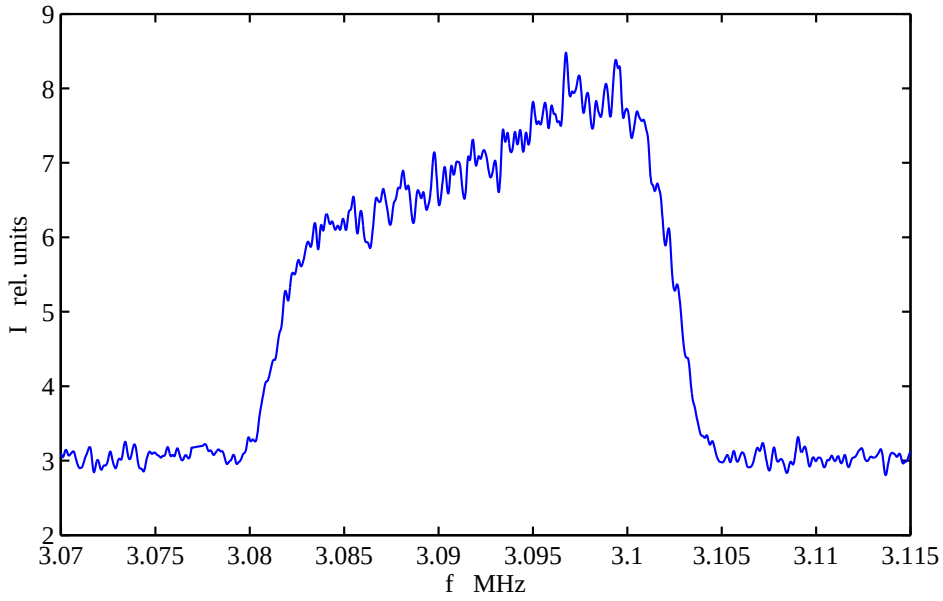

Figure 3.5: Measured frequency spread of the stored ion beam interacting with the 4^{th} order resonances around $Q_2(2.774, 2.738)$.

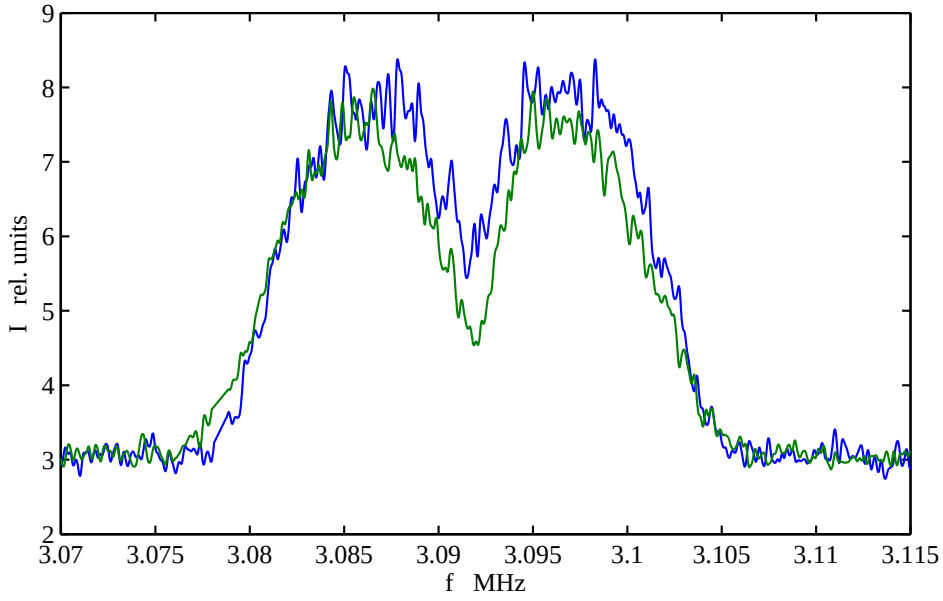

Figure 3.6: Measured frequency spread of the stored ion beam interacting with the 3^{rd} order resonances around $Q_3(2.877, 2.750)$ measured in 5 s (blue line) and in 8 s (green line) after injection.

beam loss can be seen in the change of the frequency spread as compared to the previously measured distribution (see fig. 3.4). The 3^{rd} order resonances are stronger than 4^{th} order and can cause instant beam loss. Therefore, to investigate the effect of this resonance the working point is set Q_3. A fast beam loss in 5 and 8 seconds are observed after injection due to a strong resonance stopband, it appears as a downward dip in the measured frequency spread as shown in fig. 3.6. The stopband of the resonance is obviously dividing the beam profile into two parts around the center.

With the following parameters[6] such as Schottky frequency (f=3.09233 MHz), phase-slip factor (η=0.91) and chromaticities (Q'_x=-7.29, Q'_y=-4.1), the measured frequency spread Δf converted into the tune spread ΔQ, and so-called working lines are determined for all the measurements. Length of the lines is defined by the tune spread of the

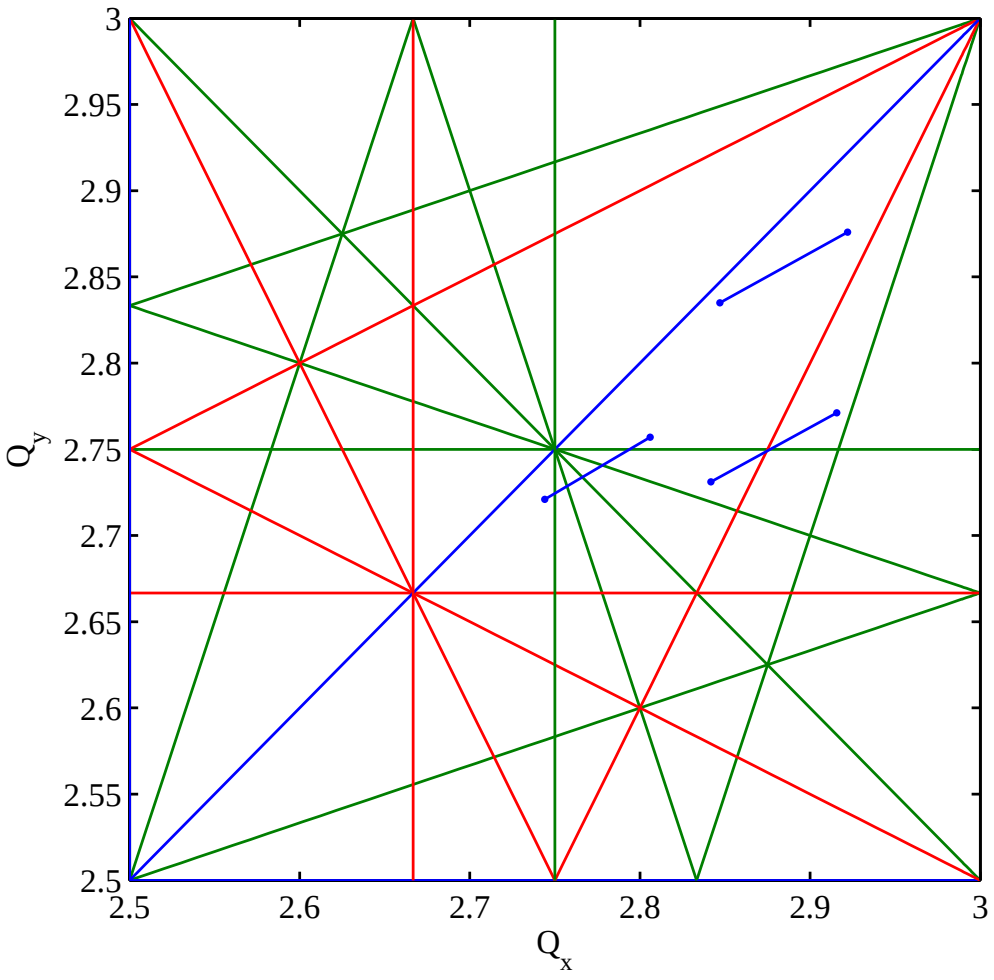

Figure 3.7: Working lines where Q_1(2.892, 2.856) as a reference and Q_2(2.774, 2.738), Q_3(2.877, 2.750) where the beam and resonance interactions are investigated.

[6]Also discussed in this chapter

beam, calculated from the following equation:

$$\Delta Q = Q' \cdot \frac{\Delta f / f}{\eta}. \tag{3.2}$$

Fig. 3.7 shows visible indications of the three different working lines, in which the stopband width measurements are conducted with 3^{rd}, 4^{th} order resonances as well as in resonance-free region as a reference. Analysis of the motion in phase space of working lines Q_1 and Q_3 are schematically explained in fig. 3.8. With multiturn injection the acceptance of the TSR will be covered and all phase space trajectories will be elliptical. If the working line Q_3 is near to the 3^{rd} order resonance it deforms the phase space into a triangular shape, characterized by the 3^{rd} order resonance. The separatrix is the boundary of stable motion, which is shown as the dashed triangular green line. The solid green circle inside the separatrix represents the stored ion beam, which means the motion is linear and stable for all the amplitudes. The dimensions of the separatrix characterized by its size, are determined by the distance between the unperturbed tune Q and the resonance value. As resonance approaches ΔQ shrinks, the separatrix size becomes smaller and particles are squeezed out along the three sides of the separatrix. The theory taking into account the perturbation in the amplitude defines the separatirix as triangular in shape with the three sides to which particles cling on their way out of the machine. If the strong resonance is close, size of the separatrix becomes smaller, meaning the stable area is smaller and turns into a point during the resonance. Outside the separatrix, the motion tends to be *chaotic*, because small changes in the initial conditions for the motion can lead to large changes after many turns. The radial distance from the center to separatrix is a measure of the maximum amplitude of the stable motion.

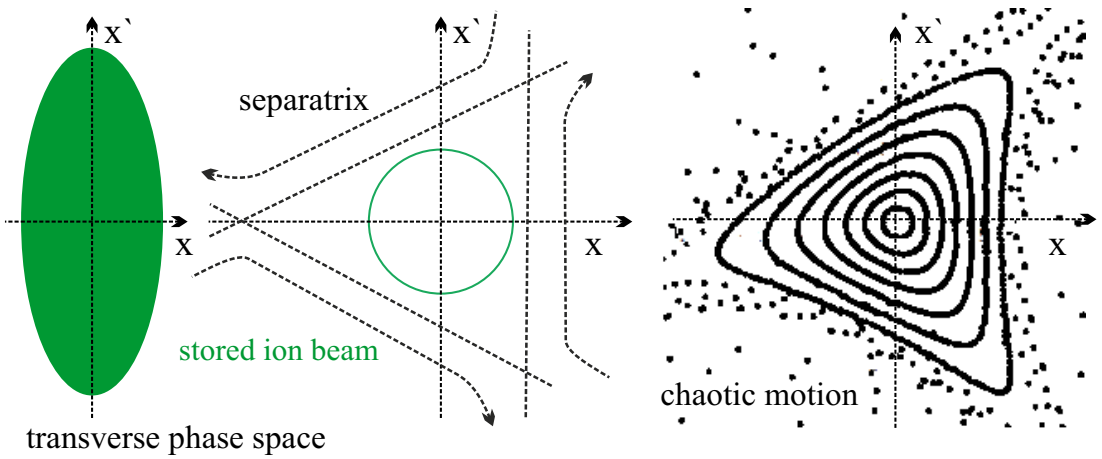

Figure 3.8: Populated transverse phase space after multiturn injection, the separatrix and stored ion beam. The beam loss and chaotic motion.

The experiment with the stopbands is not meant for estimating the absolute resonant beam losses, but it is used to explain the limitations in accumulating high intensity beams. Beam induced fields and space-charge effects cause an incoherent tune shift which moves the working point down in the diagonal direction crossing over resonances, so that,

resonance beam losses become relevant in the TSR operation at high intensities. These studies are only to demonstrate illustratively, the effects of the resonances on the beam. In the present investigation using $^{12}C^{6+}$ ions the resonant beam losses found to be significant especially when crossing the 3^{rd} order resonance stopband width. These results are applied for the incoherent tune-shift studies, which are discussed in chapter 4.3.

Beam transfer function

Studying the beam stability by using an external sinusoidal excitation was pioneered by the Midwestern Universities Research Association (MURA) group[15]. Later, the theoretical link between an excitation and the beam response, or so-called beam transfer function (BTF), as well as the theory of coherent instabilities was established[16], and practical demonstrations were made on how to excite the beam. Either a network analyzer with a swept frequency can be used, or the beam can be excited by white noise where the response is measured with FFT spectrum analyzer. The beam transfer function technique developed into a widely used and convenient operational instrument for optimizing the beam stability[17], to measure the wall impedance and the betatron tune values (working point) across the stack[18], to monitor feedback systems, to observe resonances and to minimize beam to beam couplings. Measurements of the beam response while the beam is excited transversely and dividing the response signal by the reference yields the BTF.

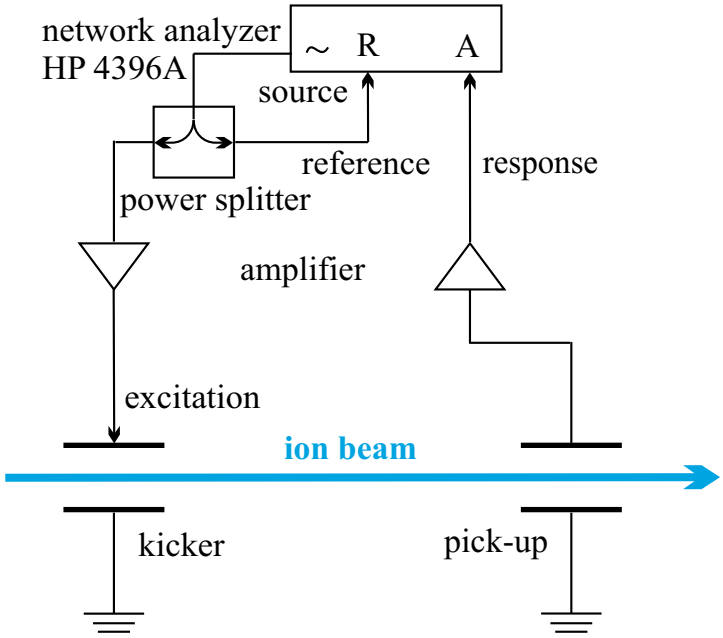

Figure 3.9: Setup of the BTF measurement.

BTF measurements are used to determine the horizontal and vertical tune by horizontal and vertical excitement of the beam with a RF field. The excitation frequency satisfies the following equation:

$$f_{x,y} = f_0(n \pm q), \tag{3.3}$$

where n is an integer number and q is the non-integer part of the tune. The revolution frequency f_0 is measured by Schottky noise diagnostics.

Setup of the BTF measurement at the TSR, is composed of a network analyzer (HP 4396A), power splitter, amplifiers, a kicker and a pick-up, as shown in fig. 3.9. The connection of the TSR and source (network analyzer HP 4396A) is provided by kicker and pick-up. The excitation signal, generated by the network analyzer, is sent to a power splitter in which divided into two output signals. One of the output signals passes through the amplifier and is applied to the kicker where one electrode is grounded. The transverse field is created to excite the beam and the other output signal from the power splitter is used as a reference. The response of the beam is detected with the pick-up, amplified and sent to the network analyzer. Vertical and horizontal BTF measurements in the standard operational mode are shown in fig. 3.10 and fig. 3.11. From the f_x, f_y resonance frequencies, the tune values ($Q_x = 2.883$, $Q_y = 2.854$) of the working point (indicated in fig. 3.1) are obtained.

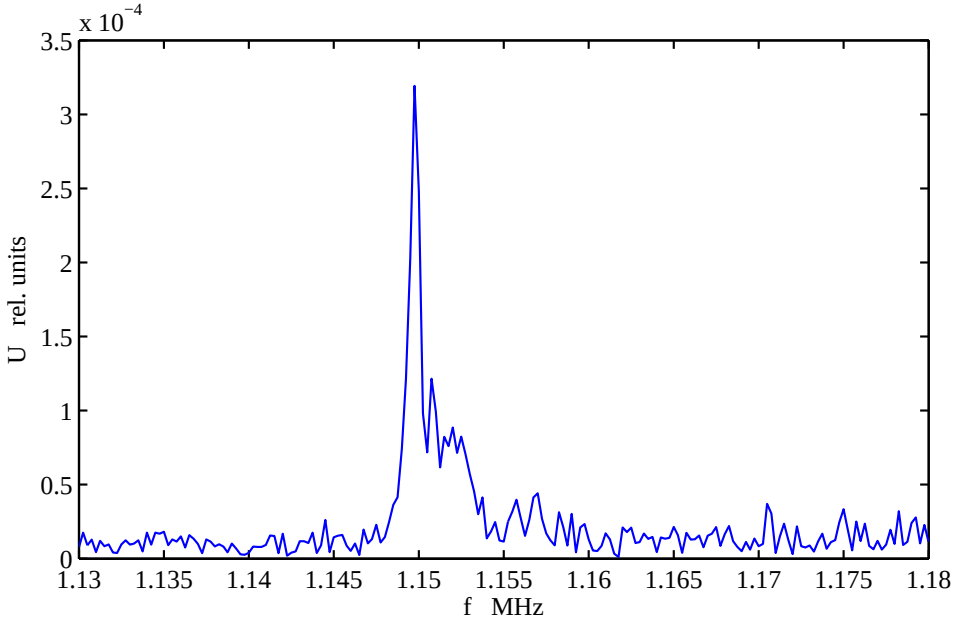

Figure 3.10: Vertical BTF measurement.

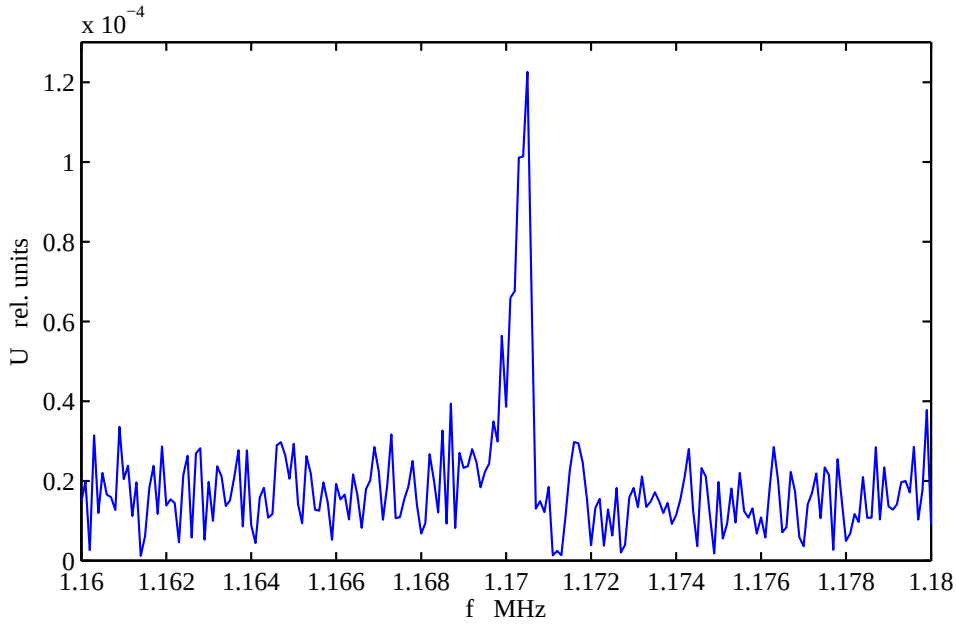

Figure 3.11: Horizontal BTF measurement.

3.2 Phase slip factor and the momentum compaction

To determine the momentum spread of the beam from the measured revolution frequency distribution, the slip factor of the storage ring must be known. The slip factor η of a storage ring is defined as the ratio of the following two quantities:

$$\eta = \frac{\frac{\Delta f}{f}}{\frac{\Delta p}{p}}, \tag{3.4}$$

where $\Delta f/f$ is the ion revolution frequency spread and $\Delta p/p$ is the longitudinal momentum spread of the stored ion beam. A consequence of the change in the ion momentum results to a closed orbit shift and the η parameter will be smaller than 1. The revolution frequency can be determined from the ion velocity v and circumference C of the storage ring with the following relation:

$$f = \frac{v}{C}. \tag{3.5}$$

The relative change of the revolution frequency is:

$$\frac{\Delta f}{f} = \frac{\Delta v}{v} - \frac{\Delta C}{C}. \tag{3.6}$$

By inserting eq. 3.6 into eq. 3.4, the following equation is obtained:

$$\eta = \frac{\frac{\Delta v}{v}}{\frac{\Delta p}{p}} - \frac{\frac{\Delta C}{C}}{\frac{\Delta p}{p}}. \tag{3.7}$$

It can be shown that:

$$\frac{\frac{\Delta v}{v}}{\frac{\Delta p}{p}} = \frac{1}{\gamma^2}, \tag{3.8}$$

where γ is the relativistic mass increase. In the non-relativistic approach, the ion mass is constant: $\frac{\frac{\Delta v}{v}}{\frac{\Delta p}{p}} = 1$. The momentum compaction factor α is a constant parameter defined by:

$$\alpha = \frac{\frac{\Delta C}{C}}{\frac{\Delta p}{p}} = \frac{1}{\gamma_{tr}^2}, \tag{3.9}$$

where γ_{tr} is the so-called transition gamma. By inserting the eq. 3.9 and the eq. 3.8 into the eq. 3.7, the slip factor can be calculated from the following equation:

$$\eta = \frac{1}{\gamma^2} - \frac{1}{\gamma_{tr}^2}. \tag{3.10}$$

At the transition energy $\gamma = \gamma_{tr}$ the slip factor is η=0. Below the transition energy $\gamma < \gamma_{tr}$, with η >0, a higher momentum particle will have a revolution period shorter than that of the synchronous particle. Because a high-energy particle travels faster, its speed over compensates its longer path length in the accelerator, so that it will arrive at a fixed location earlier than a synchronous particle. Above the transition energy, with $\gamma > \gamma_{tr}$, the converse is true. At $\gamma = \gamma_{tr}$ the revolution period is independent of the particle momentum and all the particles at different momenta travel firmly around the accelerator with equal revolution frequencies. This is called the isochronous condition.

Measurements of the momentum compaction factor

The compaction factor can be determined by applying a relative change for all the magnetic fields[7] of the TSR. In this method, the momentum of the stored ions will be kept constant and all the magnetic fields are changed by $\frac{\Delta B}{B}$ using the ramp program of the TSR. The magnetic field changes has the same effect on the closed orbit as momentum change by $\frac{\Delta p}{p}$ if (see appendix A):

$$\frac{\Delta B}{B} = -\frac{\Delta p}{p}. \tag{3.11}$$

Because the length of the closed orbit is given by:

$$C = \frac{v}{f}, \tag{3.12}$$

the relative change of the closed orbit is:

$$\frac{\Delta C}{C} = \frac{\Delta v}{v} - \frac{\Delta f}{f}. \tag{3.13}$$

[7] "All the magnetic fields" implies the magnetic field of the storage ring is composed of different magnetic fields such as dipole, quadrupole and sextupole fields.

Since the velocity is constant during the actual experiment, the relative change of the closed orbit can be written as:

$$\frac{\Delta C}{C} = -\frac{\Delta f}{f}. \tag{3.14}$$

By inserting eq. 3.14 and eq. 3.11 into eq. 3.9, the momentum compaction factor can be calculated from the following equation:

$$\alpha = \frac{1}{\gamma_{tr}^2} = \frac{\frac{\Delta f}{f}}{\frac{\Delta B}{B}}. \tag{3.15}$$

The fractional change of the revolution frequency is measured by Schottky noise diagnostics. The measurements are shown in fig. 3.12. From the slope of the linear fit through the data, the ratio $\frac{\Delta f}{\Delta B/B}$=0.2655 MHz is obtained, where the main dipole field is 5979.8 gauss and the momentum compaction factor $\alpha = 0.0857$ is calculated. From eq. 3.10 the

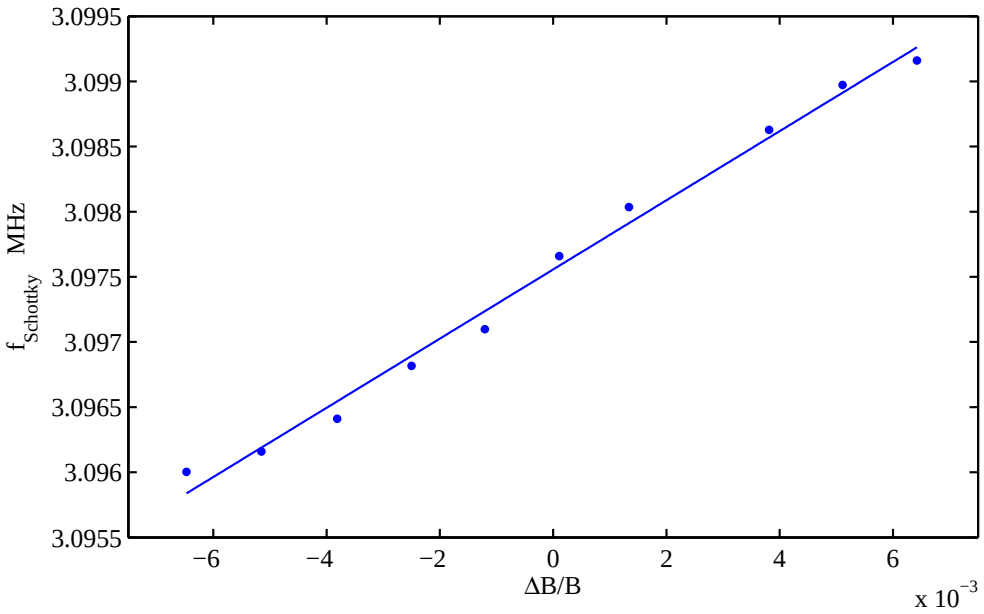

Figure 3.12: Schottky frequency of the $^{12}C^{6+}$ ion beam (h=5) as a function of the variation of all the magnetic fields.

slip factor can be calculated as:

$$\eta = 0.901,$$

where $\gamma_{tr} = 3.416$ and $\gamma = 1.0066$. Previously, the slip factor of the TSR was determined based on the measurement of the momentum compaction factor as a function of the change of the main dipole field only. This satisfies the fact that in the first order, the relative change of all the magnetic fields can be replaced by the change of the main dipole field only. Applying this approximate method measurements performed, which are shown in fig. 3.13. The ratio $\frac{\Delta f}{\Delta B} = 4.3821 \cdot 10^{-5}$ MHz/gauss is determined from the slope of the fit.

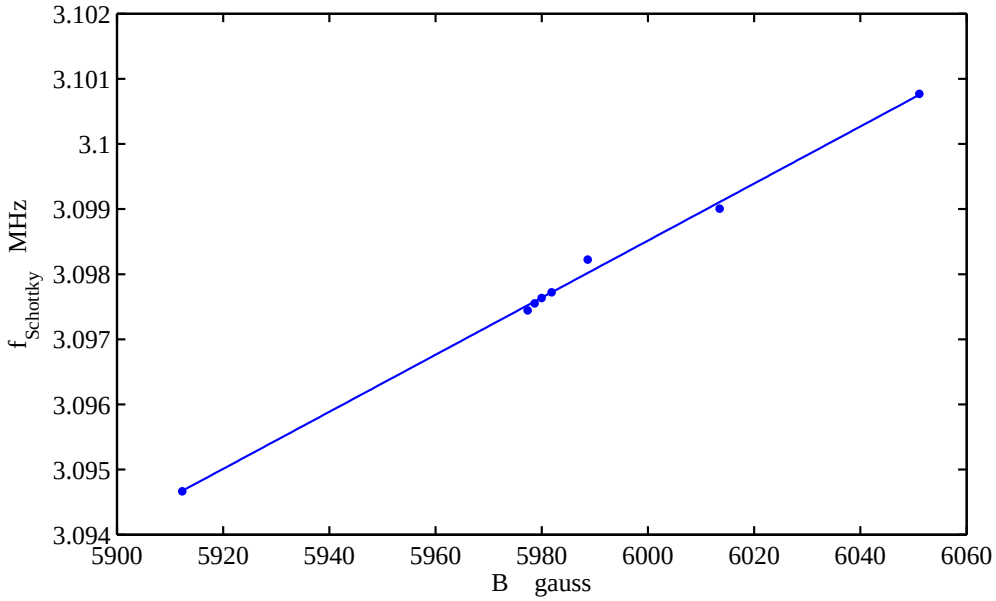

Figure 3.13: Schottky frequency of the $^{12}C^{6+}$ ion beam (h=5) as a function of the main dipole field.

From eq. 3.15 the momentum compaction $\alpha = 0.0847$ and from eq. 3.10 the slip factor are calculated:

$$\eta = 0.923,$$

where $\gamma_{tr} = 3.4368$ and $\gamma = 1.0066$. The momentum compaction factor is determined with two different methods and the slip factor, one of the main parameters which is important for further analysis is calculated, accordingly. The results of both methods agree with each other within 2%.

3.3 Chromaticity

The chromaticity Q' of the storage ring characterizes the dependency of the tune Q from the ion momentum shift:

$$Q' = \frac{\Delta Q}{\frac{\Delta p}{p}}. \tag{3.16}$$

Chromaticity, in generally, not desirable in a machine, for at least following two reasons:

- there is always a spread in momentum, then there is spread in tune due to chromaticity. If large enough, this tune spread could put some of the particles dangerously close to resonances.

- A collective instability[8] depends on the value of the chromaticity. To calculate the

[8] At high energy machines

chromaticity of the storage ring the focusing strength k of a quadrupole is considered:

$$k = \frac{1}{B\rho}\frac{dB_y}{dx}, \tag{3.17}$$

where $B\rho$ is the beam rigidity and $\frac{dB_y}{dx}$ is the quadrupole gradient. Because $B\rho = \frac{p}{q}$, the finite momentum spread $\frac{\Delta p}{p}$ of the ions cause a change in the focusing strength:

$$\frac{\Delta k}{k} = -\frac{\Delta p}{p}, \tag{3.18}$$

resulting in a tune shift:

$$\Delta Q \propto \frac{\Delta p}{p}. \tag{3.19}$$

Replacing the proportionality by an equality and by considering eq. 3.18, the tune shift can be written as[19]:

$$\Delta Q = \frac{1}{4\pi}\int \beta(s)\Delta k(s)\,\mathrm{d}s = \Big(-\frac{1}{4\pi}\int \beta(s)k(s)\,\mathrm{d}s\Big)\frac{\Delta p}{p}. \tag{3.20}$$

A comparison with expression 3.16 allows to calculate the chromaticity with the following equation:

$$Q' = -\frac{1}{4\pi}\int \beta(s)k(s)\,\mathrm{d}s. \tag{3.21}$$

In the storage ring β function will reach its maximum value in a focusing quadrupole, where $k(s)$ >0, therefore the chromaticity of any storage ring, containing only dipoles and quadrupoles is always negative. This chromaticity is called the natural chromaticity.

Chromaticity measurements

The common method to determine the chromaticity of the storage ring is to measure the tune of the stored particles as a function of their momentum variation. It is conveniently realized with the electron beam of the electron cooler. Introducing an energy mismatch between ions and electrons will result in an ion-beam momentum variation $\frac{\Delta p}{p}$, which can be measured via Schottky noise diagnostics. Horizontal and vertical tune measurements as a function of the Schottky frequency are shown in fig. 3.14 and fig. 3.15, relatively. From eq. 3.4 with the measured Schottky frequency for a 73.3 MeV $^{12}C^{6+}$ ion beam and using the known slip factor of the TSR, the momentum can be calculated. The ratios $\frac{\Delta Q_{x,y}}{\Delta f}$ are determined from the slope of the fits through the data, accordingly. From that, the obtained horizontal and vertical mean chromaticities are:

$$\overline{Q'_x} = -7.3$$

$$\overline{Q'_y} = -4.1.$$

Based on the eq. 3.11, the new method is tested to determine the chromaticity. The

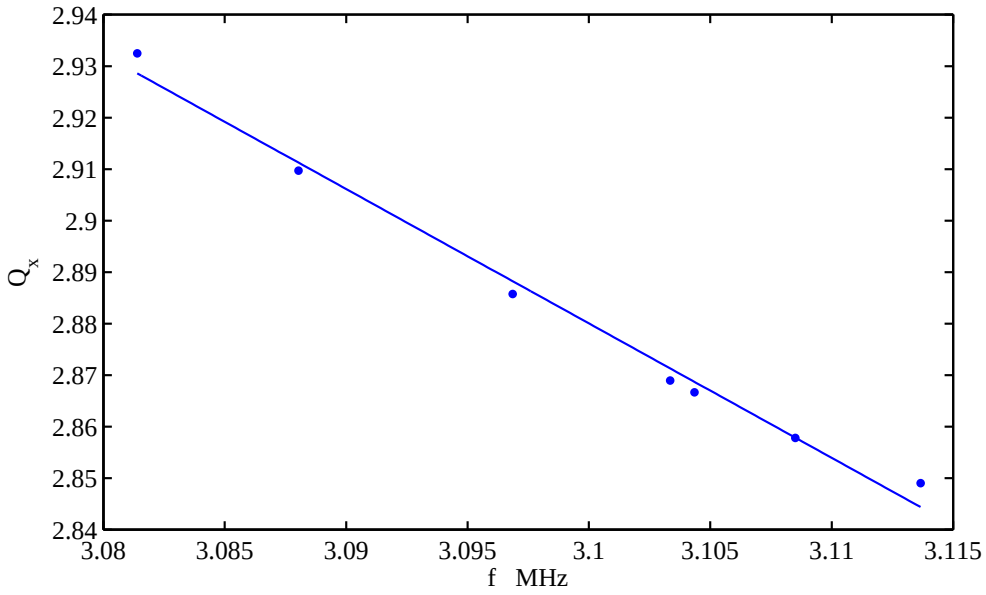

Figure 3.14: Horizontal tune as a function of the Schottky frequency measured by changing the ion momentum with the electron cooler.

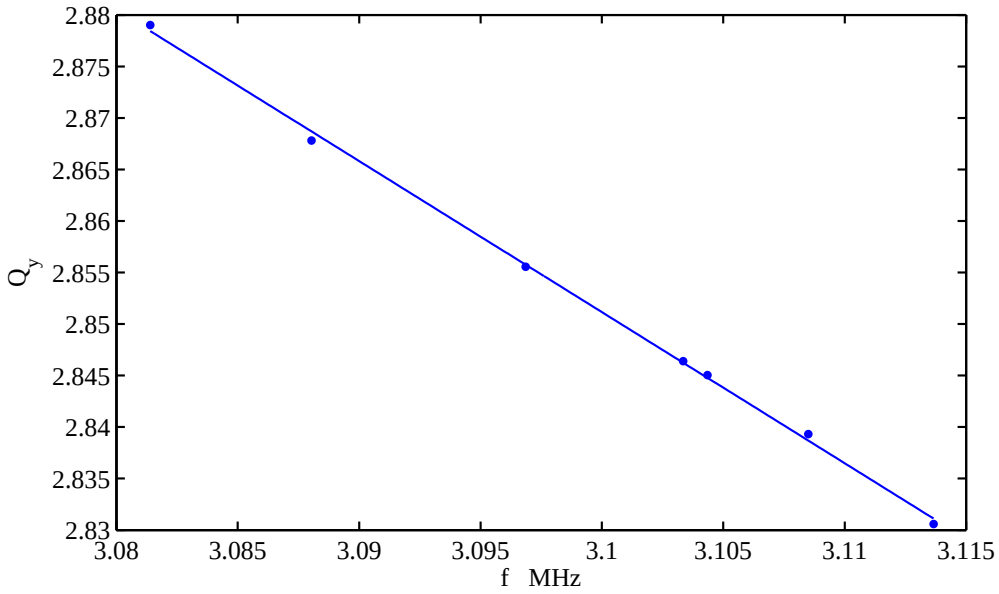

Figure 3.15: Vertical tune as a function of the Schottky frequency measured by changing the ion momentum with the electron cooler.

horizontal and vertical tune dependency on the variation of all the magnetic fields of the TSR are measured, then, the chromaticity can be calculated from the following expression:

$$Q' = -\frac{\Delta Q}{\frac{\Delta B}{B}}. \tag{3.22}$$

The magnetic fields are changed by $\frac{\Delta B}{B}$ as described above, using the ramp program and the corresponding tune values are shown in fig. 3.16 and fig. 3.17. The ratios $\frac{\Delta Q_{x,y}}{\Delta B}$ are determined from the slope of the fits through the data. The calculated mean chromaticity values are:

$$\overline{Q'_x} = -8.4$$

$$\overline{Q'_y} = -4.5.$$

The horizontal and vertical chromaticities are slightly different as compared to the values from the previous method.

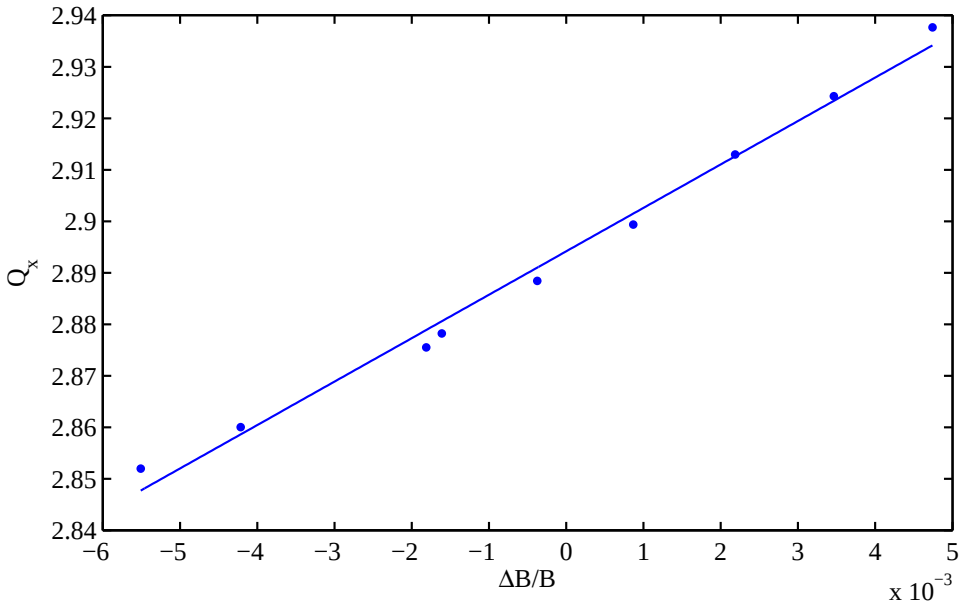

Figure 3.16: Horizontal tune as a function of the variation of all the TSR magnetic fields.

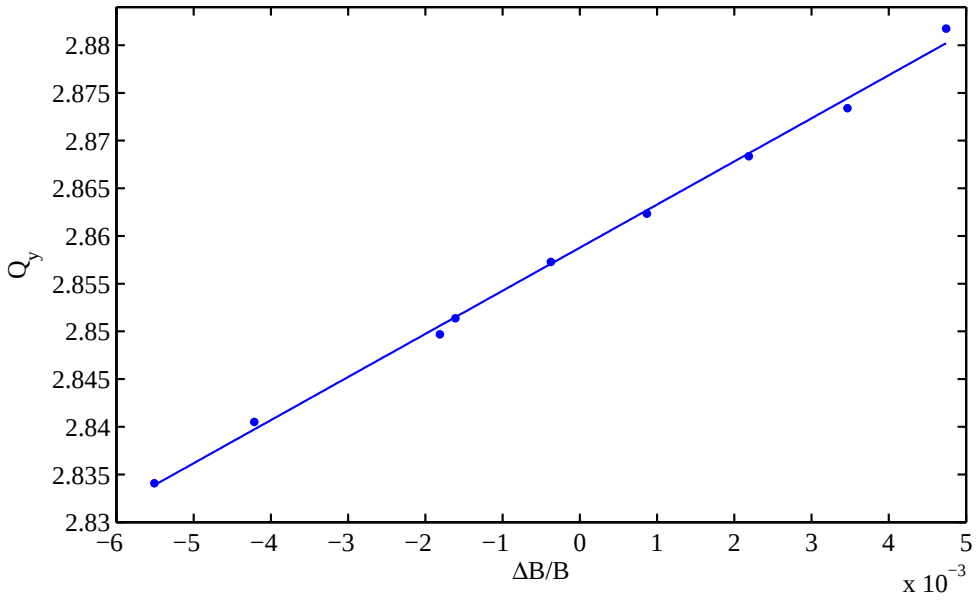

Figure 3.17: Vertical tune as a function of the variation of all the TSR magnetic fields.

3.4 Dispersion

The bending angle of the dipole depends on the momentum of the particle p. Thus, the resulting closed orbits will also depend on Bρ, particles with higher momenta are bent less, have a larger radius of curvature in the guide field, and their closed orbit has a larger mean radius. As a result, they do no longer pass axially through the quadrupoles and, therefore, are subject to focusing forces. Each time an off-momentum particle passes through a bending magnet it gets an additional kick with respect to the reference particle, which can be expressed as an additional term on the right in Hill's equation[20]:

$$\frac{d^2x(s)}{ds^2} + k(s)x = \frac{1}{\rho(s)}\frac{\Delta p}{p}, \tag{3.23}$$

where $\rho(s)$ is the radius of curvature of the equilibrium orbit as a function of s, the path along the ring and at the point s, $\frac{1}{\rho} = 0$ outside dipoles. The closed orbit for a zero betatron amplitude particle with a momentum $p_0(1 + \frac{\Delta p}{p})$ is displaced from the central p_0 orbit by an amount of:

$$\Delta x(s) = D_x(s)\frac{\Delta p}{p}, \tag{3.24}$$

where $D_x(s)$ is called a dispersion, which is a lattice function varies along the path s. Only in the first order calculation (see eq. 3.23) the closed orbit shift is proportional to the momentum shift. In general the closed orbit shift can be given by a Taylor expansion:

$$x = x_0 + D_x(s)\frac{\Delta p}{p} + \frac{1}{2!}D_{(x)2}(s)\left(\frac{\Delta p}{p}\right)^2 + ... + \frac{1}{8!}D_{(x)8}(s)\left(\frac{\Delta p}{p}\right)^8 ... , \tag{3.25}$$

where $D_x(s)$ is the dispersion function determined from the linear particle motion. If the momentum distribution of the beam can be described by a gaussian function with the σ value, the measured horizontal $\sigma_{m,x}$ beam width is:

$$\sigma_{m,x}^2 = \sigma_x^2 + \left(D_x \frac{\Delta p}{p}\right)^2. \tag{3.26}$$

Due to the dispersion and momentum spread of the beam, the measured beam width $\sigma_{m,x}$ is larger than the beam width σ_x related to the beam emittance ϵ_x describing the betatron motion:

$$2\sigma_x = \sqrt{\beta(s) \cdot \varepsilon}, \tag{3.27}$$

where β is the betatron function.

Measurements of the dispersion function

The standard method to determine the dispersion function at the TSR is the measurement of the closed orbit shift as a function of the ion momentum changes. As previously, changing the ion momentum is realized using the electron cooler and the fractional change of frequency $\frac{\Delta f}{f}$ is measured by Schottky noise diagnostics. Based on eq. 3.11, an alternative method for the closed orbit change is applied. In this case, by varying all magnetic fields with the ramping program the closed orbit shift is measured at the position of beam profile monitor. Both measurements are combined to determine the dispersion as shown in fig. 3.18, where the green markers are the closed orbit change dependency on $\Delta p/p$ and the blue markers represent the dependency on $\Delta B/B$, relatively. Within the small

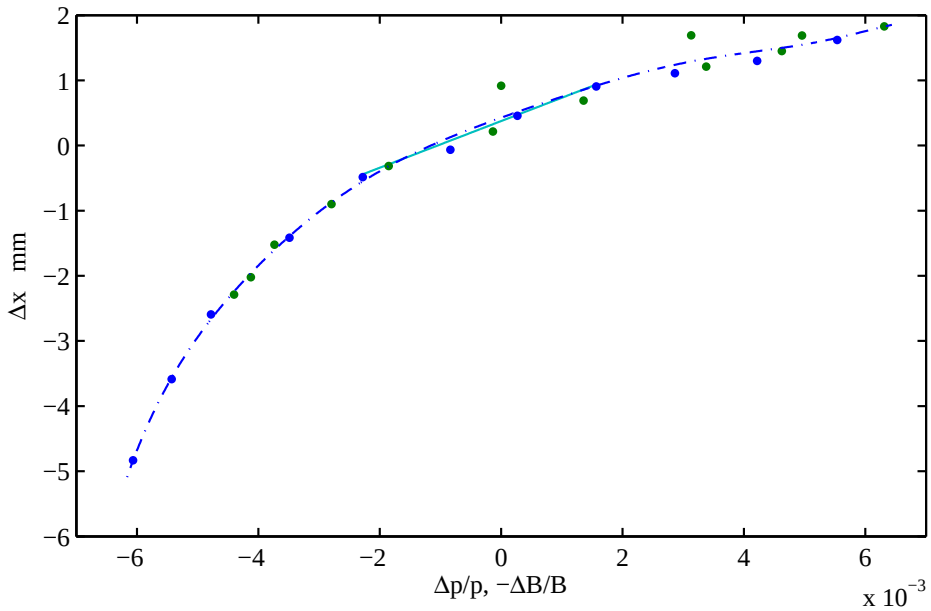

Figure 3.18: Measured closed orbit shift as a function of the variation of ion momentum and as a function of the variation of all the magnetic fields.

range centered at $\Delta p/p = 0$, the data is fitted partially, which is shown as a solid cyan line (see fig. 3.18), with the eq. 3.24, the dispersion function in the momentum range $\Delta p/p = \pm 2 \cdot 10^{-3}$, is determined:

$$D_x = 0.358\ m.$$

To verify this approximated determination of the linear dispersion, eq. 3.25 is fitted to the data which is shown as a dash-dot blue line (see fig. 3.18). From the fit the linear part of the dispersion is obtained:

$$D_x = 0.336\ m.$$

The linear dispersion value from both methods are well coincided. Due to this low dispersion at the position of the BPM and the low momentum spread of 10^{-4} of the electron cooled ion beam the effect of the dispersion on the measured beam profile can be neglected. Therefore, the emittance of the beam can be determined from the beam profile, directly.

3.5 Betatron function

The beta function is a measure of the beam width (see eq. 3.27) and provides details on how the beam size changes along an accelerator or a storage ring. Due to the strong focusing of the quadrupoles the beam size depends on the position in the ring. There are separate beta functions for the horizontal and vertical planes. The square root of β_x is proportional to the horizontal beam size. The $\beta_{x,y}$ functions of the TSR in the standard operation mode are calculated with the MAD8[21] program, and are shown in fig. 3.19. At the TSR due to its superperiodicity of 2, the β functions are repeated after a half revolution. In the straight section for the in-ring experiments, the horizontal and vertical β functions are 6 m and 2.5 m. These are double of the corresponding values in the straight section equipped with electron cooler. At the position of the electrostatic septum β_x=3.3 m and β_y=1 m. The maximum horizontal β function is β_x=17.4 m, in the horizontal focusing quadruples whereas the maximum vertical beam size is in the vertical focusing quadruples, which are situated in the straight sections of the injection and the in-ring experiments.

Measurement of the betatron function

To determine the emittance of the stored ion beam from the measured beam size, the β function at the position of the BPM has to be known. Experimentally, the β function can be measured only at the position of the 5 quadrupole families (QFX1, QFX2, QFX3, QDX1, QDX2) at the TSR. By changing the strength of the one quadrupole family the corresponding tune changes are measured via the BTF, which is shown in fig. 3.20. If the strength k of one quadrupole family is changed by Δk, the resulting horizontal and

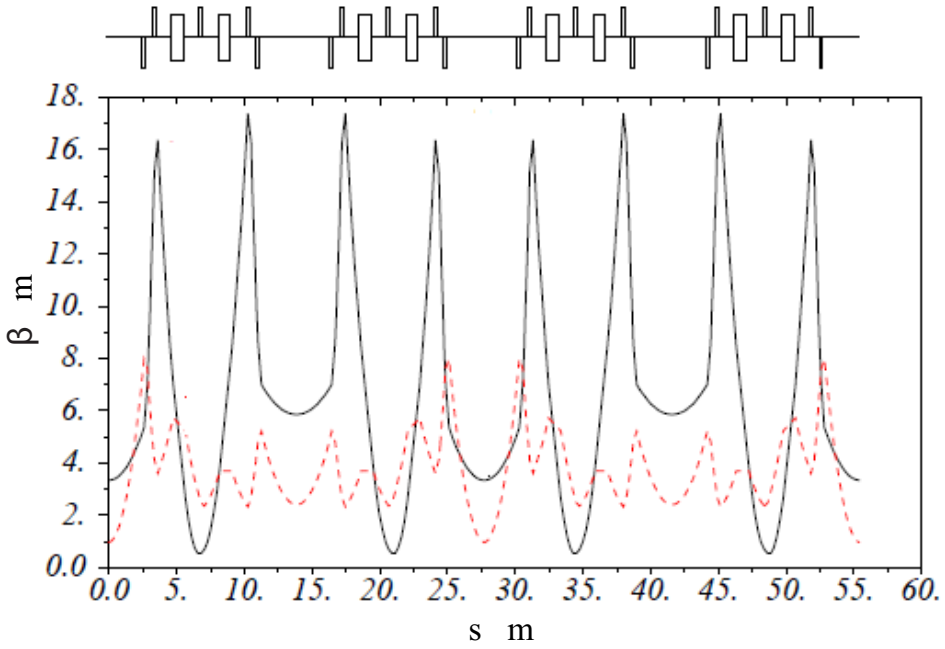

Figure 3.19: Calculated β functions with the MAD8 program. The solid black line is the horizontal, and the red dashed line is vertical, β function. The position s=0 is the center of the straight section where the RF system of the TSR is located. The smaller and larger rectangles on the top represent the location of the quadrupoles and dipoles, respectively.

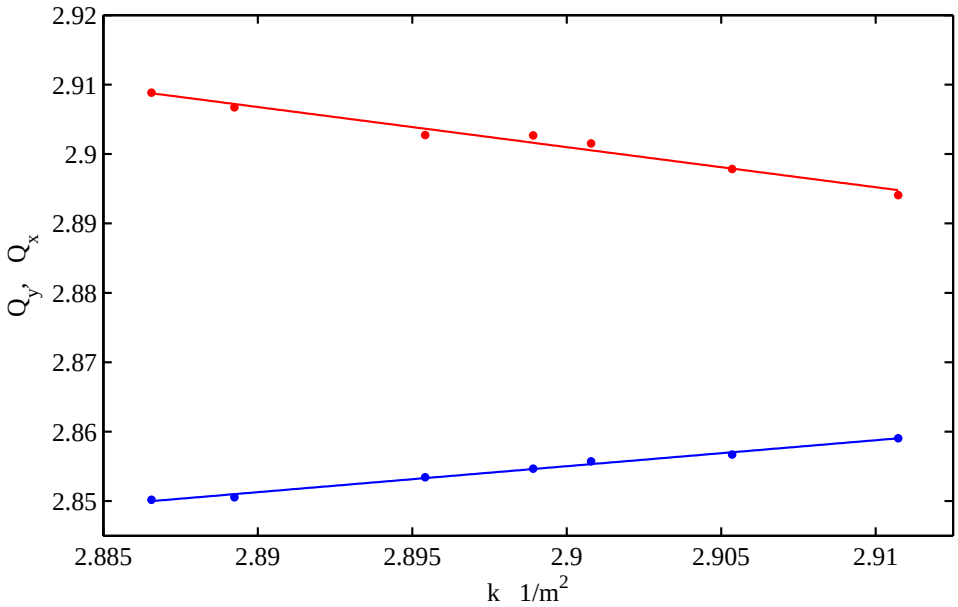

Figure 3.20: Tune measurements as a function of the quadrupole strength. The red and blue markers are the horizontal and vertical tune values, respectively.

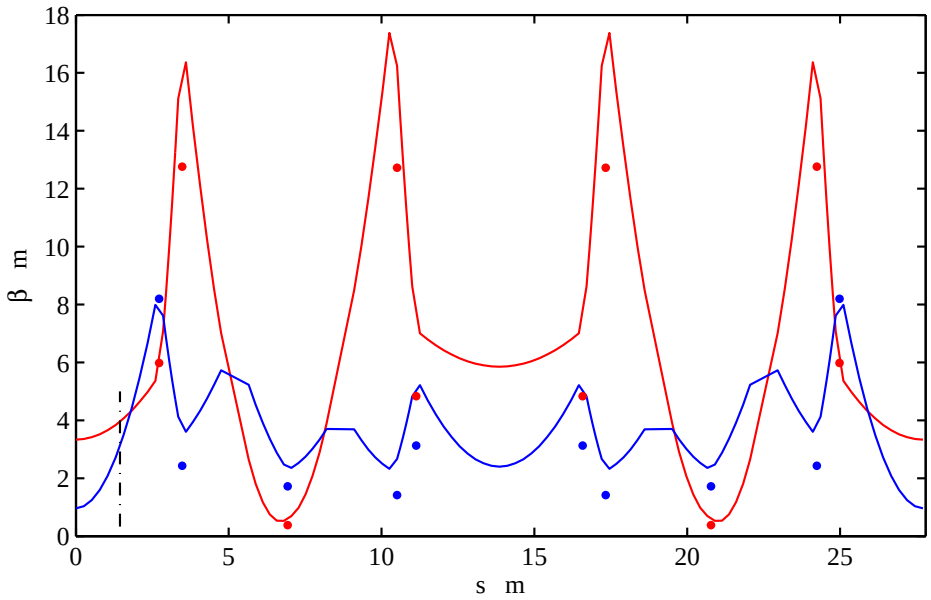

Figure 3.21: Comparison between the measured and the computed β functions. Vertical dash-dot black line represent the position of the BPM and the RF system location is at s=0. One superperiod of the ring which corresponds to the half of the TSR circumference is shown in the figure.

vertical tune change can be written as:

$$\begin{aligned} \Delta Q_x &= \frac{1}{4\pi}\int \beta_x \Delta k(s)\,\mathrm{d}s, \\ \Delta Q_y &= -\frac{1}{4\pi}\int \beta_y \Delta k(s)\,\mathrm{d}s. \end{aligned} \tag{3.28}$$

The integration has to be made over all 4 quadrupoles in a family. Therefore, the tune shift scales directly with the average β function $\langle\beta\rangle$ in each quadrupole family:

$$\begin{aligned} \Delta Q_x &= \frac{1}{\pi}\langle\beta_x\rangle L_{eff}\Delta k(s), \\ \Delta Q_y &= -\frac{1}{\pi}\langle\beta_y\rangle L_{eff}\Delta k(s), \end{aligned} \tag{3.29}$$

where L_{eff} is the effective length of one quadrupole. From the slope of the linear fits through the data, the average β function values at the location of the quadrupole families can be obtained. Fig. 3.21 shows the computed values of the horizontal and vertical β functions as red and blue as solid lines; the red and blue markers are the values of the measured β functions. The experimental data is consistent with the computed values. The deviation between them is explained as a result of the inaccuracy in the effective length of each quadrupole family. During the construction of the TSR, the effective length of each quadrupole was measured separately. However, the environment in the ring can slightly modify it. The MAD8 calculations of β functions were done for an average effective length

of $L_{eff} = 0.376$ m.

Acceptance of the TSR

Acceptance is the measure of the limiting aperture of a transport line, accelerator, or individual device; it defines how "large" a beam will fit without scraping. More technically, acceptance is the phase space volume which the beam can occupy in order to be transmitted through an optical system without losses.

The horizontal acceptance of the TSR is filled via multiturn injection of 73.3 MeV $^{12}C^{6+}$ ions. At the position of the BPM, the measured maximum horizontal beam size x_0 is shown in fig. 3.22, where the horizontal beta function β_x=4 m. If the horizontal beam size is known the horizontal acceptance of the storage ring can be calculated from the following equation:

$$A_x = \frac{x_0^2}{\beta}. \tag{3.30}$$

From the measured beam profile a maximum beam size x_0=20 mm can be determined resulting in horizontal acceptance of the storage ring $A_x = 100\ mm \cdot mrad$. Due to the low dispersion at the position of the BPM and the small momentum spread of the ion beam in determining the acceptance of the storage ring the contribution of the momentum spread to the measured beam profile is negligible.

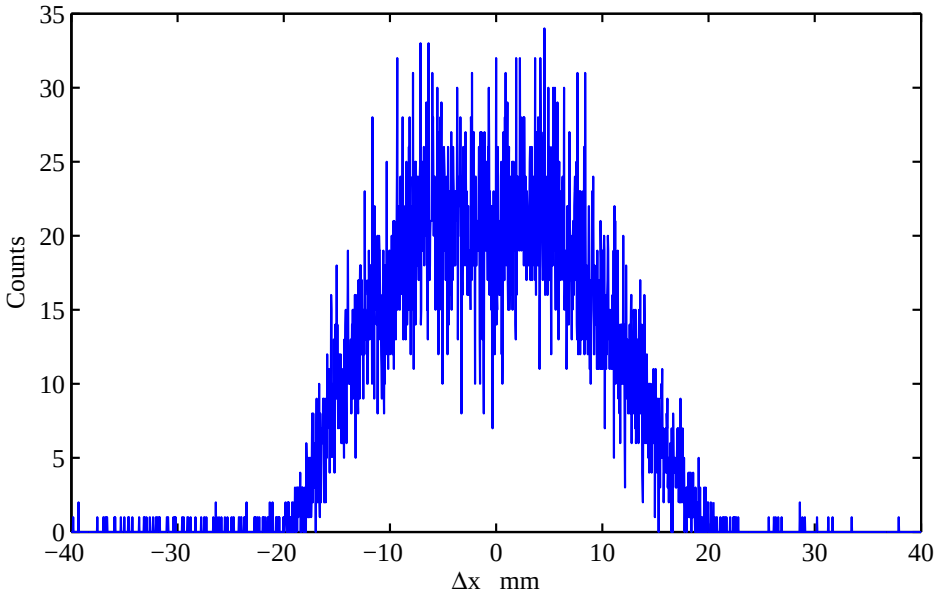

Figure 3.22: Measured horizontal beam size of the 73.3 MeV $^{12}C^{6+}$ ion beam after multiturn injection.

4 Beam losses and space-charge effects

The ion beam lifetimes due to residual gas scattering, depend on the residual gas composition, are inversely proportional to the pressure. Moreover, the lifetime of the beam in a storage ring can be limited by intrabeam scattering (IBS), transverse instabilities, incoherent space charge tune-shifts and resonances. Nonlinear magnetic field errors and large beam sizes also reduce the beam lifetime. The mechanism of IBS couples all three degrees of freedom. For heavy ions, the transverse emittance growth results from IBS, which may deteriorate the beam quality. However, it can be effectively counteracted by electron cooling and, due to the large transverse acceptance of the TSR, does not limit the lifetime.

A particle will be lost if it is scattered through an angle greater than the limiting dynamic aperture of the ring. At high densities, the space charge of the beam can change the tune, and the tune can overlap with resonances, leading to large beam losses and a poor beam lifetime. The lifetime of 73.3 MeV $^{12}C^{6+}$ ion beam is discussed for various values of the incoherent space charge tune-shifts in the current chapter. The lifetime due to electron capture of the ions in collisions with the residual gas atoms is strongly energy dependent as compared to the lifetime of single and multiple scattering processes. To investigate the energy dependency of the beam lifetime the $^{12}C^{6+}$ ion beam is injected at 73.3 MeV and decelerated to different energies. Beam losses accompanying the deceleration of the $^{12}C^{+6}$ ion beam are discussed in chapter 6.3. Except electron capture in the residual gas, a recombination with free electrons in the electron cooler through radiative or dielectronic recombination are also possible.

A moving beam containing billions of charged particles represent a current which creates its own electromagnetic field. That can influence the beam motion and can change the betatron frequencies. Part of this effect is caused by the direct Coulomb force of the charged particles in the beam. Moreover, the Coulomb field of the moving beam is accompanied by a magnetic field. Since the forces due to these two fields have opposite signs, there is a partial cancellation which leads to a $\frac{1}{\gamma^2}$ dependence of the direct space-charge force, where γ is the Lorentz factor. The beam field can be further modified by the boundary conditions imposed by the beam's surroundings. For a smooth, cylindrical and perfectly conducting vacuum chamber the boundary conditions introducing image charges or currents can be satisfied the field. Their fields then create an indirect space-charge effect, which does, therefore, not decrease with $\frac{1}{\gamma^2}$ and thus, can be dominant at high energy. If the beam as a whole does not oscillate, the space-charge forces are stationary and affect only the focusing of the individual particles leading to so-called incoherent tune shifts. In general, beam fields influence the motion of individual particles, incoherent effects, as well as perturb the beam as a whole so-called coherent effects.

4.1 Lifetime due to the residual gas interactions

The working point of the TSR is normally within the resonance-free region in the tune diagram (see fig. 3.1). Then, the lifetime of ions is primarily determined by the interac-

tions with the residual gas and the electrons in the electron cooler. The interactions are classified into the following processes:

- single and multiple Coulomb scattering,
- electron capture in the residual gas and electron cooler,
- electron stripping.

Each of these processes may become dominant under certain operational conditions of the TSR. The partial lifetime τ of the beam with respect to a certain process is given by:

$$\tau^{-1} = \sigma \rho v, \tag{4.1}$$

where σ is the relevant cross section, ρ is the density of the residual gas atoms with charge Z_{gas}, and v is the ion velocity. Since all cross sections scale with a power of Z_{gas}^n, where $1 < n < 5$, the concentration of heavier atoms in the residual gas often becomes important. The small-angle multiple scattering process and, in particular, the influence of the storage ring acceptance has been treated by Hardt[23]. Introducing a maximum acceptance angle Θ_{max} of the ring, the e^{-1} time τ_{ms} for losses due to multiple scattering is given for a round limiting aperture by:

$$\tau_{ms} = \frac{\Theta_{max}^2}{3.67 d\overline{\Theta^2}/dt}. \tag{4.2}$$

The time derivation of the projected mean square angle $\overline{\Theta^2}$ for multiple scattering is given in[24] and for a single residual gas component:

$$\tau_{ms} = \frac{\Theta_{max}^2 v^3}{\pi \rho (q/A)^2 Z_{gas}^2 r_p^2 c^4 \ln(\Theta_{max}/\Theta_{min}) 14.67}, \tag{4.3}$$

where q is the charge state of ions with mass number A, r_p is the classical proton radius and c is the speed of light, while Θ_{min} is given[24] by:

$$\Theta_{min} = \frac{2.84 \cdot 10^{-6} Z_{gas}^{1/3}}{A(v/c)\gamma}. \tag{4.4}$$

The measured lifetimes are reproduced with a value of the maximum acceptance angle of Θ_{max}=2 mrad[6]. When the emittance growth is compensated by electron cooling, the losses due to multiple Coulomb scattering can be neglected. Then, for bare ions two processes compete, namely single scattering and electron capture in residual gas.

Single scattering by an angle larger than Θ_{max} results in an effective lifetime τ_{ss}:

$$\tau_{ss} = \frac{1}{\rho v \int \sigma_R d\Omega} = \frac{\Theta_{max}^2 v^3}{4\pi \rho (q/A)^2 Z_{gas}^2 r_p^2 c^4}, \tag{4.5}$$

where Ω is a solid angle. From eq. 4.3 and eq. 4.5 it follows:

$$\tau_{ss} = \tau_{ms} \ln(\frac{\Theta_{max}}{\Theta_{min}}) 3.67 = 20.5 \tau_{ms}, \tag{4.6}$$

meaning that single scattering lifetimes are approximately one order of magnitude higher than the multiple scattering lifetimes τ_{ss}.

For the lifetime by electron capture in the residual gas, a universal scaling rule has been determined by Schlachter et al.[25]. They introduced a reduced cross section $\tilde{\sigma} = \sigma Z_{gas}^{1.8}/q^{0.5}$ and a reduced energy per nucleon $\tilde{E} = E/(Z_{gas}^{1.25}q^{0.7})$, where the projectile energy is expressed in keV/A and σ is the cross section in cm^2. They determined a relation for the reduced cross section:

$$\tilde{\sigma} = \frac{1.1 \cdot 10^{-8}}{\tilde{E}^{4.8}}(1 - e^{-0.037\tilde{E}^{2.2}})(1 - e^{-2.44\cdot 10^{-5}\tilde{E}^{2.6}}). \tag{4.7}$$

At the typical TSR energies the bracket terms can be neglected in most cases and the following equation is obtained[6]:

$$\sigma = 1.1 \cdot 10^{-8}\frac{q^{3.9}Z_{gas}^{4.2}}{E^{4.8}}. \tag{4.8}$$

For the TSR residual gas composition the strong $Z_{gas}^{4.2}$ dependence of the cross section leads to a dominant contribution to losses from the carbon, nitrogen, oxygen fraction. The lifetime τ_{rec} due to radiative recombination in the electron cooler is given by:

$$\frac{1}{\tau_{rec}} = n_e(l_{eff}/C)\alpha_{rec}, \tag{4.9}$$

where α_{rec} is the recombination coefficient, l_{eff} the effective length of the cooler, C the circumference of the storage ring and n_e the electron density. The recombination coefficient α_{rec} has been derived in [26]:

$$\alpha_{rec} = 3.02 \cdot 10^{-13}\frac{q^2}{\sqrt{kT_\perp}}(\ln(\frac{11.32q}{\sqrt{kT_\perp}}) + 0.14(\frac{kT_\perp}{Z^2})^{1/3}), \tag{4.10}$$

with $kT_\perp$ in eV and α_{rec} in cm^3/s.

For stripping of one-electron ions, reliable theoretical as well as experimental results exist. Theoretical treatments of stripping reactions are often based on classical models[27] or on the Born approximation more sophisticated calculations do exist. The classical model considers the energy transfer to the bound electron as a result of its scattering by an atomic nuclei of the residual gas with charge Z_{gas} and by the individual electrons of such an atom. The stripping cross sections [27],[28] for ion velocities larger than the velocity of the ionic electron ($v > Zv_0$, with the Bohr velocity as a $1s$ electron in atomic hydrogen with $v_0 = \alpha \cdot c$, where α is fine structure constant) are calculated separately for light and heavy targets, which translates into heavy and light projectiles.

For heavy projectiles with $Z \geq Z_{gas}$ the following equation is obtained:

$$\sigma_{sh} = 4\pi a_0^2(\frac{v_0}{v})^2(Z_{gas}^2 + Z_{gas})\frac{I_0}{I}, \tag{4.11}$$

where a_0 is the radius of the first Bohr orbit, I is the binding energy of the electron and I_0=13.6 eV.

For light projectiles with $Z \leq Z_{gas}^{1/3}$:

$$\sigma_{sl} = \pi a_0^2 Z_{gas}^{2/3} \frac{v_0}{v} \sqrt{\frac{I_0}{I}}. \tag{4.12}$$

In this case, it is taken into account that firmly bound inner electrons of the target no longer act independently but screen the nuclear field. The stripping cross section for ions with several electrons can be calculated approximately by summing over the contributions of the k individual electrons of the projectile.

For heavy projectiles:

$$\sigma_{sh}(k) = 4\pi a_0^2 (\frac{v_0}{v})^2 (Z_{gas}^2 + Z_{gas}) \sum_{i=1}^{k} \frac{I_0}{I_i}. \tag{4.13}$$

For light projectiles:

$$\sigma_{sl}(k) = \pi a_0^2 Z_{gas}^{2/3} \frac{v_0}{v} \sum_{i=1}^{k} \sqrt{\frac{I_0}{I_i}}. \tag{4.14}$$

Lifetime measurements

After bakeout of the storage ring to 250° the residual gas composition is typically 93 % hydrogen, 2 % carbon, 1 % nitrogen 6 % oxygen and, as the heaviest component, 0.3% argon. Table 4.1 contains a compilation of the measured lifetimes of stored ion beams with and without electron cooling, in parallel to theoretical lifetime estimation of the respective dominating process: Coulomb scattering (MS), stripping reactions (ST), electron capture in the residual gas (CAP) and in the electron cooler (REC). The lifetimes of molecules are determined by dissociation processes(DIS) in the residual gas and in the electron cooler, yet they are not in the focus of this thesis. The lifetime for single charged ions is determined by stripping reaction and can be calculated using eq. 4.13 and 4.14.

Thus, taking into account the uncertainties in the residual gas pressure, it is possible to understand the measured lifetimes reasonably well on the basis of the calculated partial lifetimes. The longest lifetime of about 60 hours was achieved for protons at 21 MeV. This lifetime was determined by electron capture in the electron cooler. The lifetimes for highly charged ions are limited by electron capture processes in the residual gas and in the electron cooler. The heaviest ion stored so far was $^{197}Au^{50+}$. With $^{197}Au^{50+}$ ions a storage lifetime of only 3 s was observed with the magnetically expanded electron beam in the cooler at an electron density of $n_e \approx 10^7$ cm^{-3}. This short storage time is a consequence of the highest recombination rate coefficient in the electron cooler ever observed with an atomic ion. At about 30 meV a huge dielectric recombination resonance was found [22].

For the lifetime of the $^{12}C^{6+}$ ion beam without electron cooling two main loss mechanisms are considered, namely as multiple scattering and electron capture in the residual gas. Fig. 4.1 shows the measured lifetime of the $^{12}C^{6+}$ ion beam at energies between 9.77 and 73.3 MeV, without electron cooling. The lifetime measurements fluctuated significantly, because of short measuring times due to limited available beamtime. The

Table 4.1: Beam lifetimes in the TSR

			Experiment		Theory			
Ion	Energy [MeV]	Pressure [10^{-11} mbar]	Cooled [s]	Uncooled [s]	Cooled [s]	Expl.	Uncooled [s]	Expl.
p	21	4	220000		180000	REC		
HD^{+}	2	7		5				DIS
$^{7}Li^{+}$	13	6		48	41	ST	41	ST
$^{9}Be^{+}$	7	6	16	16	12	ST	12	ST
$^{12}C^{6+}$	9	7	128	92	122	CAP	101	CAP
$^{12}C^{6+}$	73	7	995	1940	1041	REC	6313	MS
$^{12}C^{6+}$	73	6	7470		5519	REC	5630	MS
$^{28}Si^{14+}$	115	6	540	260	424	CAP	493	CAP
$^{32}S^{16+}$	196	5	450		554	REC	1200	CAP
$^{35}Cl^{15+}$	157	6	366		306	CAP	375	CAP
$^{35}Cl^{17+}$	202	6	318	366	402	REC	735	CAP
$^{56}Fe^{22+}$	250	5	77		90	REC	278	CAP
$^{58}Ni^{25+}$	342	5	60		89	REC	374	CAP
$^{63}Cu^{26+}$	510	6	122		166	REC	622	CAP
$^{74}Ge^{28+}$	365	5	45		59	REC	162	CAP
$^{80}Se^{25+}$	480	5	204		179	REC	384	CAP
$^{197}Au^{50+}$	710	5	3					

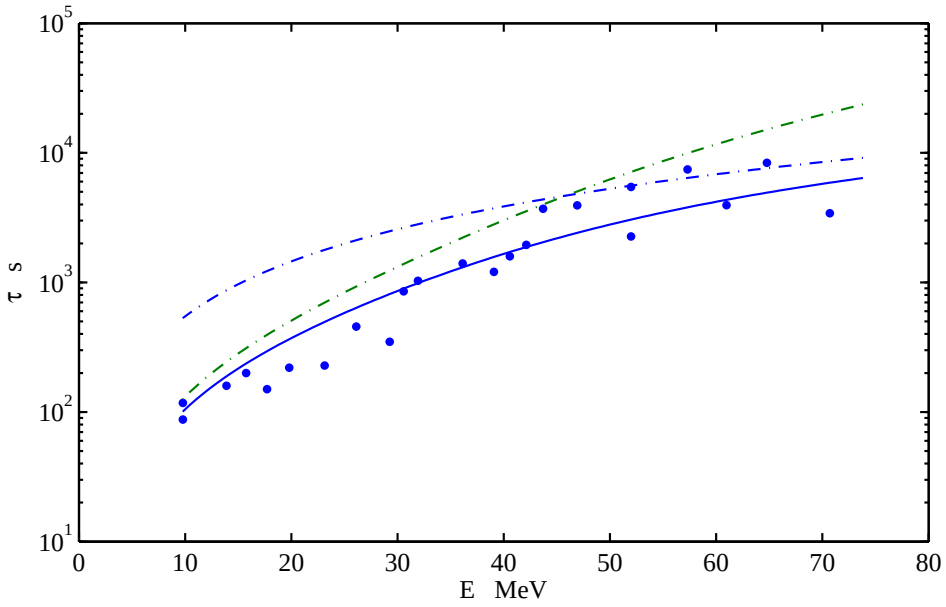

Figure 4.1: Energy dependency of the lifetimes measured with the $^{12}C^{6+}$ ion beam.

dash-dot blue curve is the lifetime τ_{ms} due to multiple scattering calculated with eq. 4.3, whereas the dash-dot green curve represents the electron capture lifetimes τ_{ec} calculated with eq. 4.7. Both curves are calculated for the residual gas pressure of p=$7 \cdot 10^{-11}$ mbar the corresponding a gas density of $1.67 \cdot 10^{12} 1/\mathrm{m}^3$. Multiple scattering dominates at higher energies around 73.3 MeV, whereas at low-energies down to 9.77 MeV electron capture determines of the lifetime. The total lifetime of these two processes is displayed with a solid blue line and are determined by the following equation:

$$\frac{1}{\tau_{total}} = \frac{1}{\tau_{ms}} + \frac{1}{\tau_{ec}}. \tag{4.15}$$

At the energies of 73.3 MeV and 9.77 MeV, the $^{12}C^{6+}$ ion beam lifetimes are also measured with electron cooling. For the lifetime of the 9.77 MeV ion beam, the electron current at the electron cooler is 0.0123 A and the electron density is $9.249 \cdot 10^{12} 1/m^3$. The expansion of the electron beam α=B_{Gun}/B_{cooler} is 9.3, which determines the ratio of transverse electron temperatures of the electron gun and in the electron cooler. In fig. 4.2 the result of the intensity decay at 9.77 MeV with $constant \cdot e^{-t/\tau}$ for an electron cooled and uncooled $^{12}C^{6+}$ ion beam is shown. The measured lifetime for the electron cooled and uncooled ion beams at 9.77 MeV are 128 s and 92 s, respectively, both are consistent with the theoretical values. Therefore, with electron cooling, it is impossible to significantly improve the lifetime at this energy, because it is mainly determined by the electron capture in the residual gas.

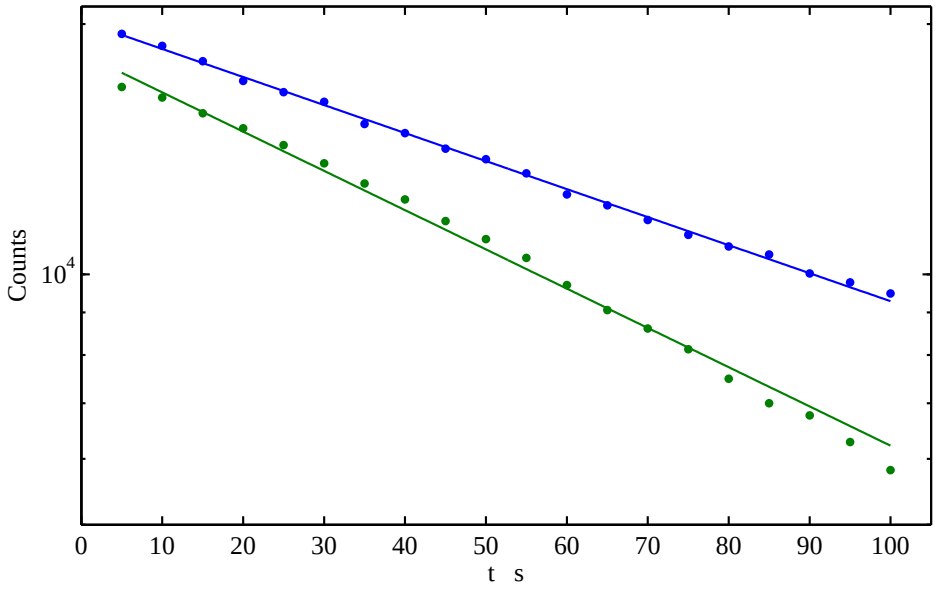

Figure 4.2: Lifetimes of the $^{12}C^{6+}$ ion beam measured at 9.77 MeV with and without electron cooling are shown as blue markers and green markers respectively.

4.2 Accumulation and intensity limit in the TSR

To study beam lifetime at higher intensities, electron cooling stacking is applied during multiturn injection of the beam.

Multiturn injection, often employed for heavy ions, is a technique of injecting the ions into a circular machine where the time is longer than the circulation period of the beam. This method is accomplished by moving the equilibrium orbit at the injection point so that previously injected particles neither collide with the newly injected beam nor with the injection septum. Applying this scheme multiple times, the horizontal acceptance of the TSR can be completely filled typically within 70 turns. The revolution period of the $^{12}C^{6+}$ ion beam is approximately 2 μs and therefore, multiturn injection only takes place in about 150 μs. The transverse phase space is filled from the center outwards

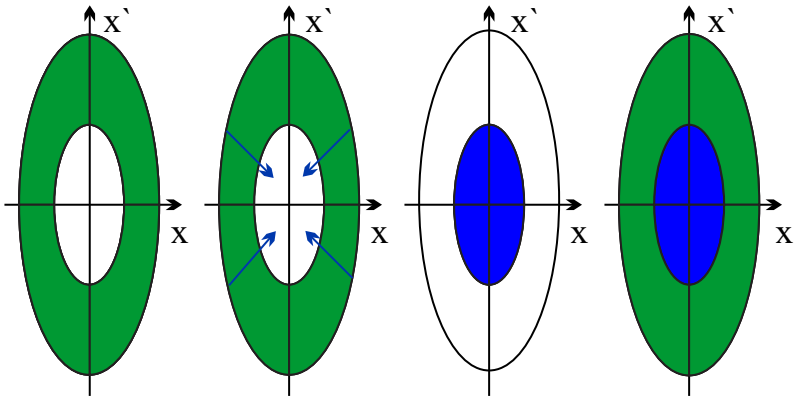

Figure 4.3: Multiturn injection of the beam with electron cooling stacking. The first step is multiturn injection to fill the horizontal acceptance of the TSR. Then, by applying electron cooling, the beam is concentrated in the center of the transverse phase space to empty the previously occupied volume for further multiturn injections. The free space will be filled with new incoming particles. The final scheme is the populated transverse phase space ellipse.

and the resultant intensity increases about a factor 40, depending on the beam quality from the injector. Then, electron cooling is applied to the stored beam, to compress its phase space for further incoming particles, often called electron cooling stacking. Fig. 4.3 shows a schematic representation of the multiturn injection process and electron cooling stacking in the horizontal phase space. The multiturn injected particles have a much lower density and larger momentum spread than the compressed beam core, and are indicated by the green color (see fig. 4.3). To avoid a collision between the electron cooled ion beam (marked in blue) and the septum's foil, the defection angle of the bumper magnets must be reduced as compared to the normal multiturn injection. Then injection and stacking is repeated several times, and thus, a large intensity multiplication factor can be obtained[32]. The intensity multiplication factor is defined as the ratio of the accumulated stored ion beam to the injected ion beam current. With electron cooling stacking the stored intensity I increase with the time as:

$$\frac{dI}{dt} = n_r \cdot I_m - \frac{I}{\tau}, \tag{4.16}$$

where n_r is the injection repetition rate, I_m the effectively stored ion current during one multiturn injection, and τ is the beam lifetime. The solution of the differential eq. 4.16 is:

$$I = I_0(1 - e^{-t/\tau}) \tag{4.17}$$

with:

$$I_0 = n_r \cdot I_m \tau \tag{4.18}$$

The current I_m depends on the injector current I_e with: $I_m = M \cdot I_e$, where M is the intensity multiplication factor for multiturn injection. The total intensity multiplication factor $N = I_0/I_e$ is thus given by:

$$N = n_r \cdot M\tau \tag{4.19}$$

To calculate the intensity multiplication factor N of electron cooling stacking, the lifetime of the ion beam must be known. The repetition rate n_r for multiturn injection depends on the time T_C for electron cooling to compress the phase space with $n_r = 1/T_C$. The intensity multiplication factor M depends on the phase space availability for further multiturn injection, because the phase space is more and more occupied by the stored ion beam.

The accumulation of the $^{12}C^{6+}$ ion beam, applying a combination of multiturn injection and electron cooling stacking, is shown in fig. 4.4. Injection starts at t=24.5 s, shows a nearly linear increase at the beginning up to an intensity of about 600 μA. The solid black line is a fit to this region of intensity increase and $n_r \cdot I_m$=17.426 μA/s is obtained from its slope. Here, it is assumed that the injection current from the source is constant, but usually fluctuations are observed during injection. The dash-dot blue line is a calculated function using eq. 4.17, with $\tau = 995.04\ s$. The reason, for the significant deviation from calculated intensity of the measured, can be a lifetime decrease and fall-off of the effective injected intensity during the accumulation process. To investigate the lifetime dependency on the beam intensity, lifetime measurements are performed for an electron-cooled ion beam at different intensities. The final flat region of the intensity is fitted with a constant, which is shown as dash-dot red line on the top. It resembles the maximum current of 1202 μA that can be achieved by electron-cooling stacking during accumulation. However, in the present case this current was not stable. At t=282 s, there is a sudden fall-off, which represents the rapid beam loss.

Lifetime of the $^{12}C^{6+}$ ion beam at intensities higher than 100 μA has been measured with a DC transformer and the BPM at lower currents. All measurements are fitted with eq. 4.17 to estimate the lifetime. As shown in fig. 4.5, the measured lifetimes are $\tau = 1100 \pm 100$ seconds in the intensity rage of 10μA to 1 mA, all lines are parallel. Therefore, the lifetime of the $^{12}C^{6+}$ ion beam is assumed to be constant in these intensity ranges, which means the lifetime of the ion beam can not be reason for deviation of the measured beam intensity (see fig. 4.4). The possibly reason for the current deviation during accumulation and for the intensity fall-off limiting the current accumulation can be explained by the incoherent tune shift.

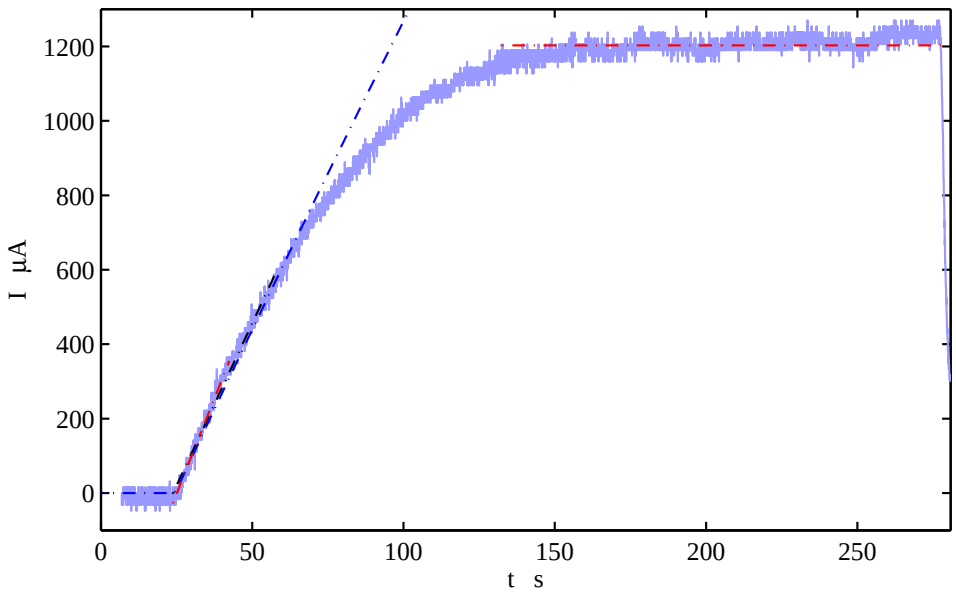

Figure 4.4: Accumulation of the $^{12}C^{6+}$ ion beam applying a combination of multiturn injection and electron cooling stacking.

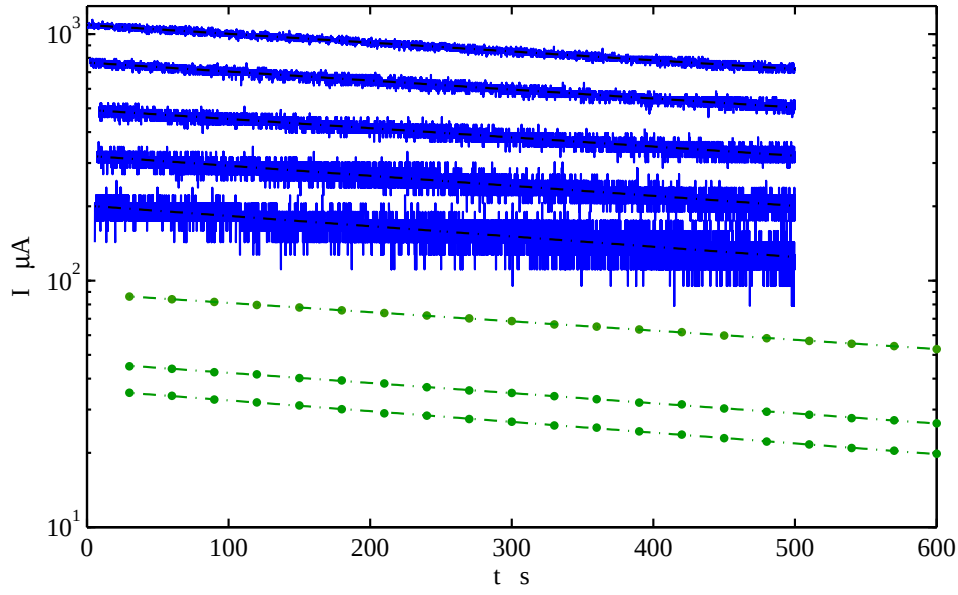

Figure 4.5: Lifetimes of the $^{12}C^{6+}$ ion beam for different intensities. Blue lines are the lifetimes obtained with the DC transformer. Each data set is fitted with eq. 4.17, as shown by the black dash-dot lines. Green markers are lifetime measurement data that are recorded with the BPM, which are also fitted and shown as green dash-dot lines.

4.3 Incoherent tune shift

The maximum ion current that can be stored at the TSR depends on the incoherent tune shift. Due to the defocusing force that is caused by the space charge of the beam, the tune of the oscillating particles are changed. This change may not exceed a certain value in order to avoid resonances and thus, beam losses. The incoherent tune shift is a beam field effect which influences the transverse particle motion and changes the betatron frequencies. Here, the space charge of the beam creates the defocusing forces which change the tune. The maximum number N_i of ions that can be stored is determined by the incoherent tune shift ΔQ given by (see appendix B):

$$N_i = \frac{A}{q^2}\frac{2\pi}{r_p} B\beta^2\gamma^3\epsilon(-\Delta Q), \tag{4.20}$$

where A is the mass number of the ions, q the charge state, r_p the classical proton radius, B the bunching factor, β ion velocity in units of the speed of light, γ the relativistic mass increase and ϵ the beam emittance. The maximum incoherent tune shift acceptable for a coasting beam (B=1) is $\Delta Q \approx -0.1$ for the TSR. From eq. 4.20 a scaling law for the resultant maximum intensity can be derived as:

$$I = q \cdot e_0 \cdot N_i \cdot f_0, \tag{4.21}$$

where f_0 is the revolution frequency. Because the emittance scales as [33]:

$$\epsilon \propto \left(\frac{q^4}{A^2}\frac{N}{\lambda_{cool}}\frac{1}{\beta^3}\right)^{0.44}, \tag{4.22}$$

where the cooling rate λ_{cool} is proportional to the density n_e of the electron beam:

$$\lambda_{cool} \propto n_e \frac{q^2}{A}. \tag{4.23}$$

The electron beam density scales as $n_e \propto \beta^2$. If expressions 4.22 and 4.23 are inserted into eq. 4.20 to estimate the maximum stored ion intensity due to the incoherent tune shift the following scaling law is obtained:

$$I_{max} = constant \cdot \frac{(A^{19}E^9)^{1/28}}{q}, \tag{4.24}$$

where the *constant* can be calculated from the current measurements with the $^{12}C^{6+}$ ion beam. The maximum values of the accumulated intensities with electron-cooling stacking and calculated values using eq. 4.24 are listed in table 4.2. The stability limit I_{max} can be only reached up to ion masses of $A = 35$, because of the intensity limitations posed by the tandem and post- accelerator combination for ion masses higher than $A = 35$. Except for the $^{12}C^{6+}$ ion beam, the maximum accumulated intensities in this table are summarized from previous beamtimes at the TSR. The calculation of the maximum stable $I_{the.}$ intensity for the $^{12}C^{6+}$ ion beam is shown in fig. 4.6. The calculated incoherent space-charge tune shifts for the $^{12}C^{6+}$ ion beam as a function of beam velocity are shown in the tune diagram in fig. 4.7. In these calculations, according to eq. 4.20 equilibrium beam

Table 4.2: Experimentally accumulated intensities and calculated maximum intensity values due to the incoherent tune shift

Ion	Energy [MeV]	$I_{exp.}$ [μA]	$I_{the.}$[μA]
p	21	1000	740
$^{16}O^{8+}$	98	750	1000
$^{12}C^{6+}$	73	1000	1000
$^{32}S^{16+}$	195	1500	999
$^{35}Cl^{17+}$	293	1000	1130
$^{45}Sc^{18+}$	178	380	1087
$^{56}Fe^{22+}$	250	70	1151
$^{56}Fe^{23+}$	260	128	1114
$^{58}Ni^{25+}$	342	600	1147
$^{63}Cu^{25+}$	290	280	1150
$^{63}Cu^{26+}$	510	100	1326
$^{74}Ge^{28+}$	365	110	1234
$^{80}Se^{25+}$	480	100	1590
$^{80}Se^{31+}$	506	1	1304
$^{197}Au^{50+}$	695	3	1651

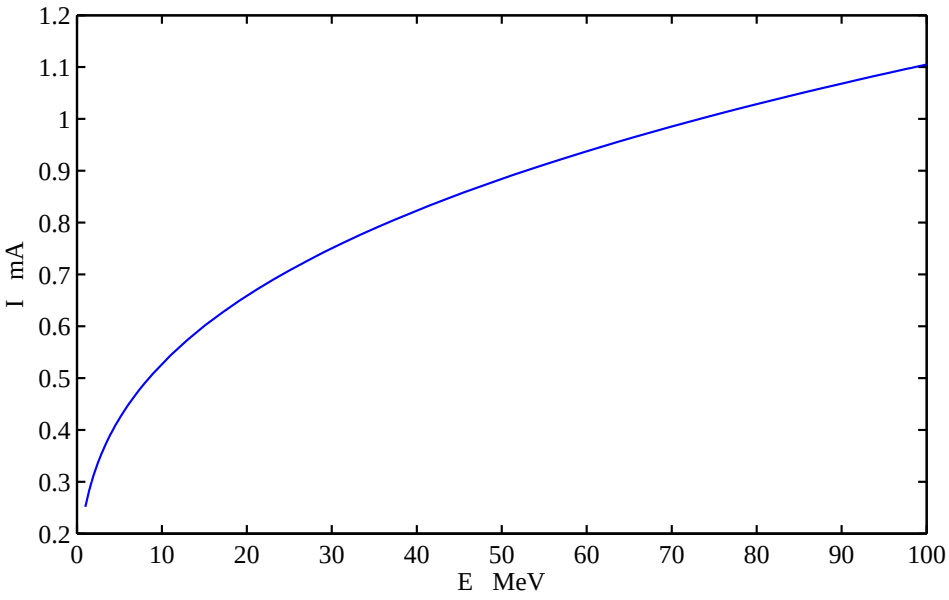

Figure 4.6: Calculation of the maximum stable intensity as a function of energy for the $^{12}C^{6+}$ ion beam according to eq. 4.24.

emittance[1] has to be known, therefore it is determined from the equilibrium beam width[2] which is measured in IBS experiments. Tune-shift calculations based on the current accumulation (see fig. 4.4) yielded deviations from the linear dependency at around 600 μA and a sudden beam loss at 1.2 mA. Here, the normal working point shown as a blue marker (indicated in fig. 3.1), was set to Q_x=2.892 and Q_y=2.856. During accumulation of the $^{12}C^{6+}$ ion beam, incoherent tune shift causes particles to interact with 4^{th} order resonances, which are shown as green solid lines in the TSR tune diagram. Exceeding 600 μA, the ion beam will have a ΔQ=-0.102 and the working point will be shifted to Q_x=2.79 and Q_y=2.754, which is shown as a yellow marker in tune diagram. The working point where the intensity drops is shown as a red marker at an incoherent tune shift of ΔQ=-0.14.

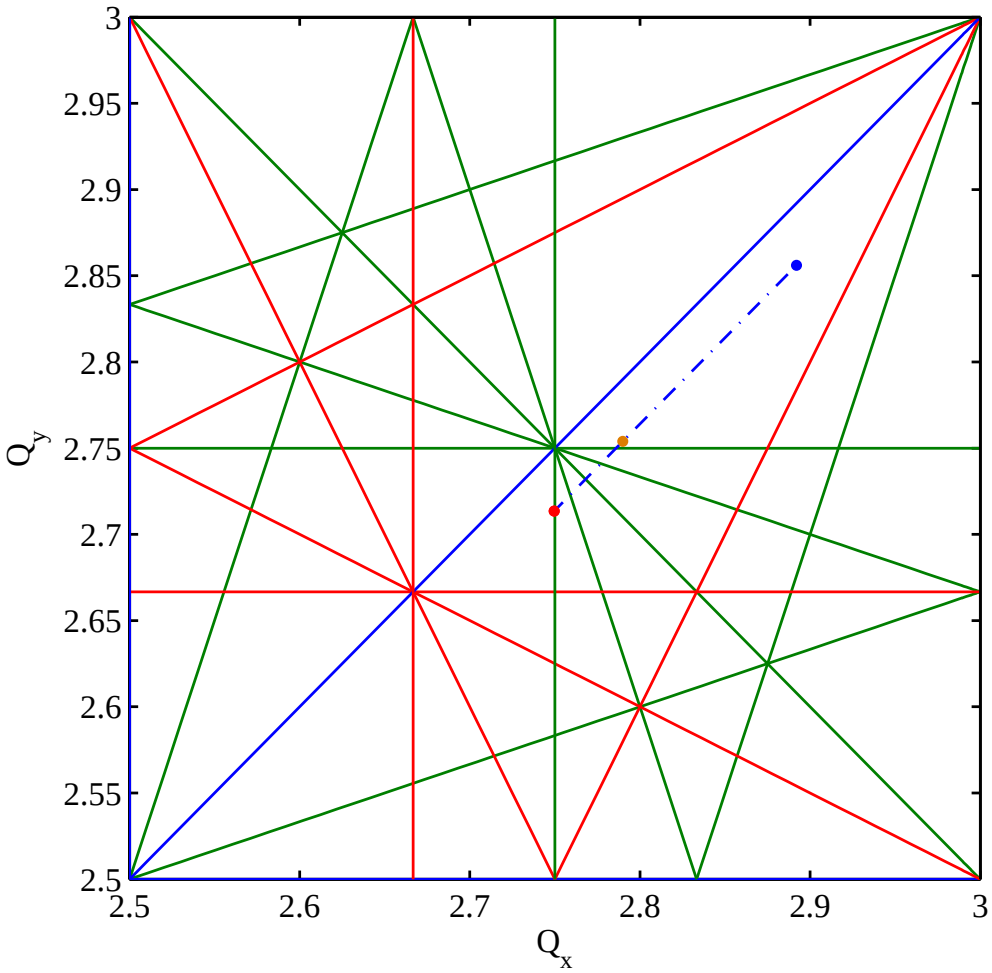

Figure 4.7: Incoherent tune shift of the $^{12}C^{6+}$ ion beam.

[1]See next chapter, section 5.3
[2]See equation 3.27

5 Intrabeam scattering

IBS is a multiple scattering effect within bunched or coasting beams due to Coulomb interaction of charged particles. It leads a diffusion in all three dimensions, expands the whole beam and if the aperture is filled, reduces the lifetime. In dense and/or low-energy beams, IBS is one of the dominant effects impacting the beam evolution. Coulomb interaction of charged particles in a stored beam causes an exchange of energies between the transverse and longitudinal oscillations. If the corresponding scattering angles are large, particles can be lost. Therefore, under typical operational conditions, IBS is always counterbalanced by electron beam cooling. During deceleration of ions in the TSR, the ramp cycle does not allow for electron cooling and at the final energy, the influence of IBS on the circulating ion beam has been investigated. Within this thesis, after introducing into IBS theory, results from IBS with the $^{12}C^{6+}$ ion beam in the energy range between 73.3 MeV and 9.77 MeV are presented in this chapter.

5.1 IBS theory

In an earlier work by Piwinski[30] the IBS theory was developed for weak-focusing machines where the lattice functions are constant. Later, the theory was extended by Martini[31] for strong focusing conditions taking into account the variation of the lattice functions along the storage ring. Based on both[30, 31], the growth times which determine the bunch dimensions, defined by:

$$\begin{aligned} \tau_{x,y}^{-1} &= \frac{1}{\sigma_{x,y}} \frac{d\sigma_{x,y}}{dt} \\ \tau_{p}^{-1} &= \frac{1}{\sigma_{p}} \frac{d\sigma_{p}}{dt} \end{aligned} \tag{5.1}$$

of the assumed gaussian transverse beam width $\sigma_{x,y}$ and relative momentum spread σ_p can be written as:

$$\begin{aligned} \frac{1}{\tau_p} &= \langle A_0 \frac{\sigma_h^2}{\sigma_p^2} f(a,b,c) \rangle \\ \frac{1}{\tau_x} &= \langle A_0 [f(\frac{1}{a}, \frac{b}{a}, \frac{c}{a}) + D_x^2 \frac{\sigma_h^2}{\sigma_{x\beta}^2} f(a,b,c)] \rangle \\ \frac{1}{\tau_y} &= \langle A_0 [f(\frac{1}{b}, \frac{a}{b}, \frac{c}{b})] + D_y^2 \frac{\sigma_h^2}{\sigma_{y\beta}^2} f(a,b,c)] \rangle \end{aligned} \tag{5.2}$$

where

$$A_0 = \frac{q^4 r_0^2 c N}{A^2 64\pi^2 \beta^3 \gamma^4 \epsilon_x \epsilon_y \sigma_s \sigma_p}$$
$$\frac{1}{\sigma_h^2} = \frac{1}{\sigma_p^2} + \frac{D_x^2}{\sigma_{x\beta}^2} + \frac{D_y^2}{\sigma_{y\beta}^2}$$
$$a = \frac{\sigma_h \beta_x}{\gamma \sigma_x \beta}$$
$$b = \frac{\sigma_h \beta_y}{\gamma \sigma_y \beta}$$
$$c = \sigma_h \beta \sqrt{\frac{2d}{r_0}}$$

$\epsilon_{x,y}$ is the horizontal and vertical emittance, d is the minimum of the horizontal and vertical beam radii, $D_{x,y}$ is the horizontal and vertical dispersion, σ_s is the rms bunch length, σ_p is the relative momentum spread, $\sigma_{x\beta}$, $\sigma_{y\beta}$ are horizontal and vertical betatron width, r_0 is the classical proton radius, and N is the number of particles. The function f is given by:

$$f(a,b,c) = 8\pi \int_0^1 [2ln(\frac{c}{2}(\frac{1}{P} + \frac{1}{Q})) - 0.577...] \frac{1-3u^2}{PQ}\, \mathrm{d}u, \tag{5.3}$$

where

$$\begin{aligned} P^2 &= a^2 + (1-a^2)u^2 \\ Q^2 &= b^2 + (1-b^2)u^2. \end{aligned} \tag{5.4}$$

The derivatives of betatron and dispersion functions of the lattice $\beta'_{x,y}$ and $D'_{x,y}$ are neglected, due to their weak influences on rise time. From eq. 5.2 for coasting and bunched beams, an expansion of the beam due to IBS can be expressed in terms of three coupled differential equations:

$$\begin{aligned} \frac{1}{\sigma_i}\frac{d\sigma_i}{dt} &= c_i \cdot \frac{q^4}{A^2}\frac{N}{\beta^3}\frac{1}{\epsilon_x \epsilon_y \Delta p/p \cdot C} \qquad \textit{coasting beam}, \\ \frac{1}{\sigma_i}\frac{d\sigma_i}{dt} &= c_i \cdot \frac{q^4}{A^2}\frac{N}{\beta^3}\frac{1}{\epsilon_x \epsilon_y \Delta p/p \cdot h \cdot l_{eff}} \qquad \textit{bunched beam}, \end{aligned} \tag{5.5}$$

where c_i (i=x,y,p)[1] are lattice dependent constants, which weakly depend on the beam energy, N is the number of ions with charge state q, mass A and velocity β and C is the circumference of the storage ring. If the beam is bunched, in the denominator C the circumference of the storage ring must be replaced by $h \cdot l_{eff}$, where h is the number of bunches and l_{eff} is the effective bunch length.

Simplified IBS model for coasting and bunched beams

The IBS equations are rather complex. It is assumed that in the IBS process the beam characteristics such as the horizontal and vertical emittances, the square of the momen-

[1] Transverse and longitudinal components.

tum spread and the square of the bunch length are proportional to each other, so that: $\epsilon_x \cdot \epsilon_y \cdot \frac{\Delta p}{p} \propto \sigma_i^5$ for a coasting beam and $\epsilon_x \cdot \epsilon_y \cdot \frac{\Delta p}{p} \cdot l_{eff} \propto \sigma_i^6$ for bunched beams. These assumptions will simplify the system of differential equations 5.5 into the following expression for all three degrees of freedom:

$$\frac{1}{\sigma_i}\frac{d\sigma_i}{dt} = \frac{D_i}{\sigma_i^\gamma}, \tag{5.6}$$

where γ=5 for coasting beam and γ=6 for bunched ion beam. The heating term D_i:

$$D_i \propto c_i \frac{q^4}{A^2}\frac{1}{\beta^3}N, \tag{5.7}$$

leads to a growth of beam width and the emittance. The solution of equation 5.6 is given by:

$$\sigma_i(t) = (\gamma \cdot D_i \cdot t + \sigma_o^\gamma)^{\frac{1}{\gamma}}, \tag{5.8}$$

where σ_0 is the initial beam width at equilibrium between IBS and beam cooling. Equation 5.8 is valid only to explain IBS effects starting from the equilibrium state. If the ion beam is bunched, IBS rates are expected to be higher at the same intensities as coasting beam due to higher ion densities.

5.2 Transverse IBS measurements

Experiments are conducted with 73.3 MeV coasting and bunched $^{12}C^{6+}$ ion beams to test the validity of the eq. 5.8. Electron cooling is applied of the beam to achieve an equilibrium state between IBS and beam cooling. The BPM starts recording data for the equilibrium state of the beam one second before switching off the electron cooler and continues to measure the time development of the beam profile without cooling. The electron cooler must be switched off to investigate the effects of IBS. At the same intensity, experiments are conducted with total measuring times of 2 and 10 seconds, where each data acquisition consists of 20 snapshots. For the data using duration of two seconds the beam profile development is recorded every 0.1 s, and for the ten second runs every 0.5 s. Both data are combined and analyzed jointly. Since the lifetime of the beam is in order of hours a new injection is not required. Therefore, it is possible to continue the experiments with the same ion beam. To achieve better statistics the measurements are repeated and corrected to the resolution of the BPM (see appendix C). The horizontal beam width of coasting and bunched beams with a bunching voltage of 195.44 V are shown in fig. 5.1 as a function of time at 50 μA ion current. The dash-dot line through the data is a fit using eq. 5.8, where the initial beam size σ_0, the heating term D_i and γ are the fitting parameters. It is obvious that the IBS rate of the bunched ion beam is larger due to higher densities as compared to a coasting ion beam. Measurements in the 5 μA to 100 μA intensity range to determine the $\overline{\gamma}$ parameter of IBS for coasting and bunched ion beam with bunching voltage of 195.44 V are shown in fig. 5.2. From the fits $\overline{\gamma} = 4.68$ and $\overline{\gamma} = 5.9$ are determined for the coasting and bunched beam accordingly, which resembles $\gamma = 5$ and $\gamma = 6$ as predicted in simplified IBS approximation. Heating terms D_x of IBS as a function of intensity are

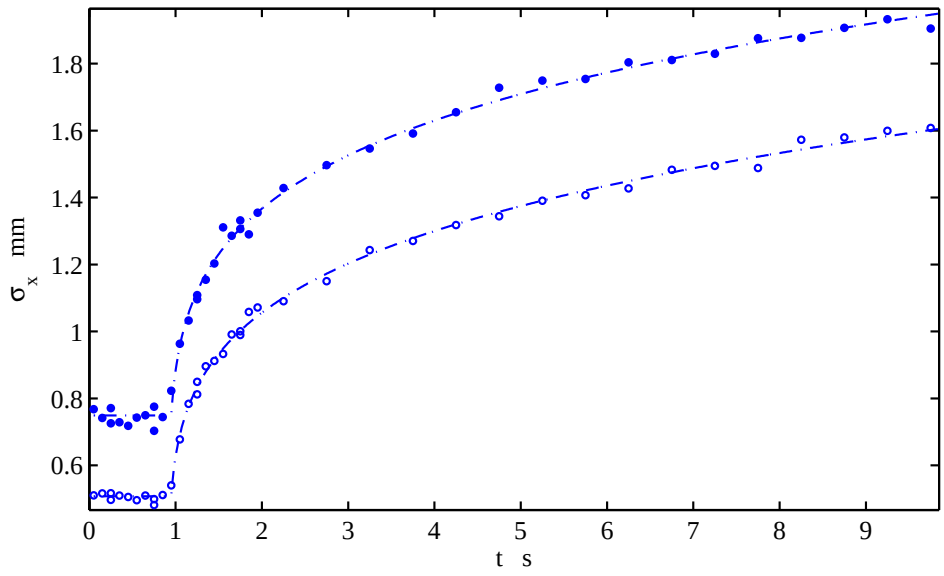

Figure 5.1: Expansion of the beam width due to IBS is measured with the 73.3 MeV coasting and bunched $^{12}C^{6+}$ ion beams at 50 μA ion current. The horizontal beam width of Gaussian profiles are shown as a function of time. The hollow markers are the data with the coasting beam and the solid markers are those with the bunched beam.

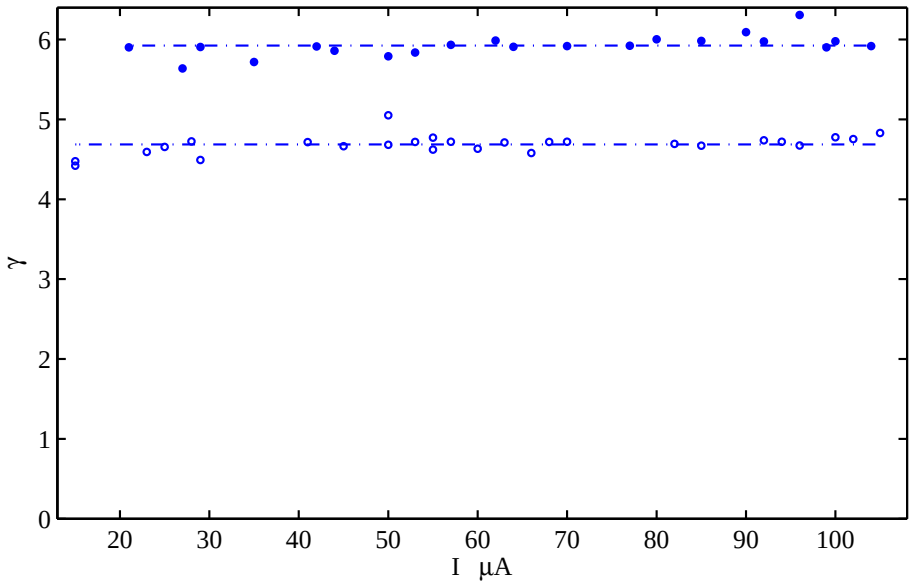

Figure 5.2: Determination of the γ parameter of IBS with 73.3 MeV coasting and bunched $^{12}C^{6+}$ ion beams as a function of the beam intensity. The hollow markers are the data with the coasting beam and the solid markers are those for the bunched beams.

shown in fig. 5.3 for coasting and various bunched ion beams. IBS heating effects increase linearly with the beam intensity, enhancing the betatron oscillation amplitude. The $\overline{\gamma}$ parameters for bunched beams, at different resonator voltages are also determined. The resonator voltage values are controlled by a function generator and therefore calibration measurements are obtained (see appendix D).

The average value of γ is kept constant for the analyses of the heating term as a function of intensity. Fig. 5.4 shows all average values of the γ parameter for IBS at different resonator voltages for intensities from 15 μA to 100 μA. From that, it can be concluded, IBS rise times do not depend on the γ parameter or bunching voltages[2]. The heating term leads to an emittance growth of the six-dimensional phase volume of the bunched beam. Moreover, the approximate IBS model describes the measured data quite well.

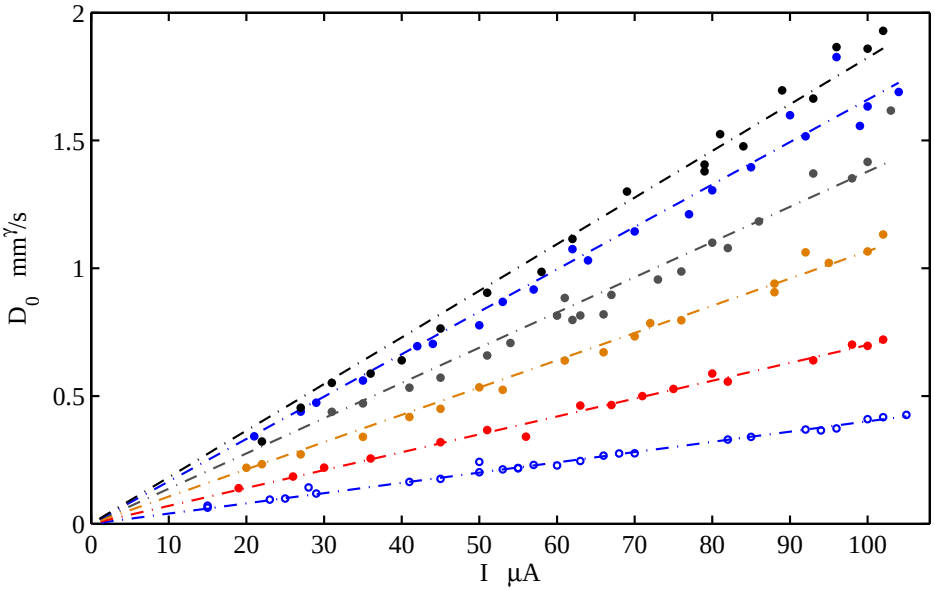

Figure 5.3: The horizontal component of the heating term D_i of IBS is measured as a function of the beam intensity. Hollow blue markers are data of the $^{12}C^{6+}$ coasting ion beam and red, yellow, gray, blue, black solid markers represent the bunched $^{12}C^{6+}$ ion beams at resonator voltages of 46.5 V, 93 V, 139.5 V, 186 V, 232.5 V, respectively.

[2]If the bunching voltage is approximately 100 V or higher.

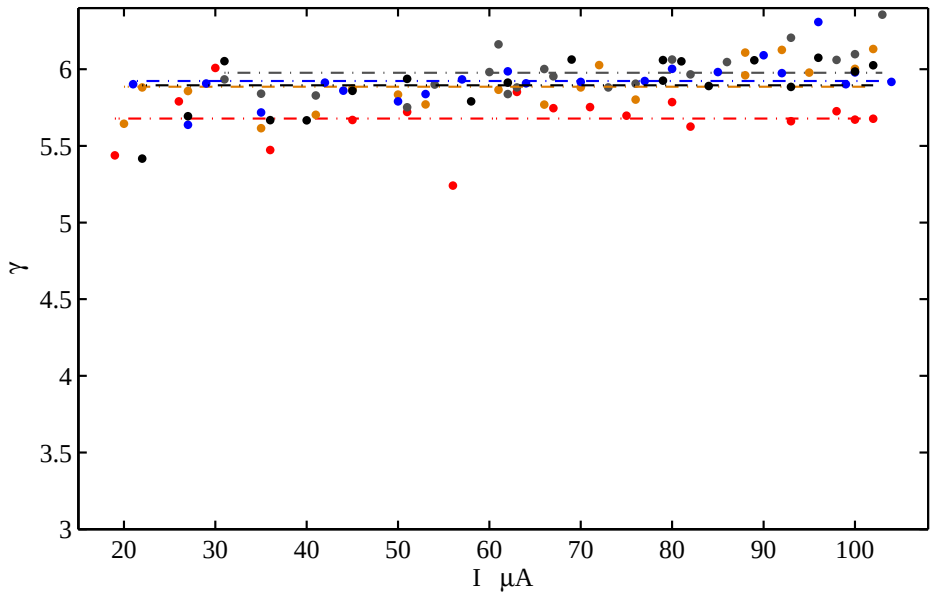

Figure 5.4: Determination of the $\overline{\gamma}$ parameter of IBS with bunched $^{12}C^{6+}$ ion beams at different resonator voltages as a function of intensity. The red, yellow, gray, blue, black solid markers represent the bunched $^{12}C^{6+}$ ion beams at resonator voltages of 46.5 V, 93 V, 139.5 V, 186 V, 232.5 V, respectively.

5.3 Equilibrium beam width

The quality of the particle beam is measured in terms of its emittance. This knowledge is necessary for the accelerator designers, operators and experimentalists. To investigate space-charge effects at the TSR the equilibrium emittance of the ion beam is important as well. By measuring the ion beam's spatial and angular distributions, the emittance can be estimated. Beam width growth rates due to IBS are given by:

$$\frac{1}{\sigma_{x,y}}\frac{d\sigma_{x,y}}{dt} \propto \frac{q^4 N}{A^2 \sigma^{\gamma} \beta^3}, \tag{5.9}$$

which can be compensated by applying electron cooling:

$$\frac{1}{\sigma_{x,y}}\frac{d\sigma_{x,y}}{dt} \propto -\frac{n_e q^2}{A}. \tag{5.10}$$

Therefore, the following equation determines the equilibrium state between IBS and electron cooling:

$$c_1 \cdot \frac{q^4 N}{A^2 \sigma^{\gamma} \beta^3} - c_2 \cdot \frac{n_e q^2}{A} = 0, \tag{5.11}$$

where c_1 and c_2 are constants. From eq. 5.11 the beam width at equilibrium is given by:

$$\sigma_{x,y} \propto \left(\frac{q^2}{A} \cdot \frac{N}{n_e \beta^3}\right)^{\frac{1}{\gamma}}. \tag{5.12}$$

The equilibrium emittances $\epsilon_{x,y}$ can be determined from eq. 3.27 by the measured 1 σ value of the spatial distribution of the beam. Transverse beam width measurements are conducted with 73.3 MeV coasting and bunched $^{12}C^{6+}$ ion beams at different bunching voltages as a function of intensity. Fig. 5.5 shows the horizontal beam width measurements at equilibrium, a power law relationship:

$$\sigma_{x_0} = constant \cdot I^{\alpha} \tag{5.13}$$

is fitted through the data, where α=0.25969 and the *constant*=0.14095 is found for the coasting beam.

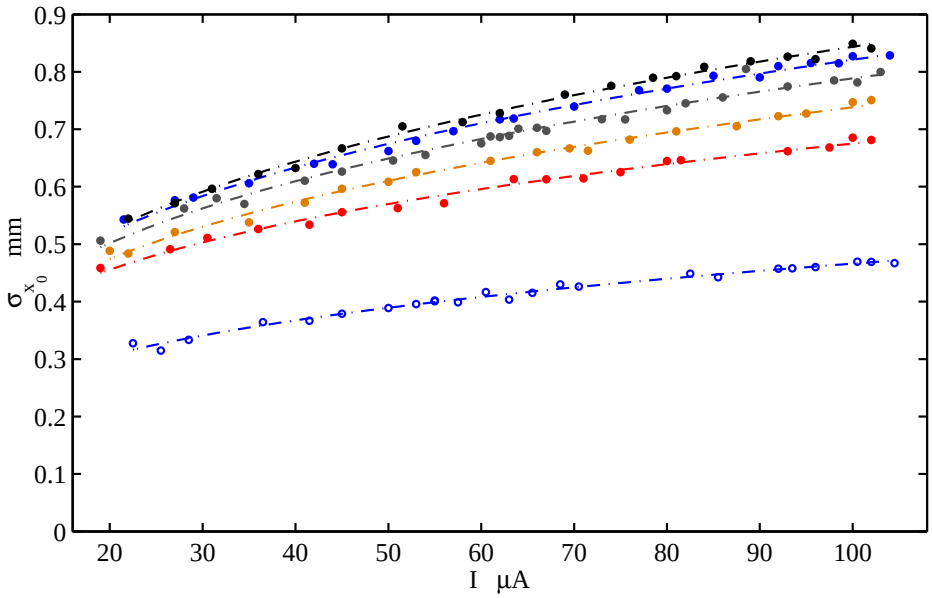

Figure 5.5: Horizontal beam width at equilibrium state is measured with 73.3 MeV coasting and bunched $^{12}C^{6+}$ ion beams at different resonator voltages as a function of intensity. The hollow blue markers are the data for coasting beam and red, yellow, gray, blue, black solid markers represent the bunched $^{12}C^{6+}$ ion beams at resonator voltages of 46.5 V, 93 V, 139.5 V, 186 V, 232.5 V, respectively.

5.4 Heating terms of IBS

The IBS heating term can be obtained by re-writing eq. 5.5 and eq. 5.6 from the following set of equations:

$$\begin{aligned} c_i \cdot \frac{q^4}{A^2}\frac{N}{\beta^3}\frac{1}{\epsilon_x\epsilon_y\Delta p/p \cdot C} &= \frac{D_{i_c}}{\sigma^{\gamma_{i_c}}} \qquad \textit{coasting beam}, \\ c_i \cdot \frac{q^4}{A^2}\frac{N}{\beta^3}\frac{1}{\epsilon_x\epsilon_y\Delta p/p \cdot h \cdot l_{eff}} &= \frac{D_{i_b}}{\sigma^{\gamma_{i_b}}} \qquad \textit{bunched beam}, \end{aligned} \tag{5.14}$$

where the double subscripts[3] i_c and i_b express three components of the heating terms and the γ parameters for coasting and bunched beams, relatively. Dividing the eq. 5.14 for the coasting beam by the bunched beam, yields the following equation:

$$\frac{h \cdot l_{eff}}{C} = \frac{D_{i_c}}{D_{i_b}}\sigma^{(\gamma_{i_b}-\gamma_{i_c})}. \tag{5.15}$$

The ratio on the left side of eq. 5.15 is so-called bunching factor B defined as:

$$B = \frac{h \cdot l_{eff}}{C}. \tag{5.16}$$

To determine the bunching factor from eq. 5.15, the heating terms D_{i_c}, D_{i_b}, the parameters γ_c, γ_b and the beam width σ of the stored bunched ion beam in the equilibrium between IBS and electron cooling have to be known. As shown in fig. 5.3, $D_{i_c} \propto I$ and $D_{i_b} \propto I$ and therefore, the bunching factor B should scale as:

$$B \propto \sigma^{(\gamma_b-\gamma_c)}. \tag{5.17}$$

Furthermore, the equilibrium beam width σ_0 of the bunched ion beam scales as $\sigma_0 \propto I^\alpha$ resulting in:

$$B \propto I^{\alpha(\gamma_b-\gamma_c)}. \tag{5.18}$$

For cooled bunched ion beams $B \propto l_{eff}$, where l_{eff} is the effective bunch length and $l_{eff} \propto I^{1/3}$[34], thus:

$$\frac{1}{3} = \alpha(\gamma_b - \gamma_c) \tag{5.19}$$

The parameters α, γ_b, $\alpha\cdot(\gamma_b-\gamma_c)$, for different resonator voltages are summarized in table 5.1 for the horizontal degree of freedom. The values of $\alpha(\gamma_b-\gamma_c)$ term are calculated with $\gamma_c = 4.75$ of the coasting beam. The theoretical value for the $\alpha(\gamma_b-\gamma_c)$ term is 1/3 given in eq. 5.19. The experimental values are consistent with the theoretical value of 1/3, if the resonator voltage is higher than 93 V. From the measured IBS parameters such as D_{i_c}, D_{i_b}, γ_c, γ_b, α, it is possible to calculate the bunching factor of ion beams using eq. 5.15. In fig. 5.4 the inverse bunching factor, derived from the experimental IBS data, for different

[3]It is essential to write these parameters in this form to derive the bunching factor from the results of coasting and bunched beams.

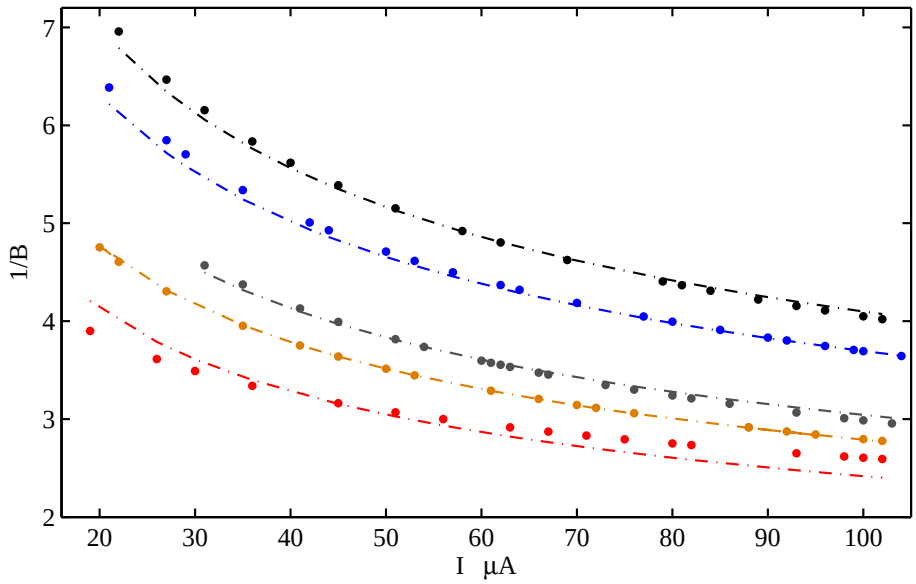

Figure 5.6: Inverse bunching factor for the $^{12}C^{6+}$ ion beams at different resonator voltages as a function of intensity. Solid markers represent experimental data and dash-dot lines are analytical calculations of inverse bunching factor.

resonator voltages and ion intensities are shown as colored markers. The bunching factors calculated from the half-bunch lengths[34] of electron cooled ion beam are fitted to the experimental data, shown as dash-dot lines. In this fit it is assumed that $l_{eff} = a \cdot w$, where w is a half bunch length and a is a fit parameter. By fitting the experimental data $a = 2.45$ is determined, predicting slightly larger bunch lengths than the maximum theoretical value of $2 \cdot w$.

Table 5.1: Experimental IBS parameters at different resonator voltages.

U[V]	α	γ_b	$\alpha \cdot (\gamma_b - \gamma_c)$
46.5	0.2440	5.68	0.2440
93.0	0.2748	5.83	0.2940
139.5	0.2810	5.90	0.3203
186.0	0.2834	5.90	0.3230
232.5	0.2953	5.84	0.3319

5.5 Longitudinal IBS measurements

From a simplified IBS model, eq. 5.8 describing the growth of the beam width with time should be also valid for the momentum spread. Therefore, IBS experiments with 73.3 MeV, $^{12}C^{6+}$ coasting ion beam are conducted along the longitudinal degree of freedom in order to test the validity of eq. 5.8.

In experiments, electron cooling of the ion beam is applied simultaneously with the injection to achieve an equilibrium between IBS and cooling. To investigate IBS the cooler must be switched off and, the development of the momentum spread measured with Schottky noise analysis, is recorded using a real time spectrum analyzator. The spectrum length is 64 ms, a span of the RSA is set to 10 kHz in all the measurements and a time-interval of the spectrum is 64 ms. That means, every 64 ms a Schottky spectrum of the beam is measured.

About one second before switching off the electron cooling, the spectrum analyzator starts recording the time evolution of the Schottky spectrum. The measurements include the equilibrium state of the ion beam at $t < 1$ s and monitor the influence of IBS while electron cooling is switched off after $t = 1$ s. A screen snapshot of the RSA from longitudinal IBS measurements is shown in fig. 5.7, where the time development of the Schottky spectrum is displayed. It can be seen that a moment of switching off the electron cooling represents a rapid increase of the Schottky band-frequency spread[4] of the stored ion beam.

In the data analysis every three time-frames are combined and every four acquisition points along the frequency axis are binned, in order to improve the statistical quality. The combined time-frames are then fitted with gaussian functions to estimate the σ values of the beam profile. An example of the gaussian fit of time frame at $t = 0.352$ s of the data is shown in fig. 5.8. Fig. 5.9 shows the resultant σ values of the spectrum as a function of time and also, represents the time development of the ion beam-profile snapshot as indicated previously (see fig. 5.7). The dash-dot line through the data is a fit using eq. 5.8 where γ, σ_0 and D_i are the fitting parameters. The slight oscillation of the data exists around the fit along the frequency spread of the ion beam due to noise. Measured in the intensity range of 4 to 26 μA, the γ parameters of longitudinal momentum spread due to IBS are shown in fig. 5.10, where dash-dot line is a fit resulting in an average value of $\overline{\gamma}$=5.75, which is higher than the expected γ=5. To determine the heating term of IBS for different intensities, the $\overline{\gamma}$ parameter is kept constant in fitting the data and the obtained results are shown in fig. 5.11 as a function of intensity.

[4]see fig. 5.9

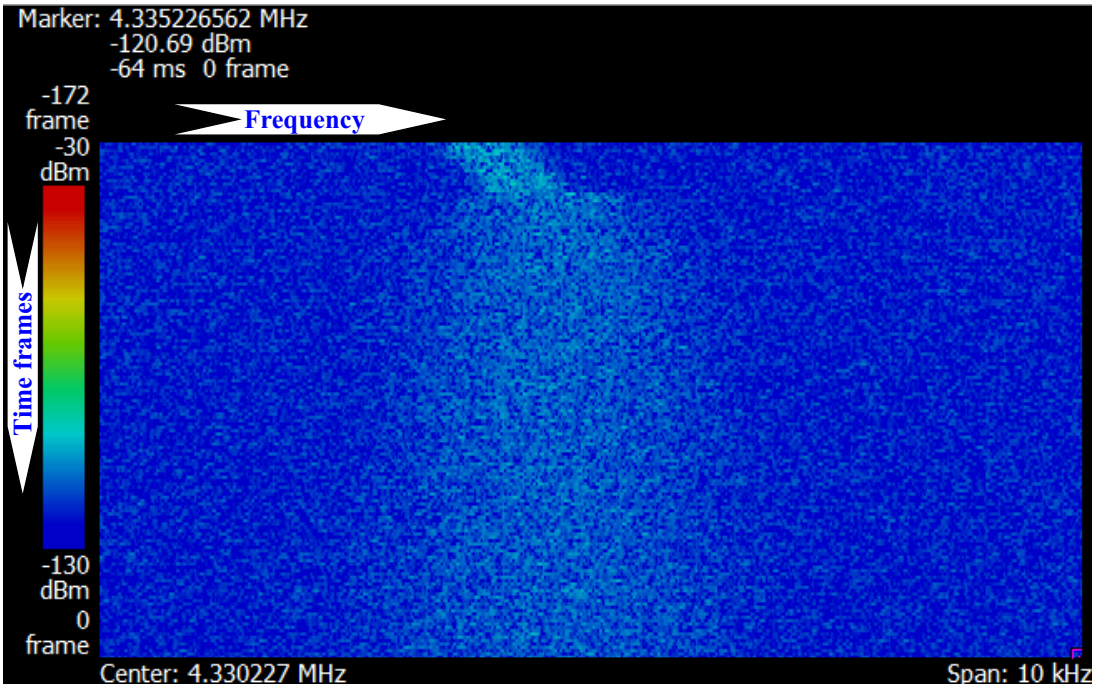

Figure 5.7: Time evolution of the Schottky noise spectrum at equilibrium state and after switching off the electron cooler. Starting from equilibrium the Schottky noise spectrum of the 73.3 MeV $^{12}C^{6+}$ ion beam is measured at a harmonic number of 7.

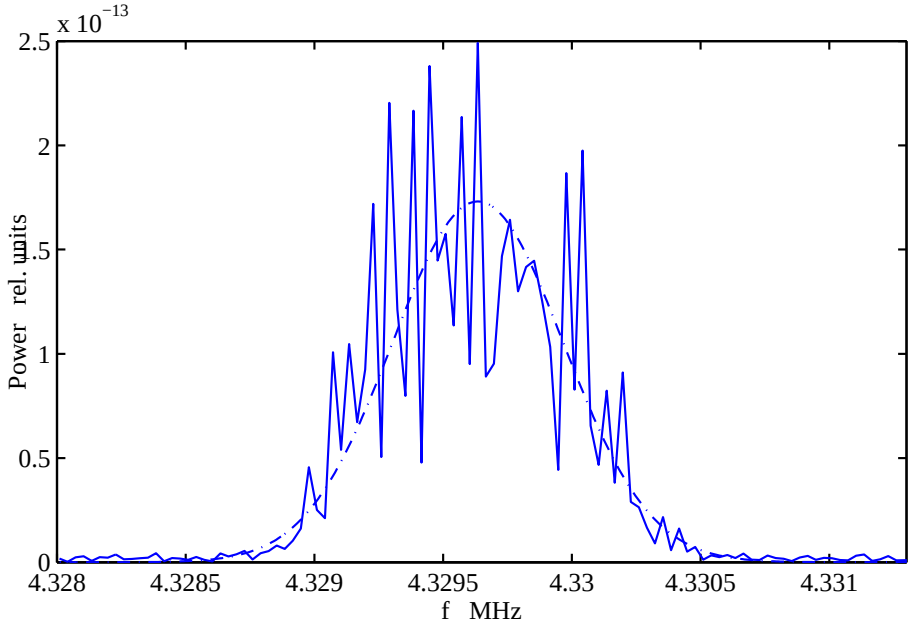

Figure 5.8: An example of the longitudinal ion beam profile and a gaussian fit measured at t=0.352 s.

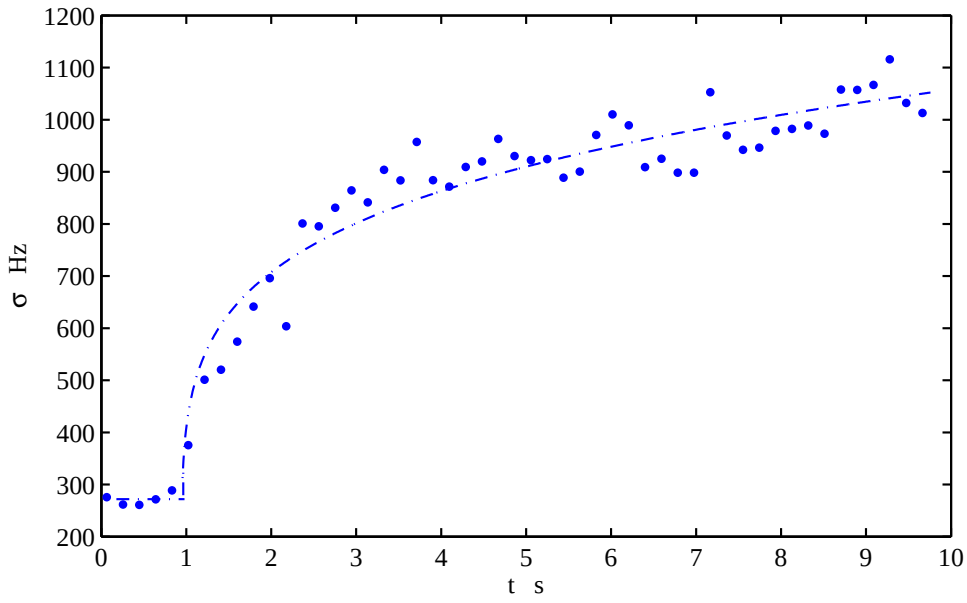

Figure 5.9: Development of the frequency spread in Schottky spectrum of the 73.3 MeV $^{12}C^{6+}$ coasting ion beam at equilibrium and after switching off the electron cooler at t=1 s.

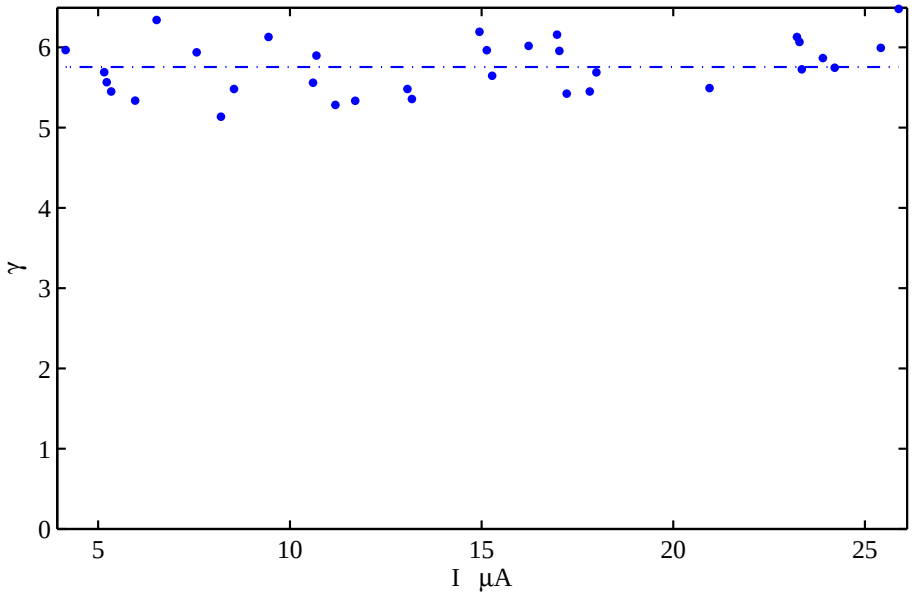

Figure 5.10: Measured γ parameter of longitudinal IBS with the $^{12}C^{6+}$ coasting ion beam as a function of intensity.

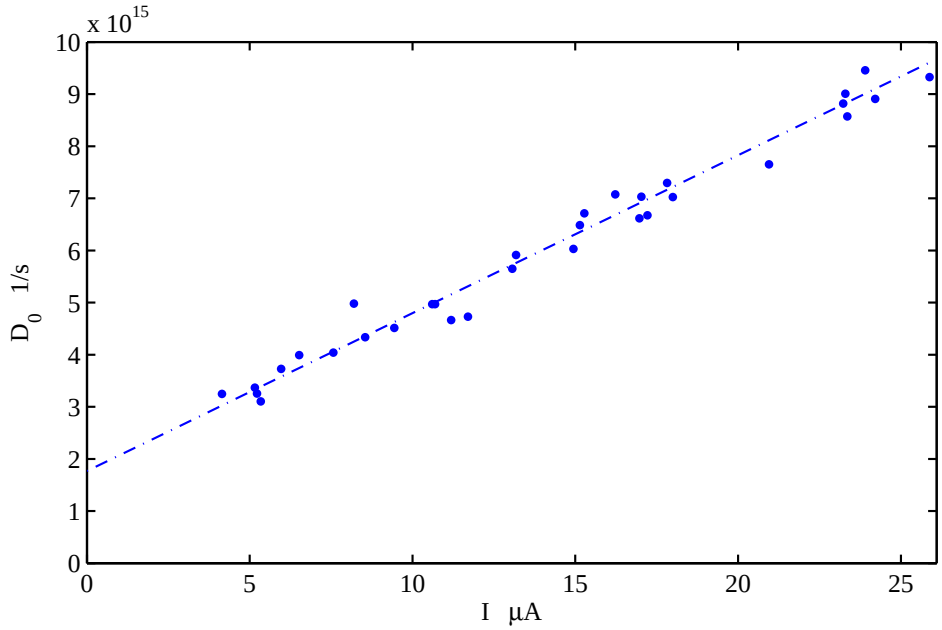

Figure 5.11: The longitudinal heating term of IBS measured with the 73.3 MeV, $^{12}C^{6+}$ coasting ion beam as a function of the intensity.

Equilibrium momentum spread

The equilibrium momentum spread $\Delta p/p$ of the electron cooled ion beam at high intensity, low ion velocity and under excellent vacuum conditions (to make multiple scattering in the residual gas negligible) is determined by the electron cooling force and IBS heating. The experimental longitudinal momentum spread $\Delta p/p$ (Δp is the standard deviation of a gaussian distribution) in the equilibrium between IBS and electron cooling ($n_e = 8 \cdot 10^6$ cm^{-3}) are shown as a function of the intensity in fig. 5.12. The measurements are performed for the $^{12}C^{6+}$ coasting ion beam having a velocity of β=0.11. It can be seen that the momentum spread increases with intensity. A fit $\Delta p/p = constant \cdot I^{\alpha}$ through the data yields an exponent α=0.21 which resembles to the expected value of $\alpha = \frac{1}{\gamma}$=0.2.

5.6 IBS at low velocities

The beam width growth rate due to IBS (see eq. 5.5) scales with the beam velocity as:

$$\frac{1}{\sigma_{x,y}} \frac{d\sigma_{x,y}}{dt} \propto \frac{1}{\beta^3}. \tag{5.20}$$

To verify this scaling law, IBS experiments are conducted at two different energies of 73.3 MeV and 9.77 MeV using $^{12}C^{6+}$ ion beams. Electron cooling of the ion beam is applied simultaneously with injection to achieve the equilibrium between IBS and electron cooling. Ion beams of 73.3 MeV and of 9.77 MeV are cooled for 1 s and for 4 s, relatively. Longer cooling is applied for lower energy ion beam to assure the equilibrium.

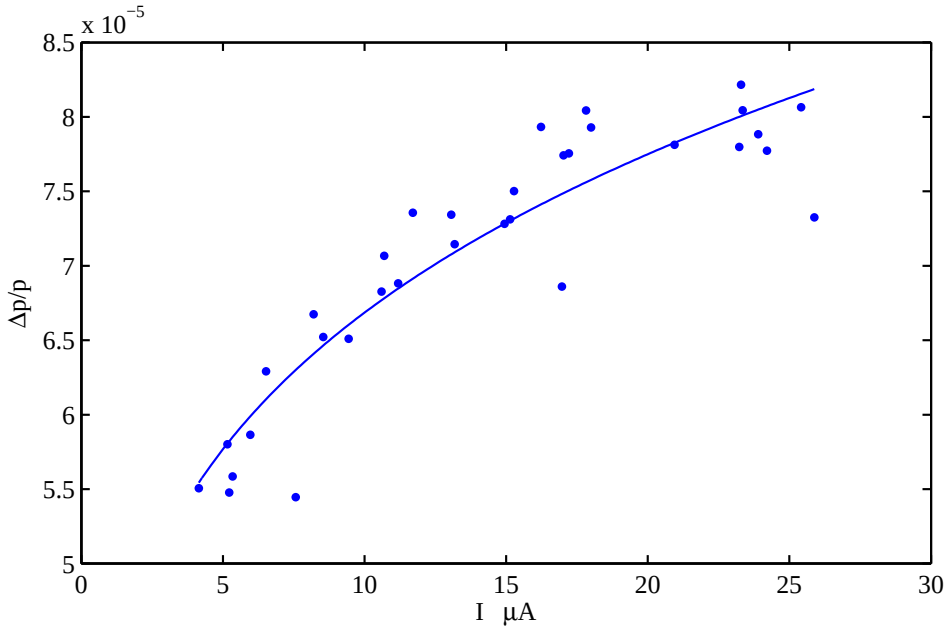

Figure 5.12: Equilibrium momentum spread of the 73.3 MeV $^{12}C^{6+}$ coasting ion beam as a function of intensity.

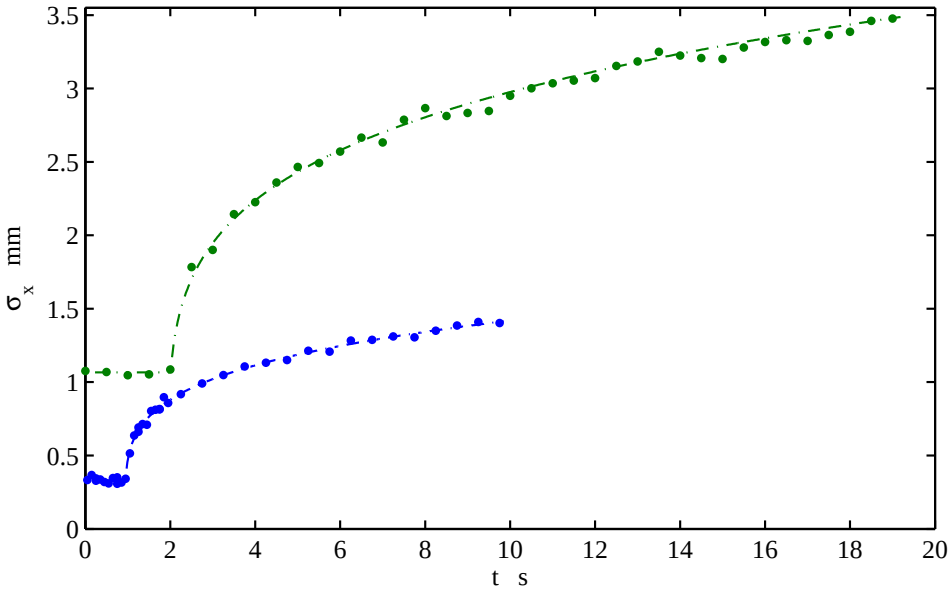

Figure 5.13: IBS measurements with 73.3 and 9.77 MeV $^{12}C^{6+}$ ion beams as a function of time. Blue and green markers are data with 73.3 MeV and 9.77 MeV ion beam, relatively.

Measurements are obtained at the same number of particles to show the energy dependency of the equilibrium beam width and the IBS rates. The BPM starts recording the data 1 s and 2 s before switching off the electron cooler, with a total measuring time of 10 s and 20 s. Both data displaying the development of the horizontal beam profiles are shown in fig. 5.13 as a function of time. It can be seen that, the IBS rates are significantly higher at the lower energy. The corresponding IBS parameters are obtained by fitting eq. 5.8 to both data (see fig. 5.13). All individual values of γ parameter for both energies as a function of the number of the stored particles are combined and using a constant fit to the data as shown in fig. 5.14, $\overline{\gamma}$=4.8 is determined.

The heating terms of IBS data for both energies are analyzed using the same constant $\overline{\gamma}$=4.8 parameter the results are shown in fig. 5.15. Independent from the energy both heating terms scale with the number of particles whereas the slope of the heating term at 9.77 MeV significantly higher than the slope determined at 73.3 MeV.

If the heating term of IBS scales as:

$$D_0 \propto \frac{N}{\beta^{\kappa}}, \tag{5.21}$$

where the exponent κ can be determined as:

$$\kappa = \frac{ln(a_2/a_1)}{ln(\beta_1/\beta_2)}. \tag{5.22}$$

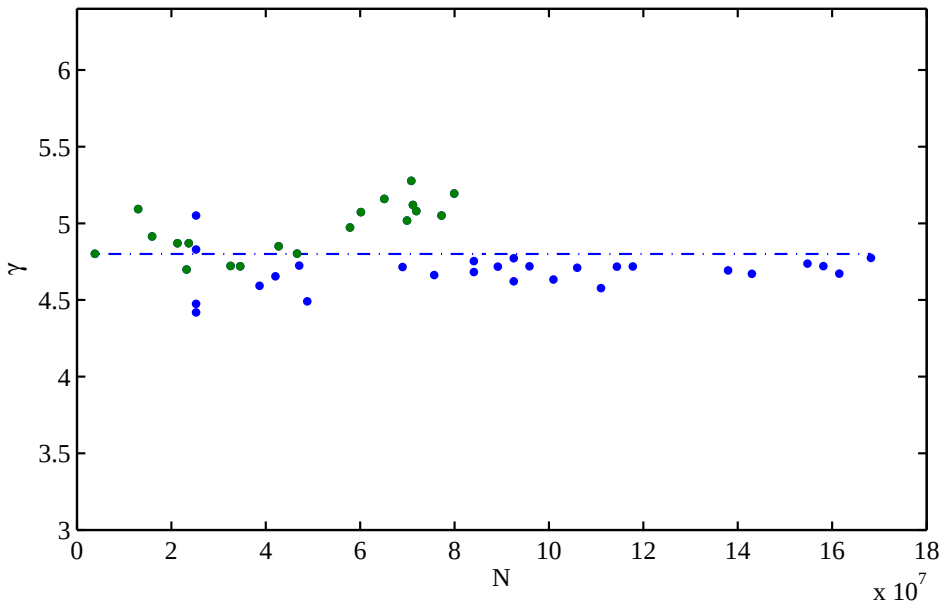

Figure 5.14: Measured γ parameter of IBS as a function of the number of stored particles. The blue and green markers are the data measured with 73.3 and 9.77 MeV $^{12}C^{6+}$ ion beams, relatively.

where β_1 and β_2 are initial and final velocities of the ion beam. From the linear fit

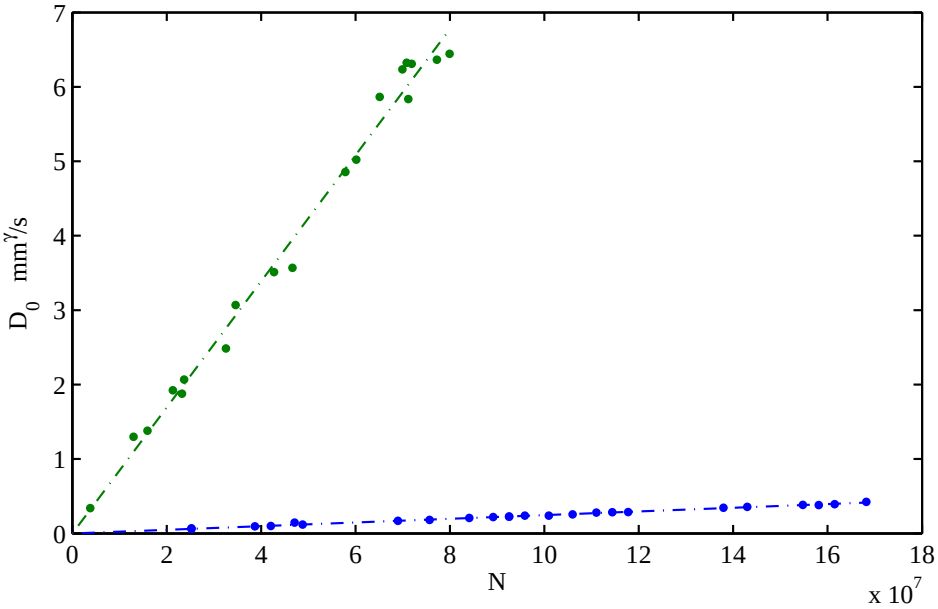

Figure 5.15: Heating term of IBS, measured with 73.3 MeV and 9.77 MeV $^{12}C^{6+}$ ion beams as a function of the number of stored particles in the ring.

through the heating terms of IBS at different energies, $a_1 = 0.246 \cdot 10^{-8}$ mm$^\gamma$/s and $a_2 = 8.469 \cdot 10^{-8}$ mm$^\gamma$/s are determined. According to eq. 5.22 this leads to $\kappa \approx 3.5$ which is slightly higher than the theoretical value $\kappa \approx 3$.

6 Deceleration and acceleration of the charged particle beam

Acceleration is the rate of increase in velocity. It indicates how much faster or slower a moving particles gets every second. A negative acceleration is called deceleration, which slows down the velocity.

The first step of the acceleration or deceleration cycle in the TSR is bunching of the multiturn injected ion beam. In the bunching process, the injected ion beam will be trapped into the RF bucket with maximum efficiency. That means, for effective bunching the RF voltage must be large enough as compared to the longitudinal phase space of the beam.

An ion is called a synchronous particle if its f_0 revolution frequency satisfies the following condition and remains on a closed orbit:

$$f_0 = \frac{f_{RF}}{h}, \tag{6.1}$$

where h is an integer number and f_{RF} is the RF frequency. The RF phase of the synchronous particle $\phi_s(n)$ after n passages trough the resonator is given by:

$$\phi_s(n) = n \cdot 2\pi h + \phi_s. \tag{6.2}$$

The phase ϕ_s in eq. 6.2 is called the synchronous phase. For bunching the injected beam in the TSR, the synchronous phase is set automatically to $\phi_s = 0$. If it is 0, the synchronous particle will enter the resonator always at the RF voltage $U_{RF} = 0$ and does not change its energy.

Then, to change the energy of an ion beam in the storage ring the ions have to interact with an electrical field. At the TSR this electrical field is generated in the RF resonator[1] and used for bunching, accelerating and decelerating the ions. The resonator consists of 20 ferrites and a capacity parallel to the acceleration gap. The accelerating voltage across the gap $U_{RF}(t)$ of the RF resonator has a sinusoidal form:

$$U_{RF}(t) = U_0 \ \sin\ (2\pi f_{RF} t + \phi_0), \tag{6.3}$$

where U_0 is the amplitude of the resonator voltage. U_0 and f_{RF} are slowly varying functions of t, but can also be constant for bunching. The energy gain of synchronous particle per turn after each passage through the RF resonator is the same:

$$\Delta(E)_{turn} = QU_0 \ \sin\ (\phi_s). \tag{6.4}$$

The synchronous phase of acceleration or deceleration of ions in the TSR is typically $|\phi_s| \approx 1^\circ$ and set automatically by the function $f_{RF}(t)$. The user-developed program for the ramp

[1] Characterized in the chapter 2

calculation is written in Mathematica. This program allows including corrections for any calculated function during and after the ramping cycle. The generated function to ramp the magnets is sent to function generator cards which control the magnet power supplies. For acceleration or deceleration in the TSR the function $f_{RF}(t)$, the RF frequency and the currents of all power supplies are calculated from the beam rigidity[2] $B\rho(t)$. The table of the calculated RF frequency will be sent to a DSP driven synthesizer card generating the frequency for the RF system. The function generator cards as well the DSP driven synthesizer cards were developed at MPIK to enable flexible acceleration and deceleration procedures. The rigidity of the injected ion beam is determined by measuring the Schottky spectrum f_{Sch} at the integer number h of the RF, used to bunch the beam. The RF frequency follows the variation of the beam rigidity $B\rho$:

$$f_{RF} = h\frac{(B\rho)cQ}{C_0\sqrt{(B\rho)^2q^2 + c^2m^2}}. \tag{6.5}$$

With eq. 6.5 and $f_{RF} = f_{Sch}$ the rigidity of the injected ion beam can be calculated, because the circumference of the storage ring C_0 is known. From the rigidity curve for the acceleration or deceleration process, the current functions of the main dipole magnets are calculated taking into account saturation effects. The magnetic field B_d of the main dipole magnets is directly proportional to the magnetic rigidity of the beam:

$$B_d \propto B\rho = \frac{p_s}{Q}, \tag{6.6}$$

where p_s is the momentum of synchronous particle, the coefficient of proportionality is the inverse of the curvature radius ρ_0 of the central orbit in the dipole. The TSR main dipole magnet is built for a curvature radius of $\rho_0 = 1.15$ m. However, the design value of ρ_0 was not directly used to calculate the magnetic fields of the dipole magnets from the rigidity. The magnetic field B_d of the main dipole magnet is known by setting them to a value corresponding to the injection energy taking into account saturation effects in the iron of the TSR magnets. The magnetic rigidity $B\rho_0$ and the main dipole field $B_{d,0}$ at injection determines $\rho_0 = \frac{B\rho_0}{B_{d,0}}$ to calculate the necessary magnetic field B_d to bend the ion beam with rigidity $B\rho$:

$$B_d = \frac{B\rho}{\rho_0}. \tag{6.7}$$

The main dipole magnet field B_d is excited with the current I_M coming from the main power supply and the current I_c from the correction power supply. Taking into account the saturation effect, the following scaling law was used to calculate the function of the main dipole currents for the acceleration and deceleration process:

$$I_M = I_{M,0}\frac{f(B_d)}{f(B_{d,0})} \tag{6.8}$$

$$I_c = I_{c,0}\frac{f(B_d)}{f(B_{d,0})}, \tag{6.9}$$

[2]Property of resisting for bending

where $f(B_d)$ is the function shown in fig. 6.1. $I_{M,0}$ and $I_{c,0}$ are the currents at the

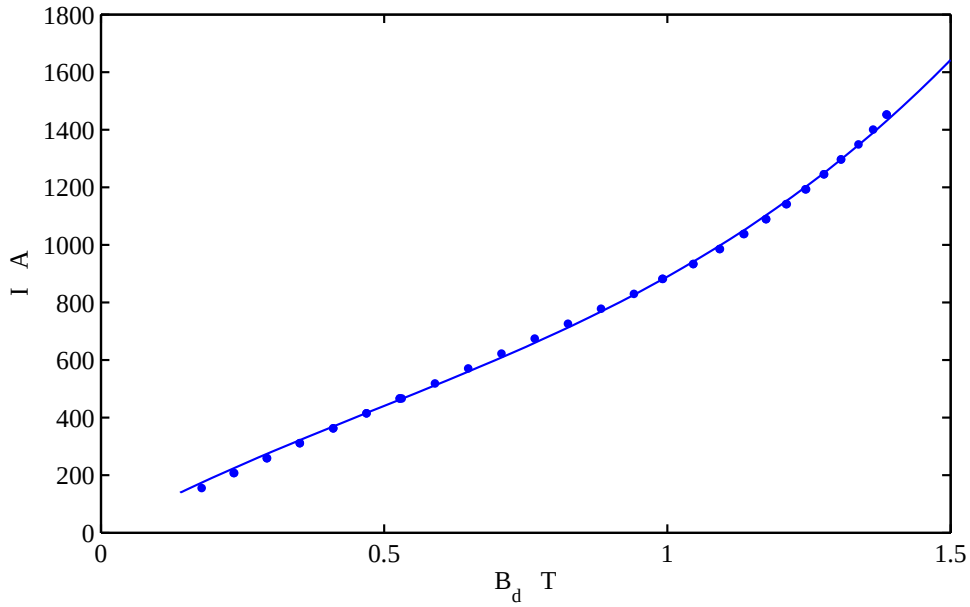

Figure 6.1: Current of the power supply as a function of the main dipole magnetic field.

injection energy of the main dipole power supply and the power supply exciting the correction winding. For the quadrupole magnets and other magnets of the storage ring no saturation measurements exist, therefore a linear scaling between beam rigidity $B\rho$ and excitation current I was assumed to calculate the power supply currents:

$$I = I_0 \frac{B\rho}{B\rho_0}, \tag{6.10}$$

where I_0 is the power supply current and $B\rho_0$ the beam rigidity at injection. The ramping time is limited by the induced voltage in the correction windings of the iron cores on the TSR main dipole magnets and it has to be kept below 6 V for proper operation of the power supplies which are presently in use. The KM power supplies provide the correction windings with current and during the ramp cycles the total voltage in the correction windings should be within the permissible range of 0 to 6 V. The power supply voltage U is given by the induction voltage induced in the coils and the voltage on the ohmic resistance R of the coils:

$$U = nA\frac{dB_d}{dt} + RI, \tag{6.11}$$

where n is the number of the coil windings and A is the iron area inside the correction coil.

6.1 Methods for the current measurements at low intensities

Current measurements are important to define the efficiency of the acceleration or deceleration processes. The minimum current that can be detected by the DC current transformer at the TSR is 1 μA. During deceleration of the ion beam the revolution frequency decreases, resulting in low current, which is difficult to measure with the common DC transformer.

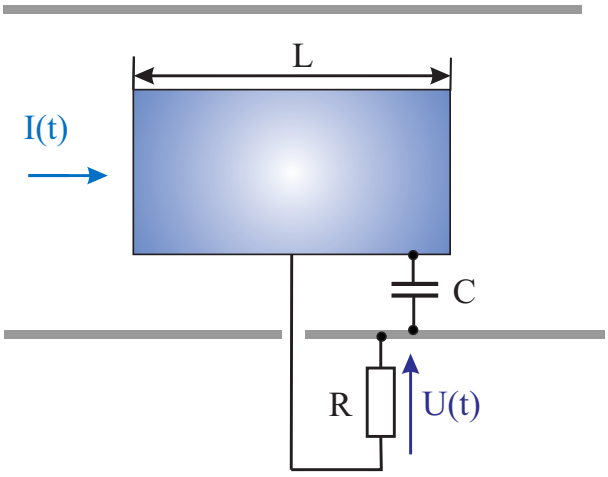

Figure 6.2: Capacitive pick-up.

Alternatively, current pick-up as shown in fig. 6.2, consisting of a tube surrounding the stored ion beam, can be used to determine the total intensity of a bunched ion beam by measuring the pick-up voltage $U(t)$. If the bunch length is much larger than the pick-up length L, the pick-up voltage can be derived by the following differential equation[35]:

$$\frac{L}{v}\dot{I}(t) = C \cdot \dot{U}(t) + \frac{U(t)}{R}, \tag{6.12}$$

where v is the ion velocity. The total capacity from the pick-up, the cable connecting the pick-up with the pre-amplifier and the pre-amplifier is given by C. If the pick-up electrode is loaded with a pre-amplifier with a very high input resistance R the term $U(t)/R$ can be neglected in eq. 6.12 and the pick-up voltage is then directly proportional to the ion beam intensity:

$$U(t) = \frac{1}{v}\frac{L}{C}I(t). \tag{6.13}$$

The average stored ion current $\bar{I}$ can be determined by integrating eq. 6.13 over one RF period:

$$\bar{I} = C_0 f_0^2 h \frac{C}{L}\int U(t)dt, \tag{6.14}$$

where f_0 is the revolution frequency, h the number of bunches and C_0 the circumference of the storage ring. If the total capacity C is known, an absolute current measurement of the stored ion beam is possible by integrating the measured pick-up voltage in time domain, taking into account the ion revolution frequency. Therefore, the pick-up signal calibration measurements are performed as a function of beam intensity using $^{12}C^{6+}$ ions at 73.3 MeV.

Calibration of the pick-up signal

Electron-cooled, short ion-beam bunches have the parabolic momentum spread profiles in the space-charge limit. In this case, the voltage of the resonator $U(\Delta\phi) = U_0 \cdot \sin(\Delta\phi + \phi_s)$ is completely compensated by the longitudinal space-charge voltage of the ion beam and the synchrotron oscillation of each ion in the bunch freezes. This condition leads to the longitudinal space-charge limit of the ion beam. The ion beam current in the time domain can be calculated from[37]:

$$I(t) = \frac{3N_bQ}{4w_t}\left(1 - \frac{(t-t_0)^2}{w_t^2}\right), \tag{6.15}$$

where w_t bunch length in time domain, N_b is the number of particles in a bunch. From eq. 6.13 and eq. 6.15 the pick-up signal of the bunch can be determined:

$$U(t) = \frac{\alpha L}{Cv} I(t) = \frac{3N_bQL\alpha}{4Cvw_t}\left(1 - \frac{(t-t_0)^2}{w_t^2}\right) \tag{6.16}$$

where α is an amplification factor of the pre-amplifier connected to the pick-up. The number of particles N_b in a bunch is given by:

$$N_b = \frac{I}{Qf_{RF}}. \tag{6.17}$$

By inserting eq. 6.17 into eq. 6.16 with $v = C_0 \cdot f_0$, the following equation is obtained:

$$\int_{-w_t}^{w_t} U(t)\,\mathrm{d}t = \frac{L\alpha}{C_0 C} \cdot \frac{Q}{f_{RF}} \cdot N_b. \tag{6.18}$$

The constant term in eq. 6.18 is a calibration factor of the pick-up:

$$\frac{L\alpha}{C_0 C} = constant. \tag{6.19}$$

By integrating eq. 6.18 the pick-up signal of the electron-cooled ion beam can be expressed as a function of intensity:

$$U(t) = \frac{3IL\alpha}{4CC_0 f_0^2 h w_t}\left(1 - \frac{(t-t_0)^2}{w_t^2}\right). \tag{6.20}$$

The pick-up signal shown in fig. 6.3, is measured with the 73.8 MeV $^{12}C^{6+}$ ion beam at $h = 7$ and is fitted with eq. 6.20. In this measurement the bunching voltage of the RF resonator is set to 232.5 V and the beam current is 36 μA. A bunch length $w_t = 26.65\ ns$

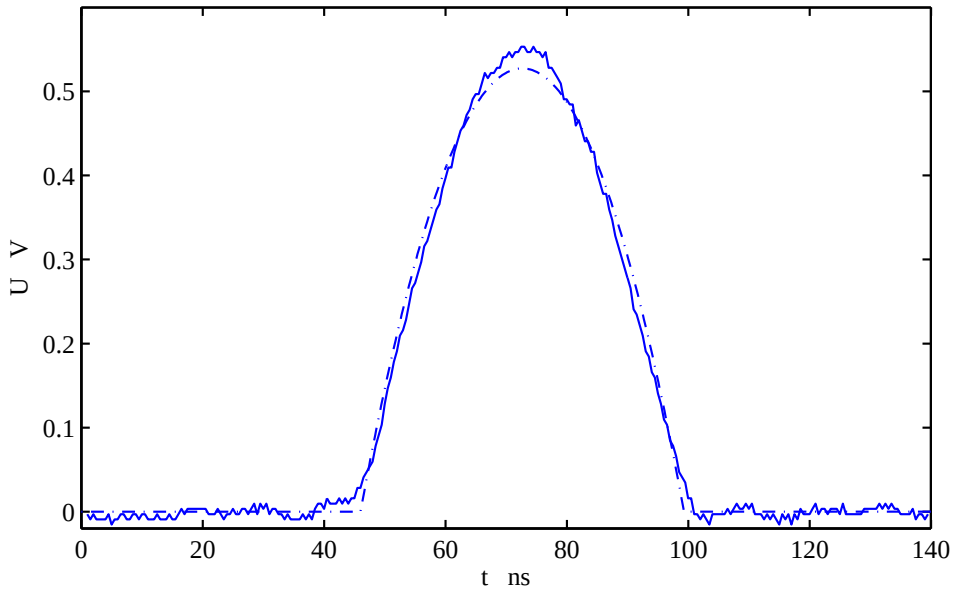

Figure 6.3: Measured bunch profile and its parabolic fit, at h=7. Blue solid line is the measured $^{12}C^{6+}$ ion beam profile, blue dash-dot line is a fit using a parabolic function.

is obtained from the fit. The area under data-curve is estimated from the integral $\int U(t)\,\mathrm{d}t$ of the pick-up signal as a function of the beam intensity and is shown in fig. 6.4 for different harmonic numbers. Fitting a linear function $f(I) = \kappa \cdot I$ to the data, κ is obtained from the slope of the fit, which is:

$$\kappa = \frac{L\alpha}{C_0 C f_0^2 h}. \tag{6.21}$$

The experimental calibration factor of the pick-up can be determined from κ, the results are listed in table 6.1. Theoretical values of the total capacity $C = (224.5 \pm 1.2)^{-12}$ F, the pick-up length $L = 0.085$ m and the amplification factor[3] α=198.96 in the frequency domain are assessed in[35]. Hence, the calibration factor of pick-up signal can be calculated:

$$\left(\frac{L\alpha}{C_0 C}\right)_{theory} = 1.36 \cdot 10^9 \ \frac{1}{F}, \tag{6.22}$$

and compared to the average experimental value which is found in good agreement:

$$\left(\overline{\frac{L\alpha}{C_0 C}}\right)_{exp.} = 1.417 \cdot 10^9 \ \frac{1}{F}. \tag{6.23}$$

According to eq. 6.13 the pick-up signal scales with the inverse of the ion velocity. To verify this dependency the $^{12}C^{6+}$ ion beam at the injection energy of 73.3 MeV is bunched, electron cooled and accelerated to 240 MeV. During acceleration the pick-up

[3] $\alpha(f[MHz]) = 198.96 - 2.95 \cdot 10^{-2} \cdot f$

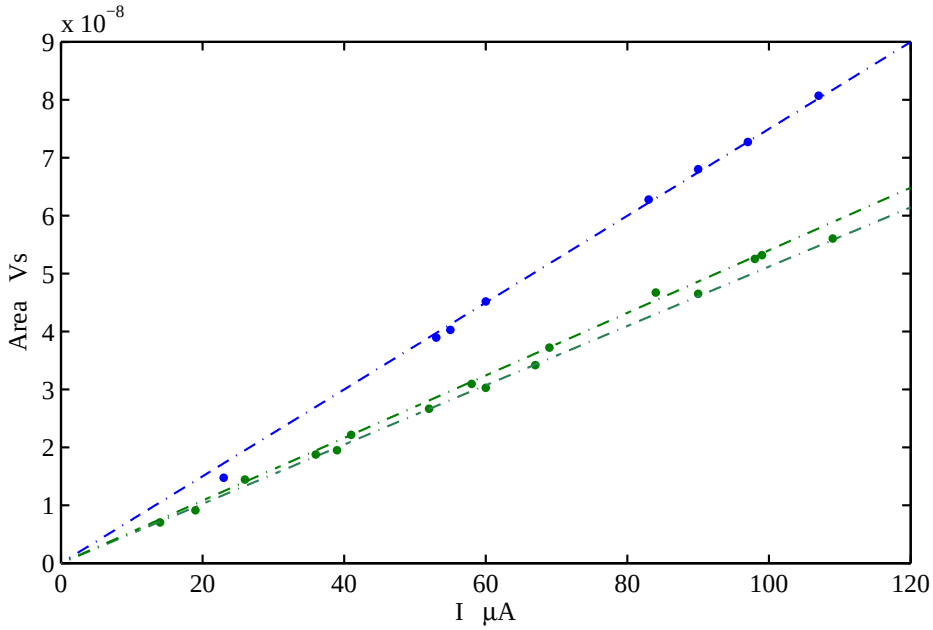

Figure 6.4: Calibration of the pick-up signal at harmonic numbers of $h = 5$ and $h = 7$. Areas under the pick-up signal curves at $h = 5$ and $h = 7$ are shown as blue and green markers. Linear fits through the data are shown as blue and green dash-dot lines, respectively.

signal is measured as a function of the revolution frequency f_0. About 98% of injected ions is accelerated to the final energy. Therefore, the number of ions are assumed to remain constant. Then, it is possible to estimate the pick-up signal area during acceleration by eq. 6.14:

$$\int U(t)dt = \frac{L}{C}\frac{QN}{C_0 h f_0}, \tag{6.24}$$

where the beam current is:

$$I = QNf_0. \tag{6.25}$$

Fig. 6.5 shows the integral of the measured pick-up signal as a function of the revolution

Table 6.1: Calibration factor of pick-up signal at different harmonic numbers of the revolution frequency.

h	κ $[\frac{1}{F \cdot Hz^2}]$	$\frac{L\alpha}{C_0 C}$ $[\frac{1}{F}]$
7	$5.403 \cdot 10^{-4}$	$1.447 \cdot 10^{9}$
7	$5.120 \cdot 10^{-4}$	$1.371 \cdot 10^{9}$
5	$7.499 \cdot 10^{-4}$	$1.435 \cdot 10^{9}$

frequency. The dash-dot line trough the data is a fit, using eq. 6.24, where the total capacity C is determined as a fit parameter. Hence, the total capacity C value 211.7 pF is obtained which is in agreement with the value of 224.5 pF measured with a LCR meter[4][35]. Measuring the pick-up signal in the time domain is a sensitive method to determine the efficiency of the acceleration or deceleration process, if the ion beam has a low intensity of 0.1 μA at velocities of $\beta \approx 0.1$.

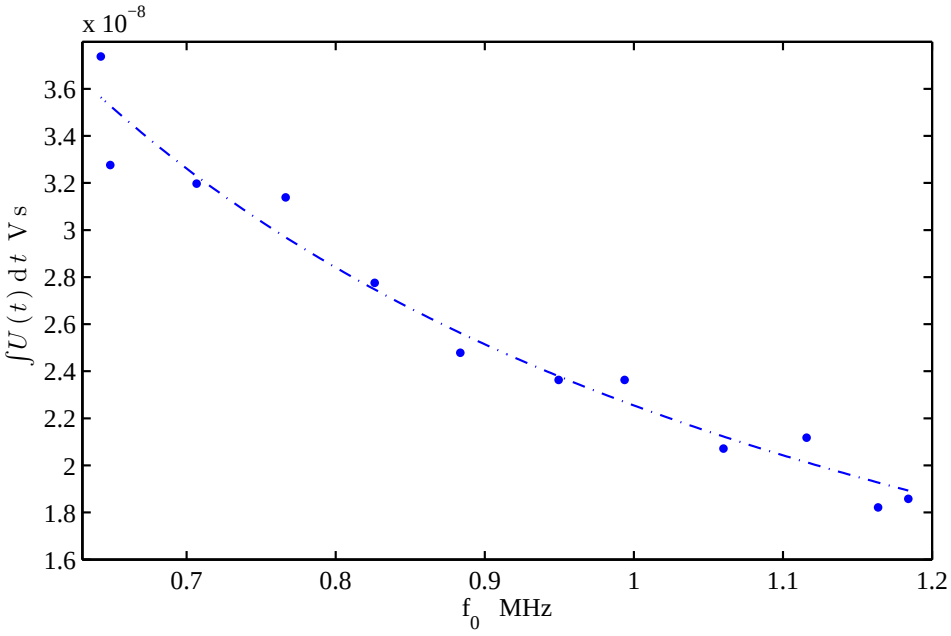

Figure 6.5: Integration of the pick-up signal as a function of the revolution frequency during acceleration of the $^{12}C^{6+}$ ion beam.

Intensity measurements with a mixed signal spectrum and BPM

To asses the number of stored ions, the measurement of the pick-up signal spectrum is an effective method at low intensities. The "spectrum" of the frequency components is the frequency domain representation of the signal. The beam current is a periodic signal, therefore, can be expressed in Fourier series:

$$I = \frac{a_0}{2} + \sum_{h=1}^{\infty} \Big(a_h \cdot \cos(h\omega_0 t) + b_h \cdot \sin(h\omega_0 t) \Big) \tag{6.26}$$

where a_0, a_h, b_h are Fourier coefficients. The spectrum of the current is given by $\hat{I} = \sqrt{a_h^2 + b_h^2}$, for symmetric functions $b_h = 0$ and $\hat{I} = a_h$.

From eq. 6.13 and, if the pick-up electrode is loaded with a pre-amplifier with a very high input resistance, the spectrum of the pick-up voltage can be expressed by:

$$\hat{U}_h = \frac{\alpha \cdot L}{v \cdot C} \hat{I}_h, \tag{6.27}$$

[4]A LCR meter (Inductance (L), Capacitance (C), and Resistance (R)) is a piece of electronic test equipment used to measure the inductance, capacitance and resistance of a component.

where $\hat{I}_h$ is the current spectrum, at the harmonic number h of the RF frequency f_0 ($f_0 = \frac{\omega_0}{2\pi}$), of the beam having a parabolic charge distribution which is determined by the bunch length w:

$$\hat{I}_h = \frac{6 \cdot \bar{I}(\sin(hw\omega_0) - hw\omega_0 \cos(hw\omega_0))}{h^3 w^3 \omega_0^3}. \tag{6.28}$$

The dependency of the bunch length w on the average beam current $\overline{I}$ is given by[37]:

$$w = C_0 \sqrt[3]{\frac{3(1 + 2\ln(\frac{R}{r}))\bar{I}}{2^4\pi^2 c^4 \epsilon_0 \gamma^2 h^2 \beta^4 U_0}}. \tag{6.29}$$

The bunch length w in eq. 6.29 is defined by the beam intensity $\bar{I}$, the resonator voltage U_0, the number of bunches h in the ring and the beam velocity β in units of the speed of light c. The constant ϵ_0 is the absolute permittivity and γ is the relativistic mass increase, for TSR energies $\gamma \approx 1$. R is the radius of the beam tube and r is the average beam radius, defined by the $2\sigma_{x,y}$ value of the transverse beam width.

From eq. 6.27, eq. 6.28 and eq. 6.29 an equation can be obtained to calculate the average beam intensity $\bar{I}$ from the measured voltage spectrum $\hat{U}_h$ of the pick-up signal. Since $w << 1/f_0$ eq. 6.28 can be Taylor expanded, resulting in an equation to calculate approximately the average beam intensity $\bar{I}$ from the main spectrum amplitude $\hat{U}_1$ at ($h = 1$) RF frequency f_0:

$$\bar{I} = \frac{v \cdot C}{\alpha \cdot L} \frac{\hat{U}_1}{2}. \tag{6.30}$$

Where $\bar{I} \propto v \cdot N$, therefore, $\hat{U}_1 \propto N$.

Continuously linear changing of the revolution frequency, during acceleration or deceleration cycle, will shift the main spectral line $\hat{U}_1$. Therefore, to maintain the spectrum at a constant frequency, it is necessary to mix the fundamental frequency of the pick-up signal with an additional frequency, for instance 2.777 kHz, resulting in $f_m = f_{RF} + 2.777$ kHz. Setup of the experiment is shown in fig. 6.6. Both frequencies f_{RF} and f_m are generated in a DDS[5] card located in the VME crate[6] of the TSR control system. Then, signals at frequencies f_m and f_{RF} are applied to a mixer and it produces new signals at the sum $f_m + f_{RF}$ and difference $f_m - f_{RF}$ of the original signals. By mixing the frequencies the fundamental frequency of the pick-up signal can be shifted to 2.777 kHz during all the measurements.

Fig. 6.7 shows the measured spectrum of pick-up signal mixed to 2.777 kHz during acceleration of the $^{12}C^{6+}$ bunched ion beam with resonator voltage of 232.5 V. In this measurement the 73.3 MeV ion beam is injected at $t_1 = 0$ s, and electron cooled during 1.5 s. Then the electron cooler is switched off and after 0.1 s delay the beam is accelerated for 5 s. The final energy of 240 MeV is achieved at $t_2 = 6.6$ s, and the resonator is switched off. Deviation of the signal profile can be explained by the bunch length change during acceleration. There is no significant beam loss and signal is almost constant, therefore

[5]Direct Digital Synthesis is a precise and stable signal source.
[6]A repository for control cards

$\hat{U}_1 \propto$ N.

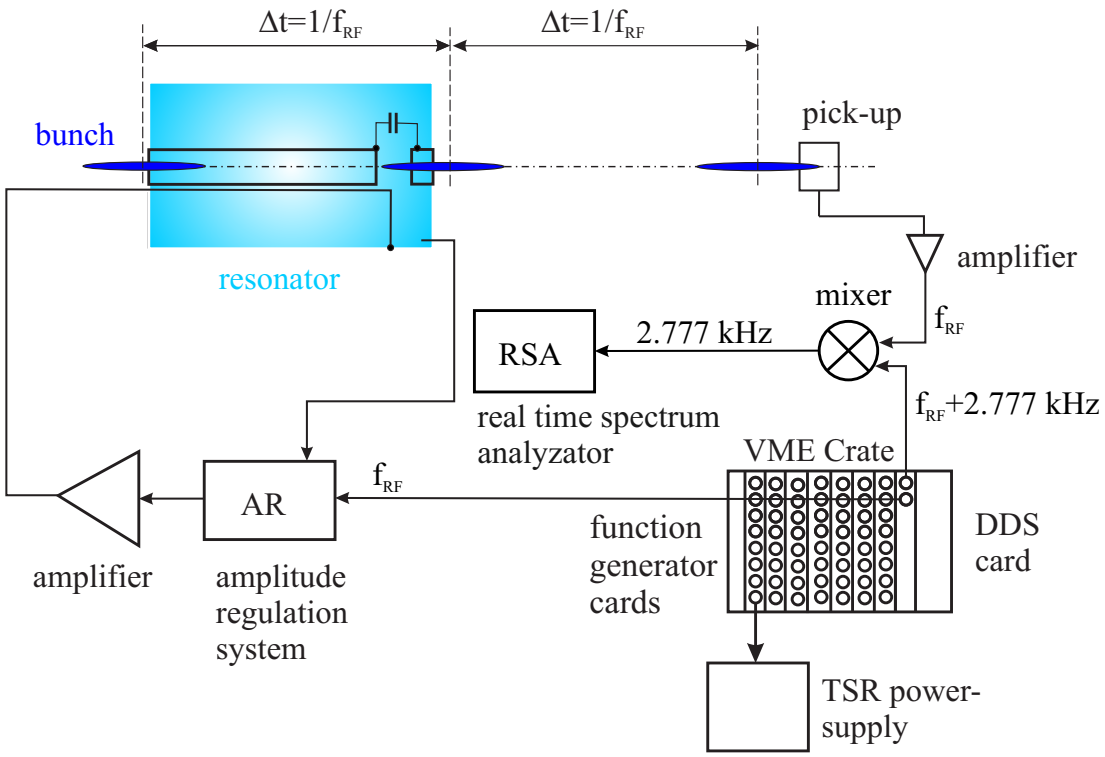

Figure 6.6: Setup for measuring the mixed pick-up spectrum.

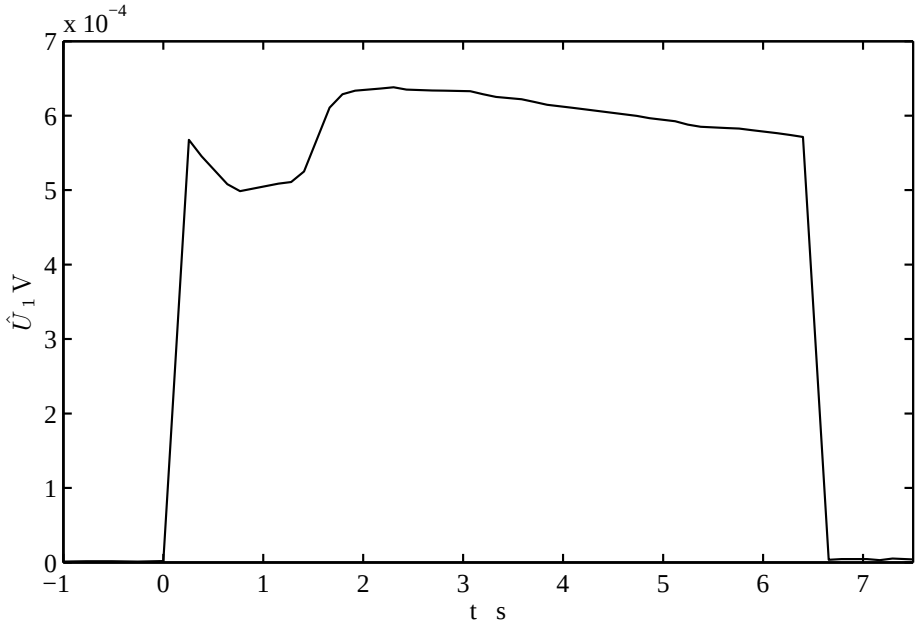

Figure 6.7: Time development of the ion beam spectrum at resonator voltage of 232.5 V, injected at t=0 s.

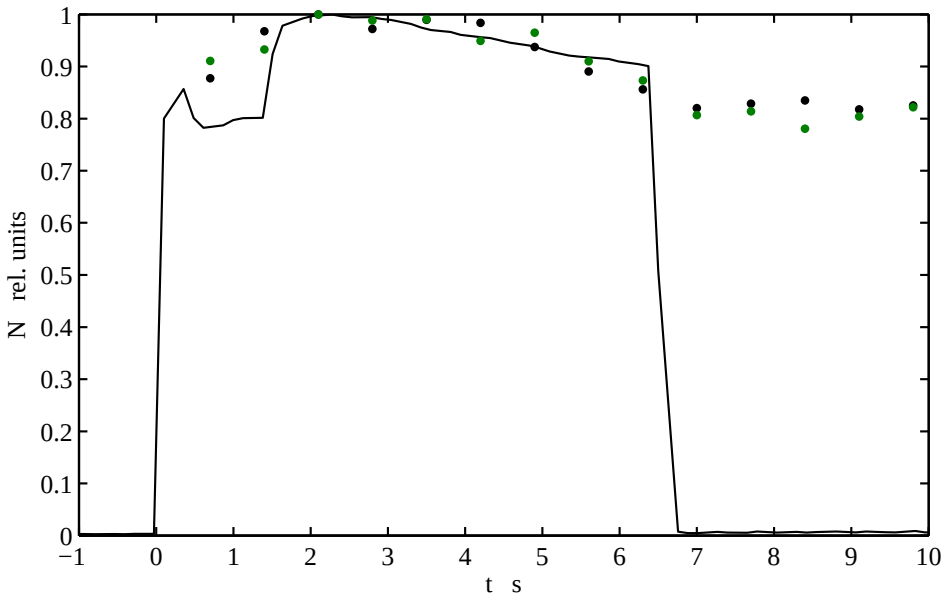

Figure 6.8: Normalized number of particles determined from the mixed signal spectrum at resonator voltage of 232.5 V, as well as from the horizontal (green) and vertical (black) BPM counting rates.

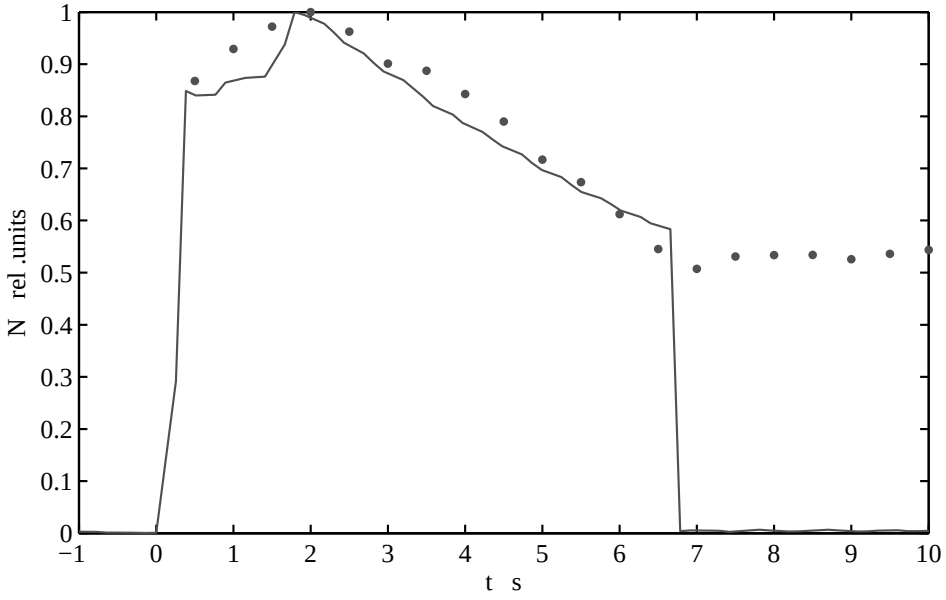

Figure 6.9: Normalized number of particles determined from the mixed signal spectrum at resonator voltage of 139.5 V, as well as from the vertical (grey) BPM counting rates.

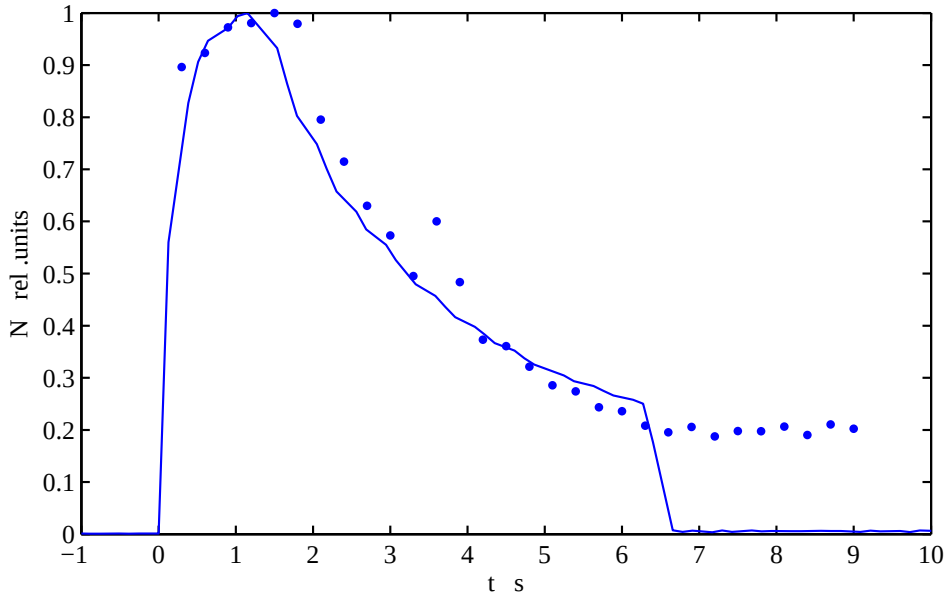

Figure 6.10: Normalized number of particles determined from the mixed signal spectrum at resonator voltage of 46.5 V, as well as from the vertical (blue) BPM counting rates.

The number of particles are determined by using the mixed signal measurements and also, by the counting rates of horizontal and vertical BPM[7], as shown in fig. 6.8-6.10 for different resonator voltages. The resonator voltage should be about 200 V or higher for effective acceleration or deceleration cycle. If it is lower the RF bucket size is small and ions can move out easily due to errors of the magnetic field ramp.

Counting rate calibration of the horizontal and vertical BPM is performed by measuring the dark current and the counting rate of the BPM as a function of ion beam intensity (see appendix E).

6.2 Acceleration of the ion beam

The widely tunable range of the TSR resonator opens up the possibility to accelerate and decelerate ions, which was demonstrated in many experiments. Based on the known functions for the power supply currents and for changing the RF frequency, it is possible to accelerate the beam. To pursue this procedure the setting of the above parameters are almost linearly changed with time from the initial to the final values.

The function of the rigidity-curve for accelerating the $^{12}C^{6+}$ ion beam from the injection energy of 73.3 MeV to 280.156 MeV with a continuous ramp is shown in fig. 6.11. Obviously, the rigidity is almost linearly with time, except a curvature in rigidity function at the starting of the acceleration cycle. It minimizes the deviation between the nominal and actual currents of the power supplies of the magnets, which are currently in use. Also, it prevents a synchronous phase jump, because the synchronous phase scales

[7]Details are in next section.

in non-relativistic approach as $\sin(\phi_s) \propto \frac{dB\rho}{dt}$.

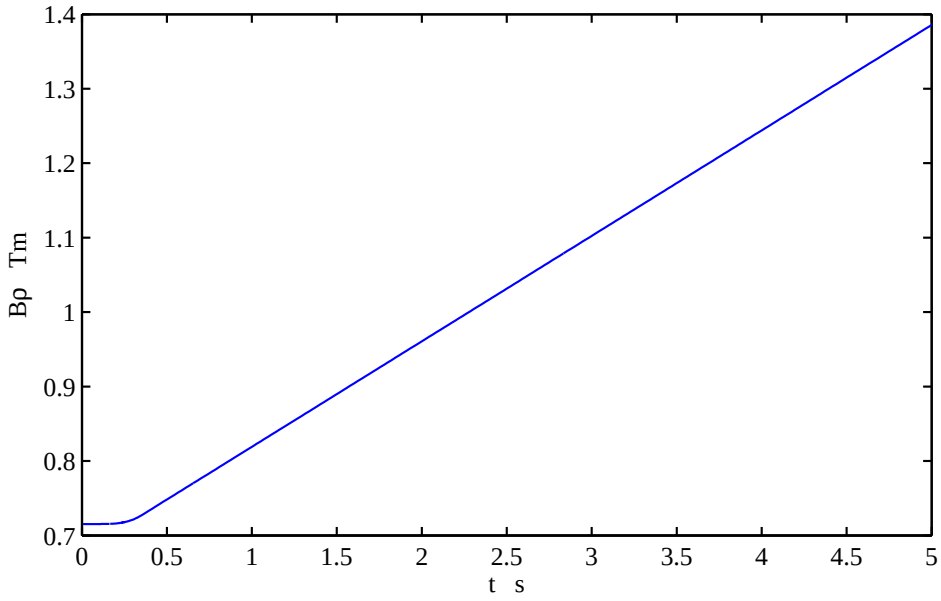

Figure 6.11: Change of the rigidity during acceleration.

After injection the resonator voltage increases linearly during 2 ms, from 0 V to 232.5 V capturing the stored ion beam into the RF buckets, enclosed by the separatrix. Electron pre-cooling can be applied to the ion beam before starting the ramp.

The ramp time is limited by an admissible voltage range of the (KM) correction magnet power supplies, which provide current to the correction windings of the dipoles. The total voltage of the correction windings consists of an induction voltage and a voltage on ohmic resistance. During the ramp cycle, it should be maintained between 0 V to 6 V. The voltage characteristics of the correction windings of the dipole magnets is shown in fig. 6.12. The blue curve refers to the acceleration ramp during 5 s and the green curve is the ramp-back, also takes 5 s. It can be seen that both curves are in admissible voltage range.

The signal of the DC transformer, measuring the ion current is recorded with a "Pico-Scope", as shown in fig. 6.13. A small offset is measured before the injection of the ion beam, which is fitted as dash-dot black line. The dash-dot green line after the injection at t=0 s represent the electron pre-cooling with a duration of 1.5 s. After 0.1 s delay the ramp starts and lasts for 5 s. At t=6.6 s the final energy of the stored ion beam is achieved. According to the increase of the revolution frequency the ion beam intensity increases during acceleration. This intensity increase is shown in time intervals of the graph from t=1.6 s to t=6.6 s. The dash-dot blue line defines the stored ion beam current which is given by:

$$I(f_0) = Q \cdot N \cdot f_0, \tag{6.31}$$

where Q is the total charge of an ion and N is the number of ions. The efficiency of acceleration can be determined by the ratio of the number of particles at final energy to

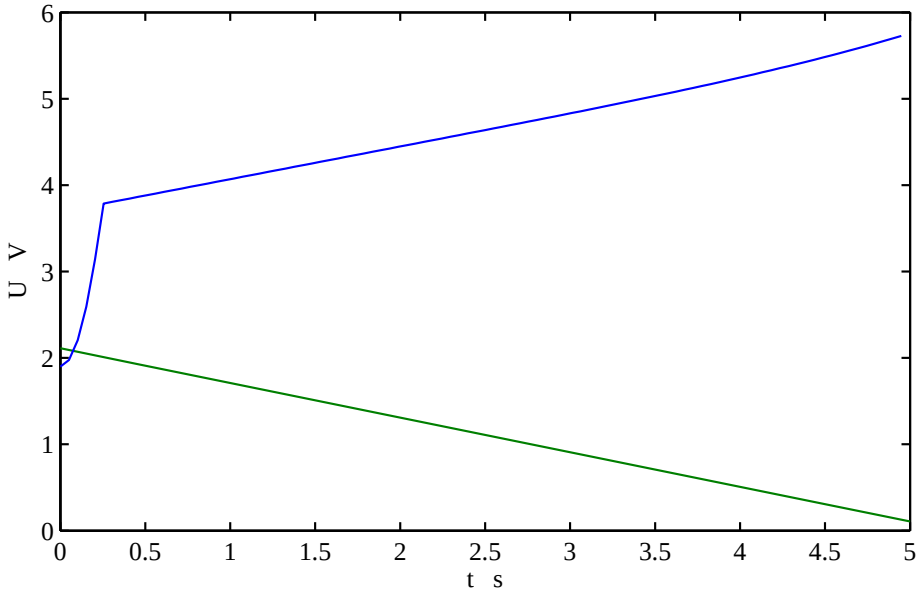

Figure 6.12: Total voltage on the correction windings of the dipole magnet during acceleration.

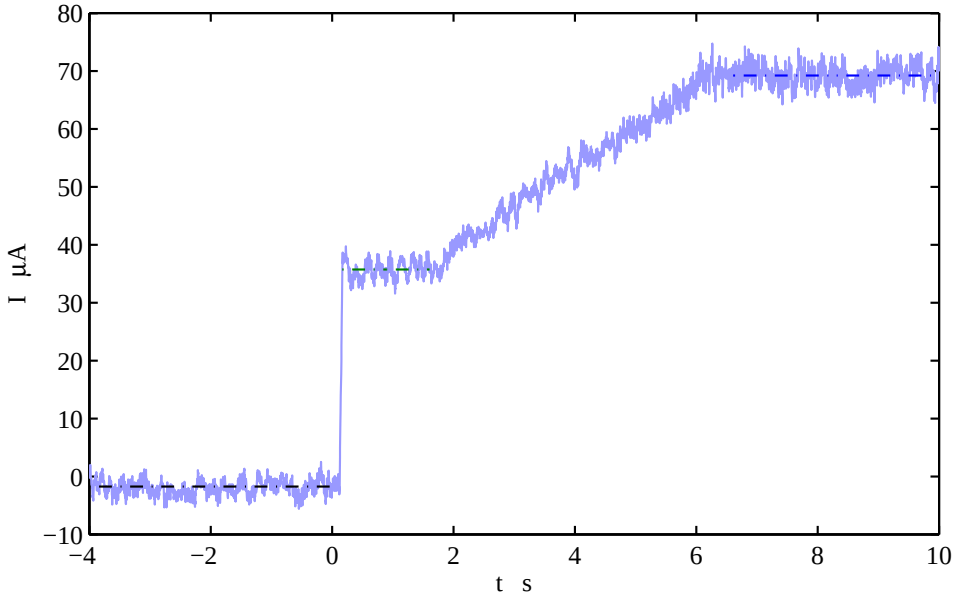

Figure 6.13: Measured ion current during acceleration of the $^{12}C^{6+}$ ion beam from 73.3 MeV to 280.156 MeV at the resonator voltage of 232.5 V.

the initial number:

$$\epsilon = \frac{N_f}{N_0} = \frac{\frac{I_f}{I_0}}{\frac{f_{RF,f}}{f_{RF,0}}}, \tag{6.32}$$

where I_f is current at final energy, I_0 is injected current, $f_{RF,f}$ and $f_{RF,0}$ are final and initial RF frequencies. From the current measurement the ratio $\frac{I_f}{I_0}$=1.894 and from the ramp calculation the ratio $\frac{f_{RF,f}}{f_{RF,0}}$=1.9218 can be calculated. Hence, the acceleration efficiency is:

$$\epsilon = \frac{1.894}{1.9218} = 0.985. \tag{6.33}$$

This means, in the experiment 98% of the injected particles are accelerated to the final energy when electron pre-cooling is applied.

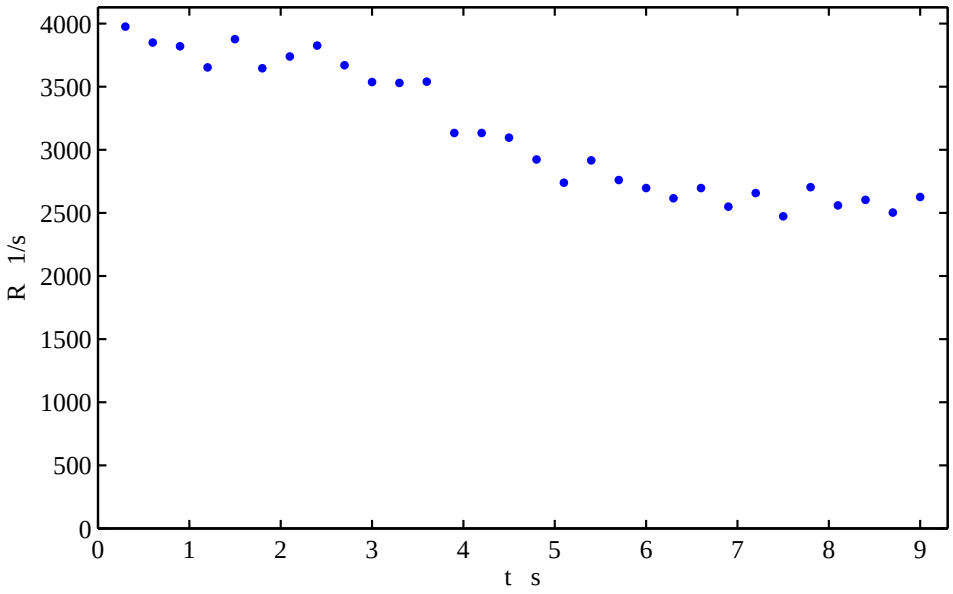

Figure 6.14: Measured counting rate of the horizontal BPM during acceleration at the resonator voltage of 232.5 V. The acceleration ramp cycle starts at t=1.6 s and ends at t=6.6 s.

To assess the number of particles in the storage ring using the ionization rate of the residual gas is an alternative method to determine the intensity of the stored ion beam. The counting rates of the horizontal and vertical BPM during RF acceleration are measured in parallel with the pick-up signal[8]. The counting rate R of the measured horizontal BPM as a function of time is shown in fig. 6.14. If the ionization cross section $\sigma(v)$ of the residual gas is known, the number of stored particles can be calculated from the following

[8]An example of the pick-up signal measurement is shown in previous section, in fig. 6.7. Therefore, the determined number of particles are compared from both methods for different resonator voltages as shown in fig. 6.8, in fig. 6.9 and in fig. 6.10.

equation:

$$R = \eta \cdot \sigma(v) \cdot v \cdot n \cdot N \cdot \epsilon_d, \tag{6.34}$$

where η - the ratio of microchannel plate length of the BPM to the ring circumference, $\sigma(v)$ - the cross section of ionization the residual gas as a function of beam velocity, n - the density of the residual gas and N_0 - the number of ions, ϵ_d - the efficiency[9] of the ion detection. During acceleration the particle loss can be neglected, therefore the number of particles are assumed as constant and the cross section of ionization of the residual gas as the function of revolution frequency can be a useful method to determine the N of particles, because $R \propto f_0 \cdot \sigma(f_0) \cdot N$. The calculated cross section for ionization of

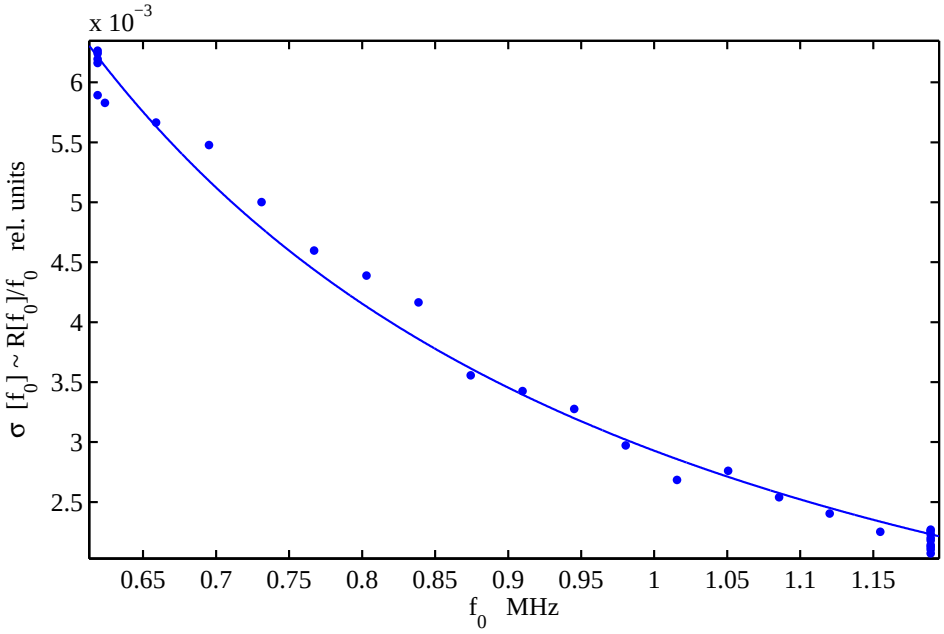

Figure 6.15: Relative cross section of residual gas ionization as a function of the revolution frequency. The counting rate is measured using the horizontal BPM. Blue markers are the values of the calculated data and blue solid line is a fit to the data.

the residual gas as a function of the revolution frequency is shown in fig. 6.15. The fit function to determine the relative ionization cross section is given by:

$$\sigma(f_0) = \frac{A}{f_0^{\alpha}}, \tag{6.35}$$

where A is a constant, which depends on the composition, concentration of the residual gas and charge of the ions. From the measured horizontal and vertical counting rates the fit parameters $A_x = 0.02928$, $\alpha_x = 1.568$, $A_y = 0.005527$, $\alpha_y = 1.604$ are obtained. Therefore, the residual gas ionization cross section for $^{12}C^{6+}$ ions in the velocity range of (0.11 - 0.22)·c[10] scales as $\sigma_v \propto \frac{1}{v^{\alpha}}$. The exponent α is known, so the relative number of

[9] $\epsilon_d \approx 1$

[10] Speed of light.

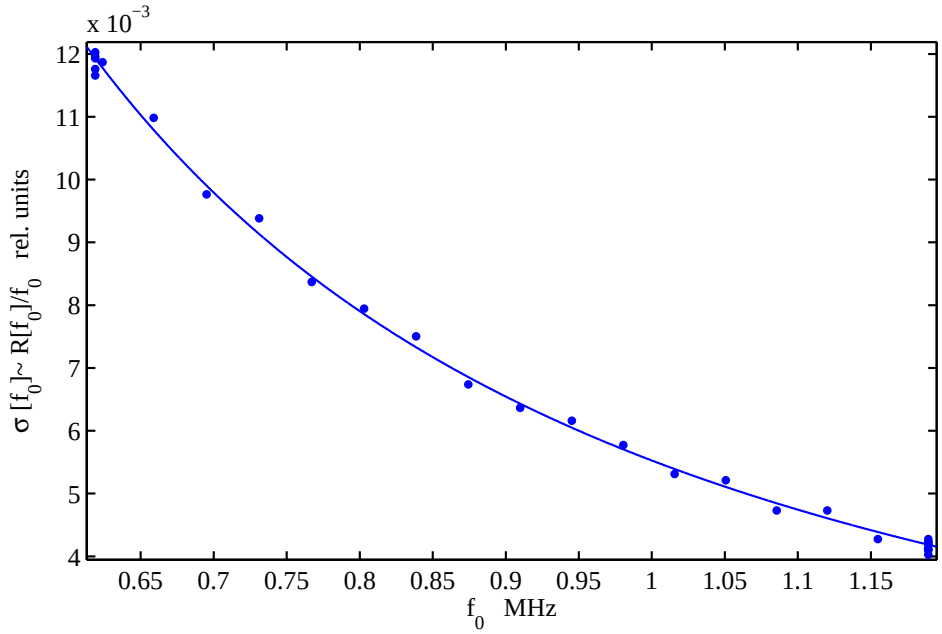

Figure 6.16: Relative cross section of the residual gas ionization as a function of the revolution frequency. The counting rate is measured using the vertical BPM. Blue markers are the values of the calculated data and blue solid line is a fit to the data.

particles can be calculated:

$$N \propto R f_0^{\alpha-1}. \tag{6.36}$$

6.2.1 The beam width during acceleration

Under the influence of linear forces by quadrupoles the trajectory of a particle in the phase space[11] follows an elliptical path. Each particle is defined by its position (x, y, z) and momentum (p_x, p_y, p_z). For a fixed time, each particle occupies a certain point in the phase space, described by six coordinates (x, y, z, p_x, p_y, p_z). Therefore, a group of $10^6 - 10^{10}$ particles, the beam, can be explained with a closed curve which includes the (x, y, z) and (p_x, p_y, p_z) coordinates of every particle. Due to the large number of particles a statistical variable represents the beam and its size, so called an emittance which is defined by the area of the ellipse. The equation of the ellipse is given by:

$$\gamma r^2 + 2 \cdot \alpha r p + \beta p^2 = \varepsilon, \tag{6.37}$$

where ε is the single-particle emittance, α, β γ are the twiss parameters, $\beta\gamma - \alpha^2$=1. Fig. 6.17 shows the single-particle emittance[12] viewed at fixed azimuthal position s and time. Particles with different amplitude lie on the different concentric ellipses. Large ellipse represents the particle with larger amplitude and different initial phases which are

[11] The phase space of non-interacting particles is an abstract space having a dimensionality of six. The state of a system is represented by a system point whose components are vectors of the particles.
[12] Also called Courant-Snyder invariant.

shown as δ the numbered black dots. The phase space trajectory of the particle with smaller amplitude is shown as a small ellipse. The area in the phase subspace is defined

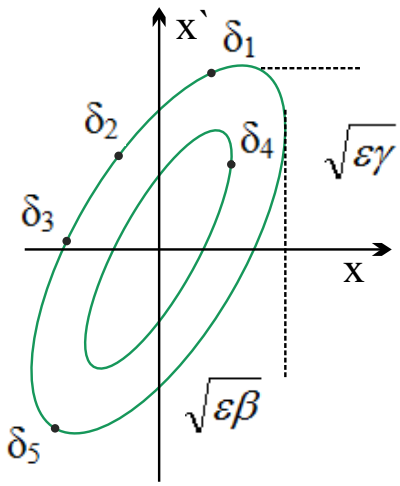

Figure 6.17: Single-particle emittance.

as $S_x = \int\int \mathrm{d}p_x\,\mathrm{d}x$ and the definition is analogous for the vertical S_y and the longitudinal S_z phase subspaces. If the particle motions in the three dimensions are independent of each other, the projections of the phase space in the three planes are uncorrelated. For independent motions the phase space volume in the entire six dimensional phase space is given by:

$$S = S_x S_y S_z. \tag{6.38}$$

The shape and position of this area changes as the motion proceeds and each particle follows its own trajectory. But the area S is conserved. This is called Liouville's theorem, states that in conservative fields[13] and without particle interaction, the phase space density, and in particular the phase space volume of the ensemble of particles, is conserved. Instead of the momentum a small angle of the particle orbit with the beam axis, so called divergence is convenient to use:

$$x' = \frac{dx}{ds} = \frac{\dot{x}}{\dot{s}} \approx \frac{p_x}{p_0}, \tag{6.39}$$

where x is displacement, p_0 is longitudinal momentum and accordingly for $y' = p_y/p_0$, $z' = p_z/p_0$. The horizontal phase subspace volume and the horizontal emittance are related through:

$$S_x = \int\int \mathrm{d}x\mathrm{d}p_x = p_0 \int\int \mathrm{d}x\mathrm{d}x' = \pi p_0 \varepsilon_x, \tag{6.40}$$

[13]In contrast, this may not be true for time-dependent fields.

and analogous for ε_y and ε_z. The Liouville theorem postulates that, for constant longitudinal momentum:

$$\int\int \mathrm{d}x'\mathrm{d}x = \varepsilon_x \pi = constant, \tag{6.41}$$

in case of acceleration the phase space $\int\int \mathrm{d}p_x \mathrm{d}x = p_0 \int\int \mathrm{d}x'\mathrm{d}x = constant$, therefore, $p_0\varepsilon = constant$. Corollary to the Liouville theorem a normalized emittance[14] $\varepsilon_n = \gamma\beta\varepsilon$ can be defined and as acceleration proceeds the normalized emittance is conserved.

To demonstrate the corollary to the Liouville theorem, experiments are conducted with the $^{32}S^{12+}$ ion beam. To neglect the interaction of the particles in the beam, in the experiment no electron pre-cooling is applied. Then the beam is accelerated from 56.34 MeV to 216.3 MeV, which in corresponding RF frequency interval from 3.325 MHz to 6.487 MHz. The horizontal beam width is measured with the horizontal BPM, as shown in fig. 6.18, after acceleration at t=6 s the final energy is achieved and electron cooling is applied. It is obvious from the rapid reduction of the beam width at t=6 s. The beam

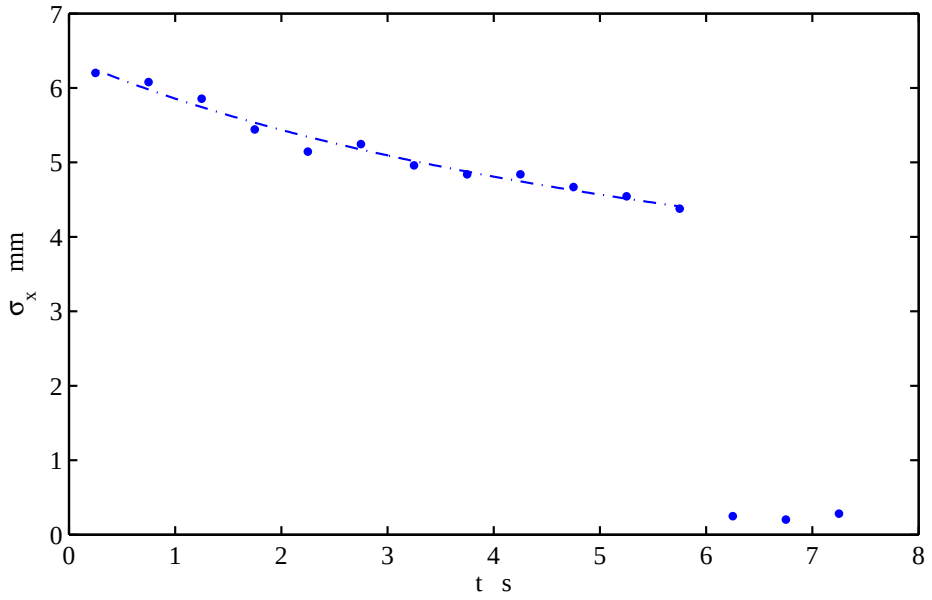

Figure 6.18: Evolution of the horizontal beam width during acceleration of the $^{32}S^{12+}$ ion beam without pre-cooling. Blue markers are the measured data and dash-dot line is a fit to the data. After 6 s at the final energy electron cooling is applied.

width scales as $\sigma \propto \sqrt{\varepsilon}$, under acceleration in addition, it scales with the longitudinal momentum as $\sigma \propto \frac{1}{\sqrt{p_0}}$. Therefore, the beam profile can be fitted with the following equation:

$$\sigma = \frac{a}{\sqrt{f_{RF}}}, \tag{6.42}$$

[14]It is independent of the particle momentum.

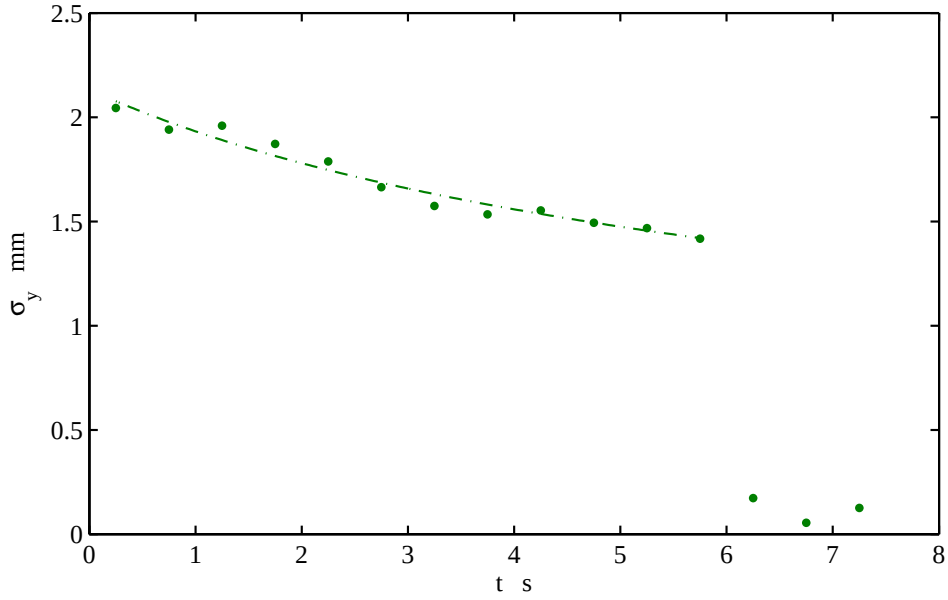

Figure 6.19: Evolution of the vertical beam width during acceleration of the $^{32}S^{12+}$ ion beam without pre-cooling. Green markers are the measured data and dash-dot line is a fit to the data. After 6 s at the final energy electron cooling is applied.

where a is constant which is given by the initial beam width and f_{RF} is the RF frequency. Fig. 6.19 shows the vertical beam profile during acceleration measured using the vertical BPM it explains the evolution of the profile in the vertical case. Eq. 6.42 is only valid for acceleration or deceleration of the beam if the interaction between the particles can be neglected. If the beam is cooled and the density is high enough, IBS must be taken into account.

Therefore, experiments are conducted with the $^{12}C^{6+}$ ion beam applying electron pre-cooling before starting the acceleration ramp. Due to electron pre-cooling the ion beam density is high and IBS will be strong. As shown in fig. 6.20, the horizontal beam profile measured with the BPM, includes the equilibrium state followed by IBS expansion at the start of the acceleration ramp and at t=1 s where the electron cooler is switched off. It can be seen that, the emittance of the beam shrinks partly, during the acceleration process, where the IBS influence is negligible. The vertical beam profile development with electron pre-cooling is also shown in fig. 6.21. Eq. 6.42 is fitted to the both data, partly.

Summarizing the experiments with and without electron pre-cooling, the adiabatic damping of the beam width under acceleration is demonstrated. When the beam is accelerated, its longitudinal momentum increases but transverse momentum remains the same. Hence the beam divergence decreases. Accelerating the beam leads to a reduction of the volume occupied in phase space. Therefore, the normalized emittance of the beam is conserved under acceleration. Normalized emittance is the volume of phase space occupied by the beam multiplied by the relativistic γ. The actual volume of phase space occupied by the beam is the (geometrical) emittance.

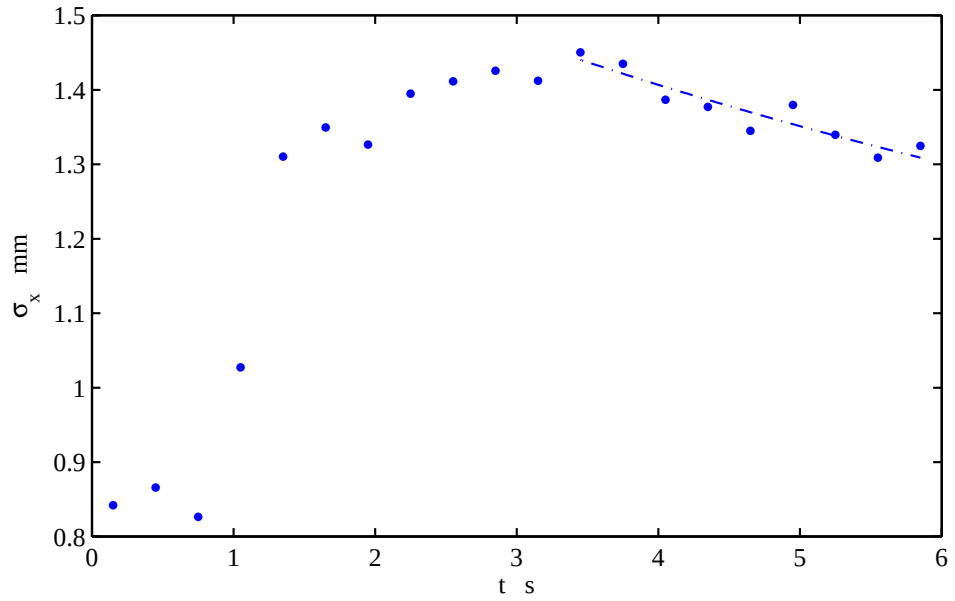

Figure 6.20: Development of the horizontal beam width during acceleration of the $^{12}C^{6+}$ ion beam with electron pre-cooling.

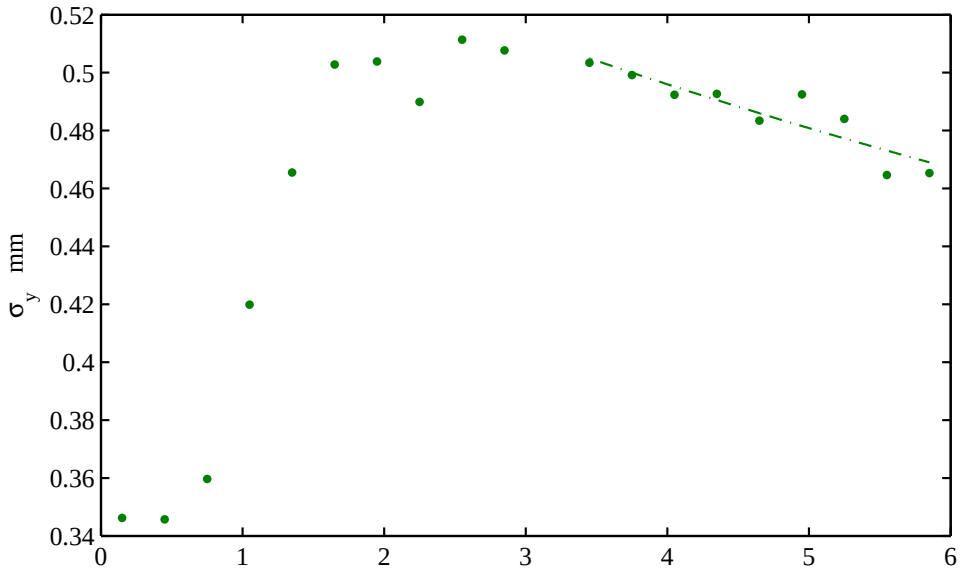

Figure 6.21: Development of the vertical beam width during acceleration of the $^{12}C^{6+}$ ion beam with electron pre-cooling.

6.3 Deceleration in the storage ring

To understand the beam dynamics in the deceleration cycle, experiments are performed using $^{12}C^{6+}$ ions, which are decelerated from 73.3 MeV to 9.77 MeV (1 MeV/u). The reduction of the beam energy by a factor of > 7, corresponds to the rigidity decrease from 0.71 Tm to 0.26 Tm, as shown in fig. 6.22. The beam is bunched at the resonator voltage of 232.5 V and electron pre-cooled for 4 s before starting the deceleration ramp. Electron cooling provides small beam emittances and momentum spread which is beneficial for efficient deceleration. After switching off the cooler the ion beam is decelerated by synchronous ramping of the ring magnets and the frequency of the RF system. The calculated frequency-curve for the deceleration ramp of 7 s is shown in fig. 6.23.

Unlike to the acceleration process, four dipoles in the injection section of the TSR, are also employed in the ramping cycle. These dipoles produce a bump[15], which is a horizontal beam-offset in the direction of the electrostatic septum. They are not laminated, therefore eddy current will occur if the magnetic field changes. If no ramping applies to these dipoles a closed orbit shifts toward the septum and the beam will collide with the septum foil causing a total beam loss.

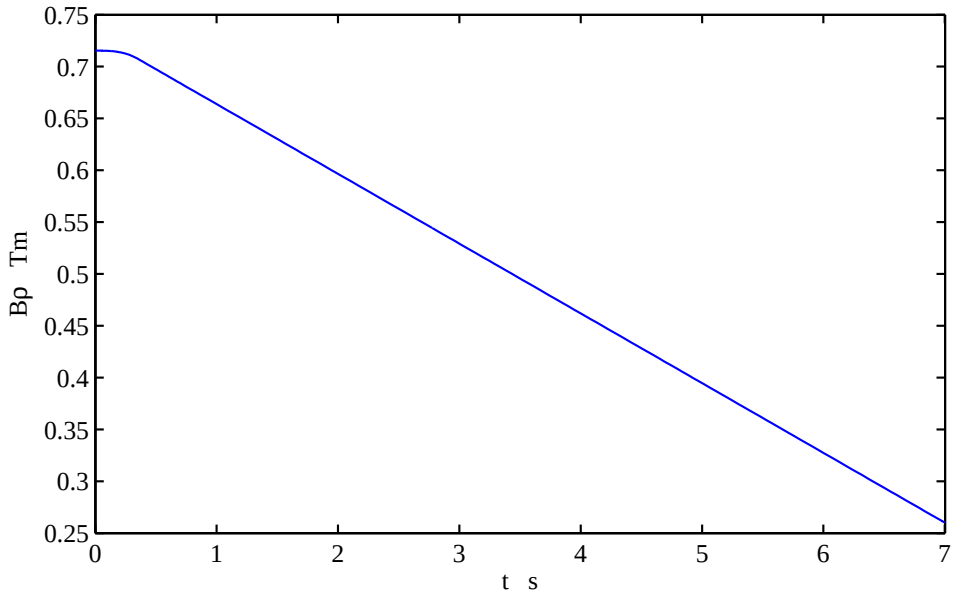

Figure 6.22: Beam rigidity as a function of time during the deceleration cycle.

The voltage characteristics of the correction windings of the dipole magnets during the deceleration ramp is shown in fig. 6.23. The blue curve refers to the deceleration ramp during 7 s and the green curve is the ramp-back, which takes 5 s. It can be seen that both curves are in the admissible voltage range. Ramping of the magnetic fields is accomplished by employing the DAC cards and the DSP driven card to generate the RF frequency.

[15] A localized orbit displacement created by vertical or horizontal correction element dipoles used to steer the beam through the available aperture or around obstacles.

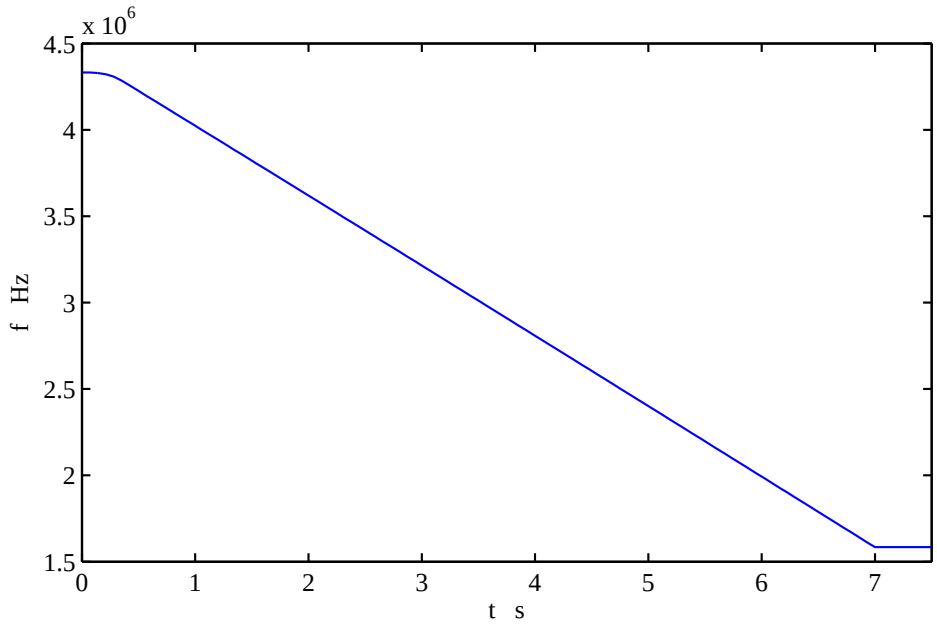

Figure 6.23: Calculated RF frequency for the deceleration cycle.

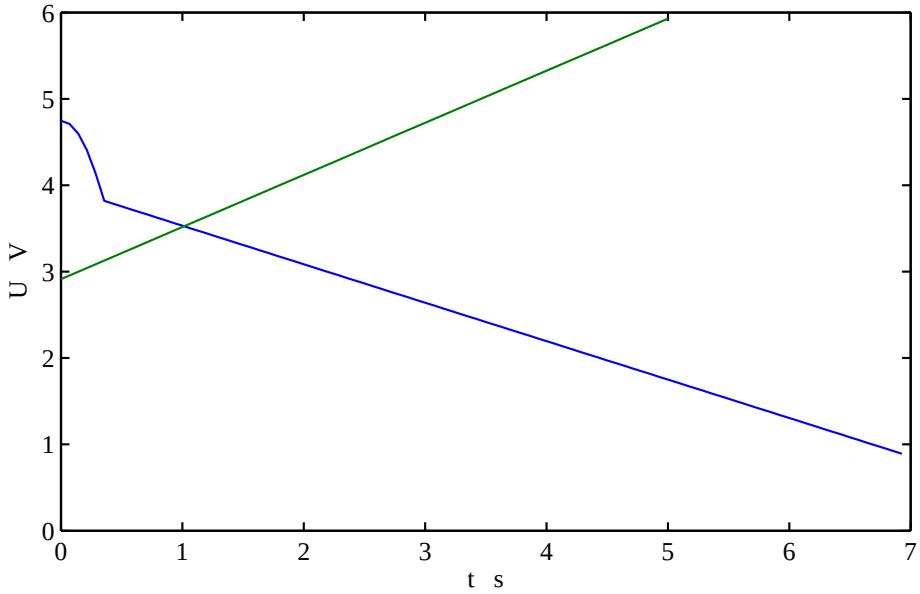

Figure 6.24: Total voltage on the correction windings of the dipole magnet during the deceleration cycle.

When the final energy is achieved simultaneously, electron cooling is applied and the RF voltage is switched off, so that the ion beam can be debunched.

Current measurements are performed by measuring the pick-up signals, as discussed in the previous section.

To evaluate the beam quality IBS measurements are conducted at the final energy. At the final energy the lifetime of the beam is measured.

6.3.1 The beam profile development

To investigate the velocity dependence of IBS with the simplified model the following ansatz for the heating term is introduced:

$$D_i(t) = \frac{\tilde{D}_i}{\beta^{\kappa}(t)}, \tag{6.43}$$

where κ=3 (see eq. 5.5). In the deceleration cycle the ion velocity is changed linearly:

$$\beta(t) = \beta_0 + \alpha t, \tag{6.44}$$

where β_0 is the initial velocity of ions. The parameter α can be determined as follows:

$$\alpha = (\beta_f - \beta_0)/T, \tag{6.45}$$

where T is ramping time and β_f is the final velocity of ions. To assess the beam width during deceleration the eq. 5.6 can be solved with eq. 6.43 and eq. 6.44:

$$\sigma_i(t) = \left(\sigma_{i,0}^{\gamma} + \frac{\gamma \tilde{D}_i \left(\beta_0^{1-\kappa} - (\beta_0 + \alpha t)^{1-\kappa} \right)}{\alpha(\kappa - 1)} \right)^{\frac{1}{\gamma}}. \tag{6.46}$$

In fig. 6.25, the experimental and computed horizontal beam width during deceleration is shown as a function of time. While injection of the $^{12}C^{6+}$ ion beam electron pre-cooling is applied simultaneously, resulting in an initial horizontal beam width of $\sigma_x = 1$ mm. The beam is cooled for 4 s and at t=4 s the electron cooler is switched off and the ion beam is decelerated during 7 s to the final energy of 9.7 MeV. Achieving the final energy at t=11 s, electron cooling is applied again, yielding in fast reduction of the horizontal beam width σ_x. Because the IBS heating term D_i is higher at the final energy, the equilibrium beam width at 9.7 MeV is slightly larger as compared to the initial one.

The computed σ_x from eq. 6.46 for κ=3 is shown as a dash-dot blue line, and the measured σ_x is shown as blue-colored markers. In this calculation the heating term $\tilde{D}_i$ and the parameter γ belong to the IBS measurement obtained at the initial energy of 73.3 MeV (see chapter 5). Obviously, the computed σ_x values do not match the measured beam profile, especially at low velocities. Therefore, a new term is added to eq. 6.46 according to Liouville's theorem. The theorem postulates that, the phase space area occupied by non-interacting particles is conserved[16] during deceleration. Accordingly, in

[16]See section 6.2

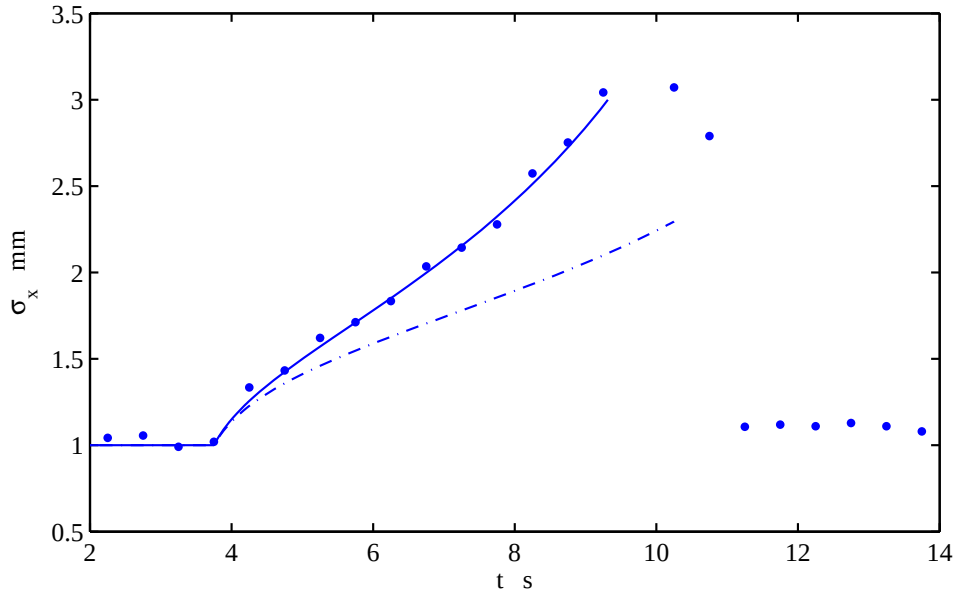

Figure 6.25: Measured and computed beam width σ_x of the $^{12}C^{6+}$ ion beam as a function of time under deceleration. The injected number of particles is $1.065 \cdot 10^8$.

the non-relativistic approach, the change of the ion beam size σ_i is given by:

$$\sigma_i(t) = \tilde{\sigma}_i \sqrt{\frac{\beta_0}{\beta(t)}}, \tag{6.47}$$

where $\beta(t)$ is the ion velocity at the time t and $\tilde{\sigma}_i$ is the beam width at t=0 s. It is a boundary value for $\tilde{D}_i \to 0$ of the eq. 6.46. To consider IBS, $\tilde{\sigma}_i$ in eq. 6.47 will be replaced by the beam width $\sigma_i(t)$ in eq. (6.46):

$$\sigma_i(t) = \left(\sigma_{i,0}^{\gamma} + \frac{\gamma \tilde{D}_i \left(\beta_0^{1-\kappa} - \beta(t)^{1-\kappa} \right)}{\alpha(\kappa - 1)} \right)^{\frac{1}{\gamma}} \sqrt{\frac{\beta_0}{\beta(t)}}. \tag{6.48}$$

According to eq. 6.48, the beam width during deceleration is computed, where the IBS heating term $\tilde{D}_i$ and γ are determined from the measurements at the injection energy of 73.3 MeV. The result is shown in the above graph as a solid-blue line. The equilibrium beam width σ_{x_0} is obtained from the measured beam width between t=2-4 s. It is demonstrated that, the calculation of the beam width during deceleration using only IBS data, measured at the injection energy, is well consistent with the observation.

In contrast to acceleration, the beam width under deceleration adiabatically expands. The longitudinal momentum decreases while transverse components are constant[17], therefore the divergence and beam size increases.

[17] If IBS can be neglected.

6.3.2 Deceleration efficiency

Unlike acceleration beam dynamic effects during deceleration are more adverse with respect to losses. To evaluate the ion loss during the deceleration cycle, in which two cooling steps are applied, the number of ions is determined by measuring the voltage on the capacitive pick-up. The integral of this pick-up signal over one RF period is proportional to the number of ions in the bunch. Therefore, the pick-up signal area is assessed for different intensities as a function of time, which is shown in fig. 6.26. During measure-

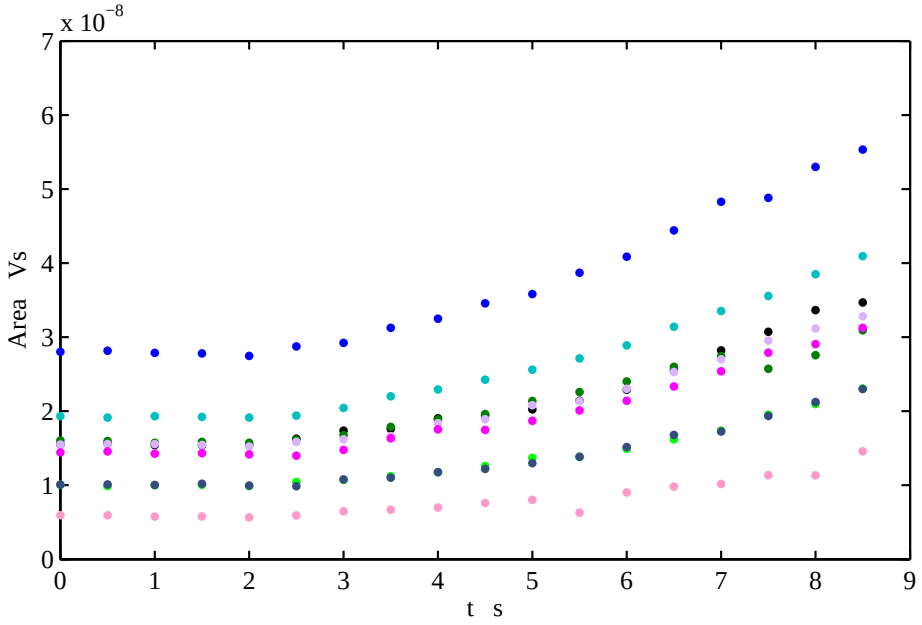

Figure 6.26: Pick-up signal area measured during the deceleration ramp cycle. The ramp starts at t=2 s and lasts for 7 s. The final energy is achieved at t=9 s. Different colors represent different intensities.

ments the data is recorded every 0.5 s which started at t=0 s, 2 s later after injection. At the end of the ramp at t=9 s the RF resonator voltage is switched off; therefore the ion bunch is debunched so that the signal can not be detected by pick-up at $t \geq$9 s. The injected ion beam, at different intensities, is electron cooled for 4 s. When the beam is cooled, the measured pick-up signal area is constant. While decelerating the beam from t=2 s to t=9 s the electron cooler must be switched off. Hence the signal area increases because it scales with the beam velocity inversely. The calculated numbers of particles, as a function of time, determined from the pick-up signal area are shown in fig. 6.27. As shown in fig. 6.28, the ratio of the number of particles $N(t)$ during the deceleration cycle and the number of particles N_0 of the injected beam defines the deceleration efficiency. It can be seen that, during deceleration in the last 2 seconds the particle loss increases. The last 2 seconds of deceleration reveals an instability causing particle losses, which is also indicated in the previous graph (see fig. 6.27). The reason can be explained by the instability of the main dipole power supply. To verify the source of this instability power supply response during the deceleration ramp is measured. Fig. 6.29 shows the measured deviation of the power supply current under the deceleration ramp. $\Delta I = I_a - I_n$

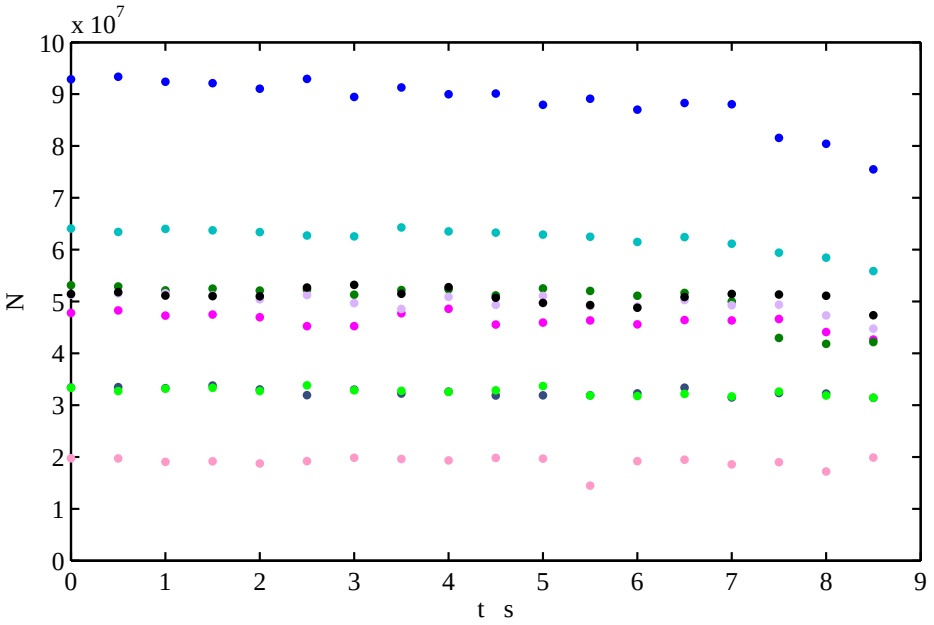

Figure 6.27: Measured number of particles as a function of time during deceleration.

is a deviation between actual I_a and nominal I_n current values, leading to a large closed orbit shift resulting in particle losses. The constant dash-dot cyan line represents an ideal current flow with ramp time. It can be seen that, starting the ramp at t=2 s shows slight deviation. It deteriorates from t=5 s and reaches the maximum at t=8.9 s which is $\Delta I/I$=1%. By current deviation $\Delta I/I$ magnetic field deviation $\Delta B/B$ is created. As discussed in the chapter 3 the magnetic field change by $\Delta B/B$ leads to a closed orbit shift as the momentum change of ions by $\Delta p/p$ does. A similar situation arises when $\Delta B/B$ occurs due to current deviation and a closed orbit shift of about Δx[18]=3 cm can cause beam losses. The calculated nominal current for the ramp cycle is shown in fig. 6.30.

Deceleration efficiency as a function of intensities is shown in fig. 6.31. It indicates that, the beams containing a small number of particles ($N \leq 10^8$) can be decelerated with an efficiency of 90%.

[18]Here, a maximum dispersion (D=3 m) is considered to calculate the closed orbit shift.

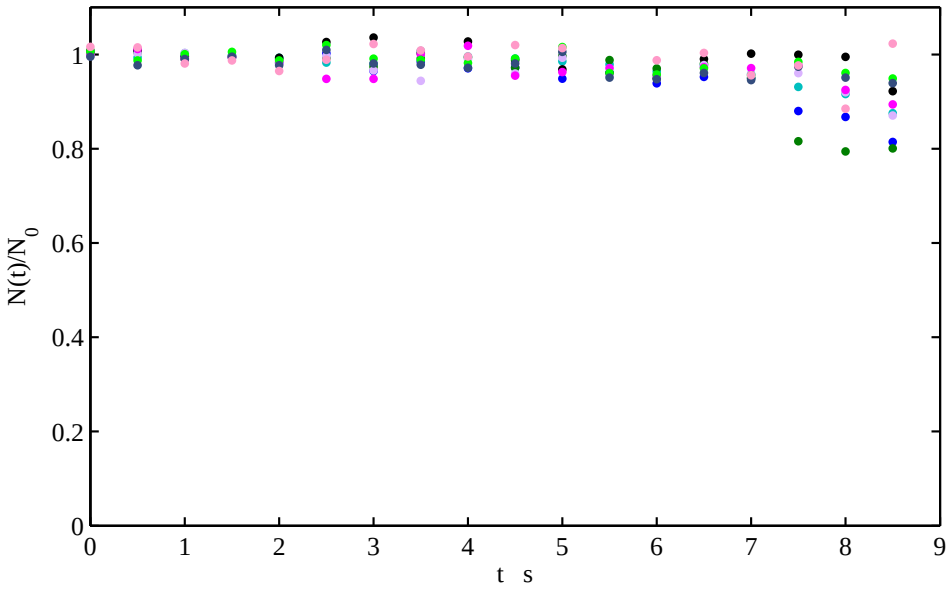

Figure 6.28: Normalized number of particles as a function of time during deceleration.

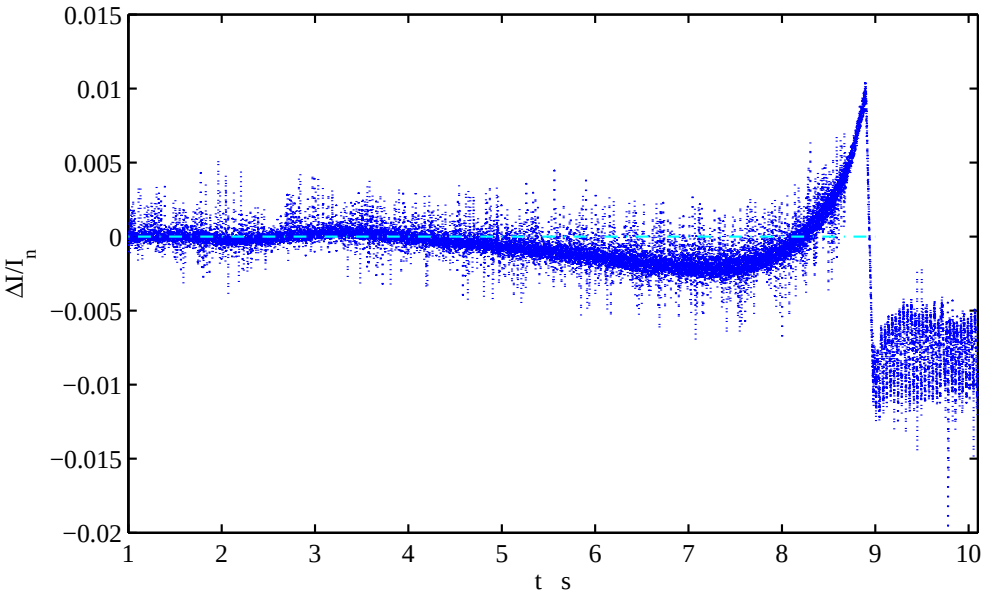

Figure 6.29: Deviation $\Delta I=(I_a - I_n)/I_n$ of the actual current of power supply I_a to the nominal current I_n during deceleration.

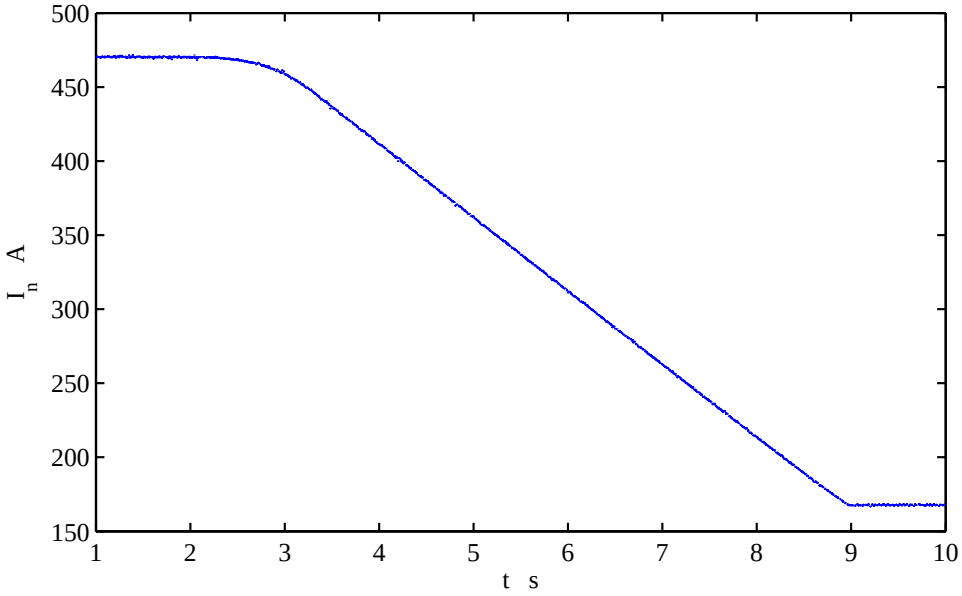

Figure 6.30: Nominal current for the ramp cycle.

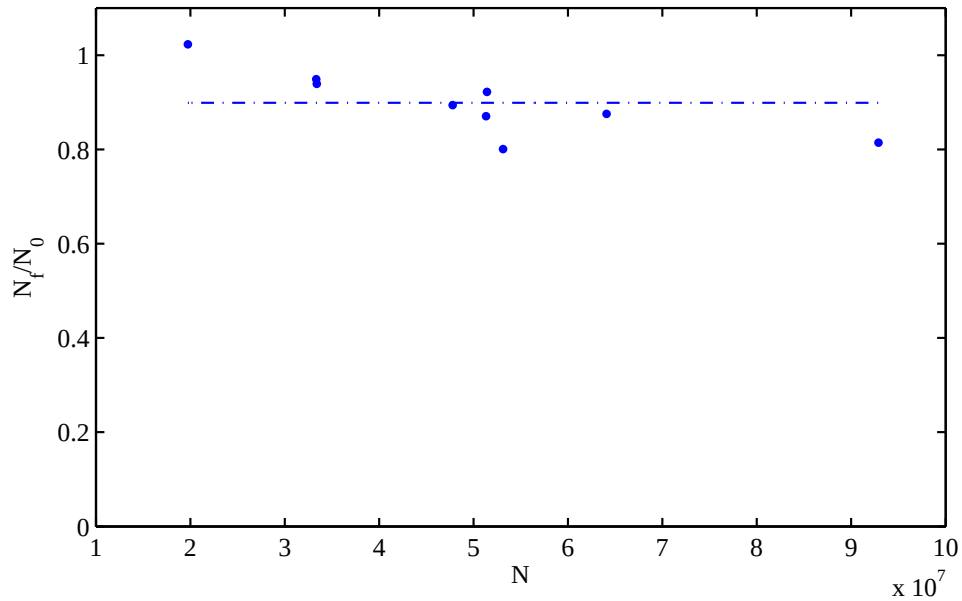

Figure 6.31: Deceleration efficiency as a function of the injected number of particles at 73.3 MeV.

6.3.3 Control system of the TSR and electron cooler

An overview of the TSR control system is shown in fig. 6.32. The important elements of the system are characterized below[40]. A VME crate contains function generator cards which consist of eight analog output channels with 16 bit resolution. All output channels are optically isolated. They had been designed and constructed at MPIK. Each function generator card has a signal processor ADSP2181 on board and it is used for programming the functions for acceleration and deceleration. The temperature drifts of the cards are below than 1 ppm/°C.

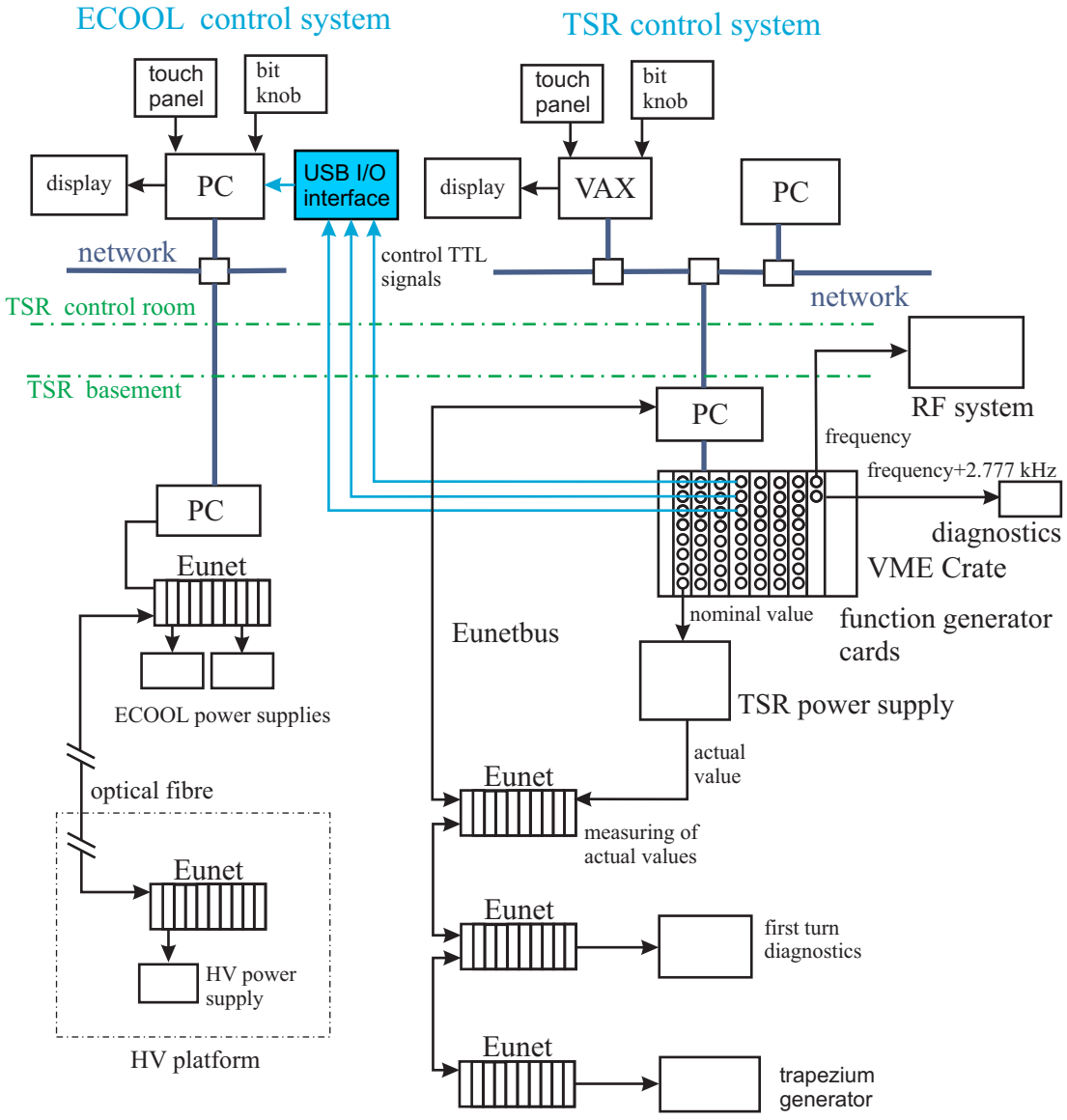

Figure 6.32: Schematics of the control system of the TSR.

Two channel synthesizer VME-DDS cards are also included in the VME crate, which generate the frequency f_{RF} of the RF system as well as a signal with a frequency of f_{RF}+2.777 kHz used for intensity measurements (see chapter 6.1). The frequency f_{RF} can be set in the range between 0 and 10 MHz with an interval of 0.023 Hz.

The database of the TSR control system is located in a VAX computer. The VAX and the VME crates, with the function generator cards, are connected via a network. Touch panels as well as bit knobs are used for the data input.

Eunet is a bus system, developed at MPIK, used to control and readout of power supplies. For this purpose DAC and ADC modules with a resolution up to 16 bit are provided. Digital output modules in the Eunet crates are utilized to control the quartz drives for the first turn diagnostics. Special designed opto-converter modules in the Eunet crates allow the control of power supplies located at the high voltage platform of the electron cooler.

In the deceleration process several cooling steps may be required, that means, the electron cooler has to change the settings during the ramp cycle. Therefore, the control system of the electron cooler is upgraded to enable its operation at different settings. An USB I/O card as shown with a blue frame (see fig. 6.32), is installed to the ECOOL user interface computer. It contains the database of the electron cooler settings. In addition, three control cables connect the I/O card with three function generators of the TSR control system. These function generators create TTL signals. If one of the three control signals change its value the ECOOL computer will load a new data base. The number of the new database is given by the values of the three control signals. The availability of the three digital control signals can provide eight different databases of the electron cooler to load during one deceleration cycle.

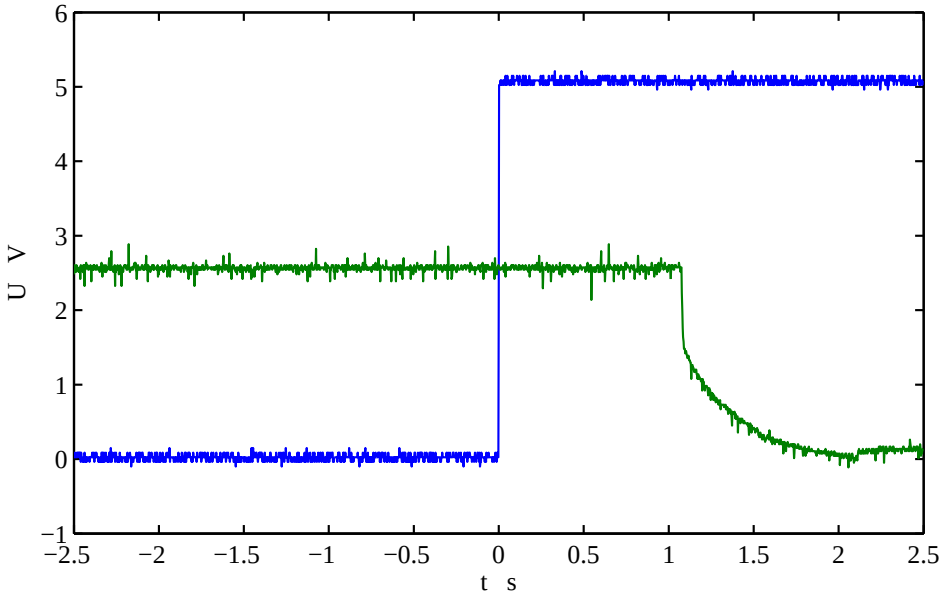

Figure 6.33: Database control signal (blue) and the current of cathode power supply (green).

The essential time for changing the database is determined by measuring the current of the cathode power supply and the signal from one of the three data base control lines. The measurement is shown in fig. 6.33, where the blue curve is the control signal and the green curve is the current of the cathode power supply. At t=0 s the control signal change

its value from 0 V to 5 V. About 1 s later at t=1, the current of the cathode power supply changes due to the new data base containing a different cathode potential. The response time of the high voltage cathode power supply is additional 0.6 s to change the cathode potential to the new value. During the deceleration cycle the database is changed while the electron cooler is switched off. The deceleration ramp time is always longer than 2 s, therefore the delay time of the database changes and the response of cathode power supply will not pose a problem.

7 Conclusions and an outlook

Recently producing high-intensity, low-energy multicharged ion beams has become important because of certain progress and needs in atomic and molecular collision experiments. It is accomplished by deceleration of ions in the cooler storage ring. To understand the deceleration cycle, experiments are performed with $^{12}C^{6+}$ ions, which in beam energy is reduced from 73.3 MeV to 9.77 MeV. The primary goal of these experiments and their detailed analysis is to explore the behavior and evolution of the ions during deceleration.

However there are also technical limitations in achieving the lower energies. For example, some of the ring magnet power supplies, which are used for closed-orbit corrections are not known well enough for fast ramping. This can be overcome by replacing each of them with an adequate power supply. At present, inappropriate power supplies for the correction coils of the main dipole magnets[1] rule out magnetic bending fields for deceleration. In the deceleration cycle, when the magnetic bending fields are lower than 0.22 T, there are control deviations in the main power supply of the TSR. But improving the current regulation system of the power supply can reduce the deviations.

Under these limitations, the $^{12}C^{6+}$ ions are decelerated from 73.3 MeV to the lowest-possible minimum energy of 9.77 MeV with 90 % efficiency. Two cooling steps applied at initial and final energies and also the lifetimes of the ion beam are measured. The results are in good agreement with the calculated beam lifetimes due to residual gas interactions, mainly electron capture and multiple scattering processes.

To apply manifold cooling steps the control systems of the electron cooler and the TSR has been upgraded. With this modification, three additional control signals can be generated in the function generators of the TSR control system and directed to the electron cooler control system.

For $N \leq 10^8$ number of ions deceleration experiments show that the efficiency has no significant dependency on the injected ion-beam intensity. The maximum intensity of any stored ion beams in the TSR can be calculated from a semi-empirical equation (4.24) explained in chapter 4. The calculations are consistent with the experiments conducted in the TSR for different ion species. The number of $^{12}C^{6+}$ ions during deceleration is below the space-charge limit, therefore incoherent tune shift is not relevant in the deceleration cycle.

Due to deceleration the final beam current decreases and becomes immeasurable using common techniques. Therefore along with the previous methods for current measurements, new methods are employed to determine the stored number of ions.

An analytical model is discussed to describe the velocity dependency of the beam width during beam deceleration, where IBS influence is significant. It is very consistent with the experimental results obtained for the $^{12}C^{6+}$ coasting and bunched beams. This model is valid for ion-beam profile evolution starting from the equilibrium[2] followed by IBS, when the electron cooler is switched off. The results of IBS measurements at different energies

[1] Magnetic field range of the TSR is between 1.3 T and 0.22 T

[2] An equilibrium between electron cooling and intrabeam scattering

show that IBS has an impact on the beam quality for low-energy ions.

It has been demonstrated that unlike acceleration of the beam, beam dynamic effects under deceleration process are more adverse with respect to losses. For instance, the emittances grow larger and space-charge effects are stronger at low energy and instabilities can cause partial beam losses. For the deceleration ramp the ion beam has to be bunched and this corresponds to an increase of the line density of the charged particles resulting in higher IBS. Consequently, the transverse emittance for the same number of particles is larger if the beam is bunched.

A couple of invariants are discussed in the last chapter related to Liouville's theorem, which apply to the emittance/phase space density. The measurements approve that the expected emittance increase at lower beam energy is proportional to the inverse of the beam momentum.

The availability of low-energy ion beams now enable for precision studies on ion-atom collisions, in-ring MOT-Remi experiments.

Appendices

A Closed orbit shift by changing the magnetic field

The equation of motion in a magnetic field $\vec{B}$ is given by:

$$m \cdot \frac{d^2\vec{r}(t)}{dt^2} = Q \cdot \vec{v}(t) \times \vec{B}(\vec{r}(t)), \tag{A.0.1}$$

where m is the mass, Q is the total charge, $\vec{v}(t)$ is the instantaneous velocity of ion and $\vec{r}$ is the vector determines the particle trajectory (or closed orbit). In static magnetic fields the ion velocity $\vec{v}(t) = \dot{\vec{r}}(t)$ does not change, therefore longitudinal coordinate s can be introduced to describe the position on the orbit defined by: $s = v \cdot t$. With this parameter the eq. (A.0.1) can be written as:

$$m \cdot v^2 \frac{d^2\vec{r}(s)}{ds^2} = Q \cdot v \cdot \frac{d\vec{r}(s)}{ds} \times \vec{B}(\vec{r}(s)), \tag{A.0.2}$$

resulting in,

$$\frac{d^2\vec{r}(s)}{ds^2} = \frac{Q}{p} \cdot \frac{d\vec{r}(s)}{ds} \times \vec{B}(\vec{r}(s)), \tag{A.0.3}$$

with $\vec{B}(\vec{r}(s)) = B \cdot \vec{\eta}(\vec{r}(s))$, where $\vec{\eta}(\vec{r}(s)) = \frac{\vec{B}(\vec{r}(s))}{B}$ is the unit vector of $\vec{B}(\vec{r}(s))$, eq. (A.0.3) can be written as:

$$\frac{d^2\vec{r}(s)}{ds^2} = \frac{B}{p/Q} \cdot \frac{d\vec{r}(s)}{ds} \times \vec{\eta}(\vec{r}(s)), \tag{A.0.4}$$

where p/Q is the beam rigidity. From eq. (A.0.4) follows that if the magnetic fields of the storage ring $B \propto p/Q$, the same closed orbit $\vec{r}(s)$ is approved for an ion. In other words, changing the magnetic fields by $\frac{\Delta B}{B}$ has the same effect on $\vec{r}(s)$ as a change of the ion momentum by $\frac{\Delta p}{p}$:

$$\frac{\Delta p}{p} = -\frac{\Delta B}{B}. \tag{A.0.5}$$

B Incoherent space-charge tune shift

The space charge forces in an ion beam as well as the magnetic field of the beam interact with the individual ions. The force on an ion is given by:

$$\vec{F} = \vec{F}_{el} + \vec{F}_m, \tag{B.0.1}$$

where $\vec{F}_{el}$=$Q \cdot E$ and $\vec{F}_m$=$Q\vec{v} \times \vec{B}$. The space charge density of the beam is assumed to be constant. The space charge density of the ion beam produces an electric field:

$$E(r) = Q \cdot \rho \frac{r}{2\epsilon_0}, \tag{B.0.2}$$

where ρ is the ion density. Eq. B.0.2 leads to

$$F_{el} = Q^2 \rho \frac{r}{2\epsilon_0}. \tag{B.0.3}$$

Finally with $F_m = -\beta^2 F_{el}$:

$$F(r) = (1-\beta^2)\rho Q^2 \frac{r}{2\epsilon_0}. \tag{B.0.4}$$

Thus a force comparable to that in a defocusing quadrupole acts on each ion. This defocusing action can be described by the quadrupole strength K_r given by the following equation:

$$\frac{d^2x}{ds^2} + K_r x = 0. \tag{B.0.5}$$

The quadrupole strength K_r can be determined by solving the equation of motion:

$$\frac{d^2x}{ds^2} - (1-\beta^2)\frac{\rho Q^2}{2\epsilon_0 \gamma m v^2} x = 0, \tag{B.0.6}$$

where $p = \gamma m \frac{dx}{dt}$ and $\frac{d^2x}{dt^2} = v^2 \frac{d^2x}{ds^2}$. Comparison of eq. B.0.6 and eq. B.0.4 yields to:

$$K_R = -\frac{\rho Q^2}{2\epsilon_0 \gamma^3 m v^2}. \tag{B.0.7}$$

The focusing parameter K_R of the space charge changes the focusing of the storage ring by $\Delta K = K_R$ and leads to a tune shift:

$$\Delta Q_{shift} = \frac{1}{4\pi} \oint \beta_t \Delta K ds, \tag{B.0.8}$$

where β_t is twiss parameter of the storage ring, the closed integral over the ring circumference will be performed, therefore:

$$\Delta Q_{shift} = -\frac{q^2}{A}\frac{\langle\beta_t\rho\rangle}{2\gamma^3\beta^2}C_0 r_p, \tag{B.0.9}$$

where q is the ion charge state, A is a mass number, C_0 is the ring circumference, r_p is the classical proton radius. The particle density can be determined from the number of particles N and the beam radius R:

$$\rho = \frac{N}{\pi R^2 C_0}. \tag{B.0.10}$$

If eq. B.0.10 is inserted into eq. B.0.9 and for beam emittance $\epsilon = R^2/\beta_t$ is used:

$$\Delta Q_{shift} = -\frac{q^2}{A}\frac{r_p N}{2\pi\gamma^3\beta^2\epsilon}. \tag{B.0.11}$$

Or for the space charge limit:

$$N = \frac{A}{q^2}\frac{2\pi}{r_p}\gamma^3\beta^2\epsilon(-\Delta Q_{shift}). \tag{B.0.12}$$

For bunched ion beam the space charge limit is given by:

$$N = B\frac{A}{q^2}\frac{2\pi}{r_p}\gamma^3\beta^2\epsilon(-\Delta Q_{shift}), \tag{B.0.13}$$

where the bunching factor $B = h\frac{l_b}{C_0}$ and l_b is effective bunch length.

Density of an electron-cooled ion beam

From eq. B.0.13 is valid for ion beams with homogeneous charge distribution. The density ρ(x,y) of the stored ion beam is given by a Gaussian distribution:

$$\rho(x,y) = \frac{N}{C_0}\frac{1}{2\pi\sigma_x\sigma_y}e^{-\frac{1}{2}(\frac{x^2}{\sigma_x^2}+\frac{y^2}{\sigma_y^2})}, \tag{B.0.14}$$

where σ_x, σ_y horizontal and vertical beam width. The average ion density is:

$$\overline{\rho} = \frac{N}{C_0}\frac{1}{4\pi\sigma_x\sigma_y}. \tag{B.0.15}$$

Using $R = 2\sigma$, the gaussian beam possesses the same average density as a round, homogeneous beam with radius R. Therefore the emittance in eq. B.0.12 and in eq. B.0.13 have to be determined using the 2σ values:

$$\epsilon = \frac{(2\sigma)^2}{\beta_t}. \tag{B.0.16}$$

C Resolution of the beam profile monitor

The residual gas ionization beam profile monitor is used to determine storage ring parameters and to observe the ion beam behavior during experiments. The spatial resolution of the monitor is given by the total root-mean-square spread of[13]:

$$\Delta x_{total} = \sqrt{(\Delta x_{rec})^2 + (\Delta x_{th})^2 + (\Delta x_{el})^2}, \tag{C.0.1}$$

where Δx_{rec} is caused by the energy transfer of recoiling ions, Δx_{th} is contributed due to the thermal motion, Δx_{el} is the intrinsic resolution of the detector and the readout electronics. The spatial resolution given by the smallest detectable profile which can be obtained in beam profile measurements. Since the equilibrium size of electron-cooled ion beams increases with their intensity, only profiles measured at very low beam currents are dominated by the detector resolution. Therefore, measurements of the resolution are performed with 73.3 MeV $^{12}C^{6+}$ ions at different intensities as shown in fig. C.1. By fitting the data points in low beam currents the horizontal resolution is determined

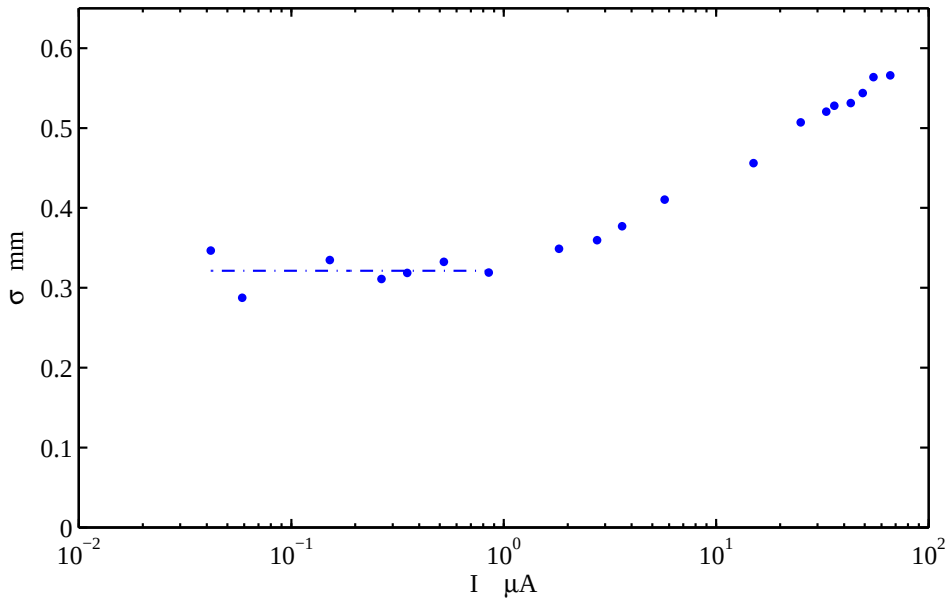

Figure C.1: Resolution of the horizontal beam profile monitor.

of about 0.32 mm. Resolution of the vertical beam profile is also determined with a analogues way, which is about 0.24 mm.

D Calibration of the resonator voltage

Synchrotron oscillation is the longitudinal oscillation of particles in storage ring around an equilibrium of the phase of the resonator voltage at the time the particles are crossing the resonator gap. The restoring force for the oscillation is provided by phase focusing so that those particles near the synchronous particle will have stable trajectories in the longitudinal phase space. For this case, the early particles experience a smaller field and the late particles a larger field than the synchronous particle. As a result of the phase stability, the energy and phase will oscillate longitudinally.

The TSR resonator voltage which is typically about $100 - 300\ V$ can be calibrated by measuring the synchrotron frequency of longitudinal oscillations of the ions. The synchrotron frequency f is given by:

$$f = \frac{1}{2\pi}\sqrt{\frac{hQU_0\eta\omega_0\cos\phi}{pC_0}} \tag{D.0.1}$$

where h is the harmonic number of revolution frequency, Q is the ion charge, U_0 is the resonator voltage, p is the momentum of the synchronous particle, C_0 is the circumference of the storage ring. The synchronous phase $\phi = 0$ for bunching the beam when the slip

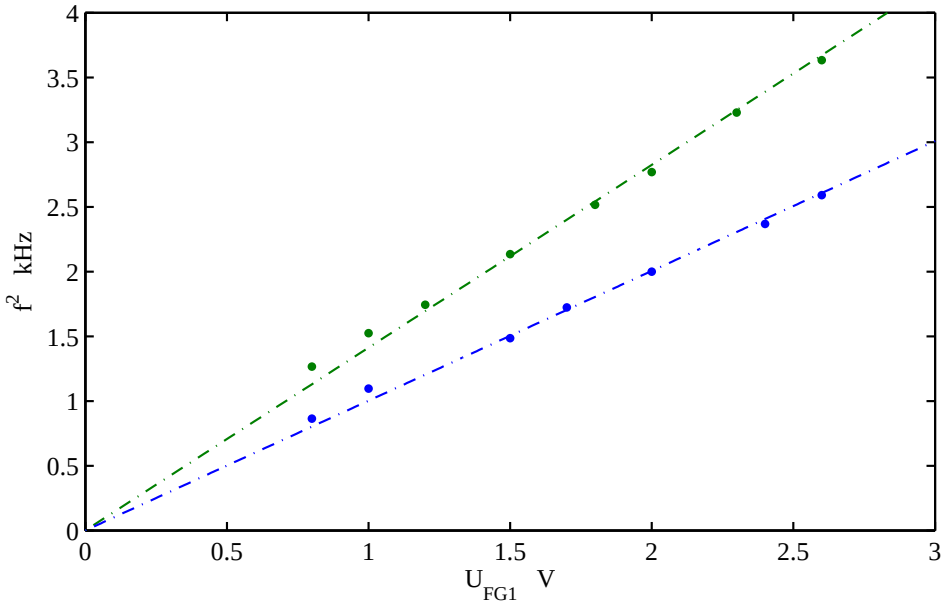

Figure D.1: Square of the measured synchrotron frequency as a function of the resonator voltage signal $U_0 \propto U_{FG1}$ at harmonic numbers of $h = 5$ (blue) and $h = 7$ (green)

factor $\eta > 0$.

$$\omega_0 = 2\pi f_0, \tag{D.0.2}$$

where f_0 is the revolution frequency given by:

$$f_0 = \frac{\beta c}{C_0} \tag{D.0.3}$$

where β is the ion velocity in units of the speed of light.

From the measured Schottky frequency $f_{Schottky} = h \cdot f_0$ the revolution frequency and momentum of the synchronous particle can be calculated. The output voltage of a function generator controlling the resonator voltage is $U_{FG1} \propto U_0$. To get the proportionality coefficient κ between the function generator voltage U_{FG1} and resonator voltage U_0 the synchrotron frequency was measured as a function of U_{FG1}. Fig. D.1 shows the calibration measurements of the resonator voltage signal, because $f^2 \propto U_{FG1}$. The corresponding value of resonator voltage at certain harmonic number for $U_{FG1} = 1\ V$ can be calculated by:

$$\frac{f^2}{f_0^2} = \frac{U_{FG1}}{U_0}, \tag{D.0.4}$$

where U_0, f_0 is a reference point, From the linear fitting through the data $\frac{f^2}{U_{FG1}}$ ratio is obtained for different harmonic numbers, relatively.

Table D.1: Measured resonator voltages for U_{FG1}=1 V.

h	$U_0[V]$
7	91.69
5	91.39

E Calibration of counting rate of BPM

As discussed in 6.2 counting rate of the beam profile monitor is given by eq. 6.34. Calibration measurements of the counting rate of horizontal beam profile monitor using $^{12}C^{6+}$ is shown in fig. E.1. Dark current during data recording is estimated as 5.49 $1/s$ and from the linear slope 1 μA corresponds to 98.01 1/s. The dark current and calibration factor

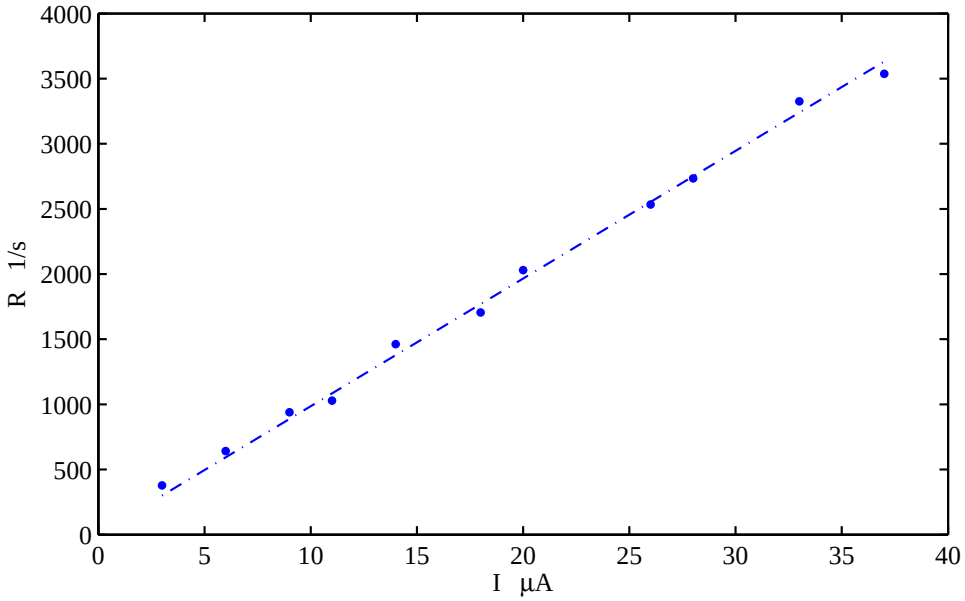

Figure E.1: Counting rate calibration of the horizontal beam profile monitor.

depends on the residual gas pressure. Calibration of the counting rate of vertical beam profile is also determined with a analogues way. The calibration value is almost the same as the horizontal calibration. Detectors and electronics of the horizontal and the vertical beam profile monitors are different.

List of Figures

List of Tables

Erklärung:

Ich versichere, dass ich diese Arbeit selbstständig verfasst habe und keine anderen als die angegebenen Quellen und Hilfsmittel benutzt habe.

Heidelberg, den (Datum) .....

Bibliography

[1] http://www.nobelprize.org

[2] F.T. Cole and F.E. Mills
Ann. Rev. Nucl. Sci. **31**, 293, 1981.

[3] H. Poth and R. W. Hasse
Cooler Rings and Their App. Symposium Proc., Tokyo, 108-123, 1990.

[4] http://www.mpi-hd.mpg.de/prioc/en/research

[5] R. Pollock
Comment. Nucl. Part. Phys. **12**, 73-84, 1983.

[6] D. Habs and et. al.
Nucl. Instr. and Meth. in Phys. Res. Section B**43**, 390-410, 1989.

[7] G. Bisoffi, M. Grieser, E. Jaeschke, D. Krämer, A. Noda
Nucl. Instr. and Meth. A**287**, 320-323, 1990.

[8] R. Webber
AIP Conf. Proc. 9^{th} Beam Instr. Workshop, 2000.

[9] M. Blum, M. Grieser, E. Jaeschke, D. Krämer, S. Papureanu
Proc. 2^{nd} Europ. Part. Acc. Conf., 955-957, 1990.

[10] M. Blum
PhD thesis, University of Heidelberg, 1989.

[11] M. Steck, G. Bisoffi, and et. al.
Nucl. Instr. and Meth. A**287**, 324-327, 1990.

[12] D. Boussard
Proc. CERN Acc. School **2**, 416, 1985.

[13] B. Hochadel, F. Albrecht, M. Grieser, D. Habs, D. Schwalm, E. Szmola, A. Wolf
Nucl. Instr. and Meth. A**343**, 401-414, 1994.

[14] M. Conte and W. MacKay
"An introduction to the physics of particle accelerators", World Scientific, 1991.

[15] L. Alvarez
Phys. Rev., **70** 799-800, 1946.

[16] J. Slater
Phys. Rev., **70** 799, 1946.

[17] K. Symon and et. al.
Proc. CERN Symposium on High Energy Acc. and Pion Phys., Geneva, **1**, 44-58, 1956.

[18] S. van der Meer
CERN/ISR-PO/72-31, 1972.

[19] http://ps.web.cern.ch/ps/training/pedestrians/

[20] S. Lee
"Accelerator physics", World Scientific, 1999.

[21] H. Grote and F.C. Iselin
The MAD Program, CERN/SL/90-13, 1990.

[22] O. Uwira, A. Müller, J. Linkemann, T. Bartsch, C. Brandau, M. Schmitt, A. Wolf, D. Schwalm, R. Schuch, W. Zong, H. Lebius, W.G. Graham, J. Doerfert, D.W. Savin
Hyperfine Interactions **108**, 149-154, 1997.

[23] W. Hardt
CERN ISR-300-gs-68-11, 1968.

[24] J.D. Jackson
"Classical Electrodynamis", Wiley, New York, 1975.

[25] A.S. Schlachter, J.W. Stears, W.G. Graham, K.H. Berkner, R.V. Pyle, J.A. Tanis
Phys. Rev. A**27**, 3372, 1983.

[26] M Bell, I.S. Bell
Part. Acc. **12**, 49, 1982.

[27] N. Bohr and K. Dan
Vidensk. Selsk. Mat. Fys. Medd. **18**, no.8, 1948.

[28] I.S. Dmitriev, V.S. Nikolaev, L.N. Fateeva, Y.A. Teplova
Sov. Phys. JETP **15**, 11, 1962.

[29] M. Beutelspacher
PhD thesis, University of Heidelberg, 2000.

[30] A. Piwinski
Pros. 9^{th} Int. Conf. on High Energy Acc., Stanford, 405, 1974.

[31] M. Martini
CERN PS/84-9(AA), 1984.

[32] M. Grieser, D. Habs, R. v. Hahn, C.M. Kleffner, R. Repnow, M. Stampfer, E. Jaeschke, M. Steck
Proc. IEEE Part. Acc. Conf., 2817-2819, 1991.

[33] B. Hochadel
PhD thesis, University of Heidelberg, 1994.

[34] M. Grieser, R. Bastert, K. Blaum, H. Buhr, R. von Hahn, M. B. Mendes, R. Repnow, A. Wolf
HIAT 09 Proceedings, Venice, 89-93, 2009.

[35] F. Laux
PhD thesis, University of Heidelberg, 2011.

[36] M. Grieser and et. al.
IPAC'11 Proceedings, Spain, 2490-2492, 2011.

[37] R. Bastert
PhD thesis, University of Heidelberg, 2009.

[38] B. Beutelspacher, M. Grieser, K. Noda, D. Schwalm, A. Wolf
Nucl. Instr. and Meth. in Phys. Res. A**512**, 459, 2003.

[39] A. Hofmann
CERN yellow report, CERN 77-13, 143, 1977.

[40] TSR Technical Design Report
European Physical Journal (EPJ), (to be published).

Acknowledgements

I would like to thank my academic advisor, Prof. Dr. Joachim Ullrich and co-advisors, Dr. M. Grieser and Prof. K. Blaum for their permanent support, guidance, advices and useful discussions. I am grateful to these persons for everything I have learned throughout my PhD years.
In addition, I would like to thank Kurt Horn, Oliver Koschorrek, Rolf Epkin, Roland Repnow for their kind help during my work on this thesis.
I present my expressions of gratitude to professors from the University of Heidelberg: A. Wolf, Prof. C. Keitel, Prof. S. Wimberger, Prof. L. Schad, and to all colleagues I have met at MPIK: Felix L., Felix B., Florian, Mike, Michael, Robert, Massimiliano, Sebastian, Janusz, Angela, Jan, Phillip, Sara, Stefan, Huayu, Ani, Siva, Ralph, Hao, Alexander and others.
My special thanks to Mary-Elizabeth and Khayrullo for their reading of the proof and comments they made on it.